Materials Horizons

ROYAL SOCIETY OF CHEMISTRY

REVIEW

View Article Online
View Journal | View Issue

Cite this: *Mater. Horiz.*, 2021, **8**, 2964

Progress on photocatalytic semiconductor hybrids for bacterial inactivation

Jiayu Zeng,†[a] Ziming Li,†[b] Hui Jiang [a] and Xuemei Wang *[a]

Due to its use of green and renewable energy and negligible bacterial resistance, photocatalytic bacterial inactivation is to be considered a promising sterilization process. Herein, we explore the relevant mechanisms of the photoinduced process on the active sites of semiconductors with an emphasis on the active sites of semiconductors, the photoexcited electron transfer, ROS-induced toxicity and interactions between semiconductors and bacteria. Pristine semiconductors such as metal oxides (TiO_2 and ZnO) have been widely reported; however, they suffer some drawbacks such as narrow optical response and high photogenerated carrier recombination. Herein, some typical modification strategies will be discussed including noble metal doping, ion doping, hybrid heterojunctions and dye sensitization. Besides, the biosafety and biocompatibility issues of semiconductor materials are also considered for the evaluation of their potential for further biomedical applications. Furthermore, 2D materials have become promising candidates in recent years due to their wide optical response to NIR light, superior antibacterial activity and favorable biocompatibility. Besides, the current research limitations and challenges are illustrated to introduce the appealing directions and design considerations for the future development of photocatalytic semiconductors for antibacterial applications.

Received 13th May 2021,
Accepted 8th September 2021

DOI: 10.1039/d1mh00773d

rsc.li/materials-horizons

1. Introduction

1.1 The crisis of bacterial infections and the development of photocatalytic antibacterial applications

Bacterial infection has become a prominent underlying cause of numerous diseases threatening human life.[1] In the past few decades, antibiotics have been widely used to combat bacteria.[2] However, the off-label abuse of antibiotics due to insufficient surveillance has resulted in an emergent crisis of antibiotic resistance and even the creation of superbugs.[3,4] Furthermore,

[a] *State Key Laboratory of Bioelectronics (Chien-Shiung Wu Lab), School of Biological Science and Medical Engineering, Southeast University, Nanjing 210096, China. E-mail: xuewang@seu.edu.cn*
[b] *MOE Key Laboratory of Macromolecular Synthesis and Functionalization, Department of Polymer Science and Engineering, Zhejiang University, Hangzhou 310027, China*
† These authors contributed equally.

Jiayu Zeng

Jiayu Zeng received her BS Degree in South China University of Technology in 2019. She is currently pursuing a Master's Degree in the State Key Laboratory of Bioelectronics of Southeast University under the supervision of Professor Xuemei Wang and Hui Jiang. Her research focuses on the design of novel bio-imaging probes for target bacteria theranostics and photodynamic therapy.

Ziming Li

Ziming Li received his BS Degree from South China University of Technology in 2019 and is now pursuing a Master's Degree in the Department of Polymer Science and Engineering, Zhejiang University under the supervision of Prof. Changyou Gao. He is currently working on the design of stimuli-responsive hydrogels for spinal cord injury (SCI) repair and regeneration. Besides, he is also interested in photocatalytic materials for antibacterial applications and tissue engineering.

the unsatisfactory input–output ratio and inadequate research activities have resulted in an equally alarming decline in the development of new antibiotics. Therefore, there is an urgent requirement for the development of novel antibacterial techniques to overcome the growing bacterial threats and address the issue of bacterial resistance.

Among the various exploited antibacterial techniques, photocatalytic disinfection as a green sustainable strategy has attracted extensive extension due to its rapid and high-efficient inactivation effect without notable drug resistance and side effects.[5] As an exogenous antibacterial technique, it relies on the strong oxidation towards bacteria induced by photogenerated ROS, which contains no chemical additives or harmful inactivation by-products.[6] Driven by solar energy, the antibacterial process is controllable, recyclable and low cost. Studies have shown that photocatalysis has broad-spectrum inactivation properties for many G-(+) and G-(−) bacteria including *E. coli*, *S. aureus*, *P. aeruginosa* and *S. choleraesuis*.[7] The photocatalytic antibacterial technique can be applied for various occasions ranging from environmental purification to biomedical treatment of bacterial infections, including environmental water disinfection, medical equipment disinfection, food sterilization, human implant sterilization, bacteria-infected wound cure and even bacterial inflammation therapy.[8,9] With the development of the photocatalytic technique, some commercial industrial applications have emerged such as self-cleaning antibacterial films, ceramic tiles, fabrics and glasses.[10]

1.2 The development of semiconductors for photocatalytic inactivation

In photocatalysis, the choice of suitable catalysts is crucial for antibacterial effects, and the photocatalysts are mainly semiconductor materials. Since Fujishima and co-workers[11] discovered the catalytic decomposition of water on the surface of the TiO_2 semiconductor with UV irradiation, photocatalysis has become a research hotspot for developing a novel field of semiconductor applications. Also, the use of photocatalytic bacterial inactivation was discovered by T Matsunaga's team,[12] who reported the photoelectrochemical sterilization of *S. cerevisiae* with semiconductor TiO_2/Pt powder as the catalyst. Inspired by this work, there have been numerous reports on photocatalytic semiconductor sterilization. N-type semiconductors such as n-TiO_2 and n-ZnO were extensively reported initially; however, pristine semiconductors suffer from inherent drawbacks such as wide energy gap, which can only be excited under UV (less than 4% of the solar spectrum[13,14]), and high rate of photogenerated change carrier recombination,[15] leading to unsatisfactory photocatalytic activity.

To overcome these drawbacks, researchers have explored the modification and reconstruction of pristine semiconductors.[16] For example, it has been proven that noble metals (for example, Ag and Au NPs) loaded on the surface of TiO_2 can effectively separate photo-generated electron–hole pairs.[15,17] Also, anion and cation doping have been investigated[18,19] to successfully restructure the bandgap of pristine semiconductors. Especially, 2D semiconductors such as g-C_3N_4, MoS_2, and BPs have attracted extensive attention in the field of photocatalytic applications in recent years,[20,21] owing to their appealing properties such as wide light response to NIR and layers-dependent band energy. However, there are few comprehensive reviews on pristine semiconductors and their modified hybrids for photocatalytic sterilization.

Herein, we comprehensively review the research progress on photocatalytic antibacterial semiconductors in recent years, including their energy band structures, synthetic techniques, photocatalytic mechanisms, ROS-induced antibacterial effects, and the influence of different modification strategies. Besides, the biosafety of the material such as cell compatibility and the evolution/degradation behaviors of semiconductors for further use in the biomedical field will be presented. Finally, some challenges and perspectives on semiconductor photocatalysts will be also discussed to spark appealing directions and design considerations for future semiconductors (Fig. 1).

Hui Jiang

Hui Jiang received his PhD (2005) from the University of Science and Technology of China. After completing postdoctoral research at Nanjing University, he joined the faculty of Biomedical Engineering at Southeast University in 2007, and now he is an Associate Professor. His research interests include nanocluster assembly and biological imaging, micro–nano biosensors and the research on POCT.

Xuemei Wang

Xuemei Wang received her PhD in Chemistry from Nanjing University in 1994 and then worked as a Lecturer in the Department of Chemistry in Nanjing University from 1995 to 1996. From 1996 to 1998 she studied in Germany with Alexander von Humboldt Fellowship. Then she came back to Nanjing and worked in the School of Biological Science and Medical Engineering as an Associate Professor in Southeast University. Since 2001 she has worked in Southeast University as a Full Professor. Her main research interests cover the design of novel bio-imaging probes including self-assembled biosynthesized functionalized nanoclusters/or smart nano-robots for target cancer theranostics, biosensors and nanomedicine.

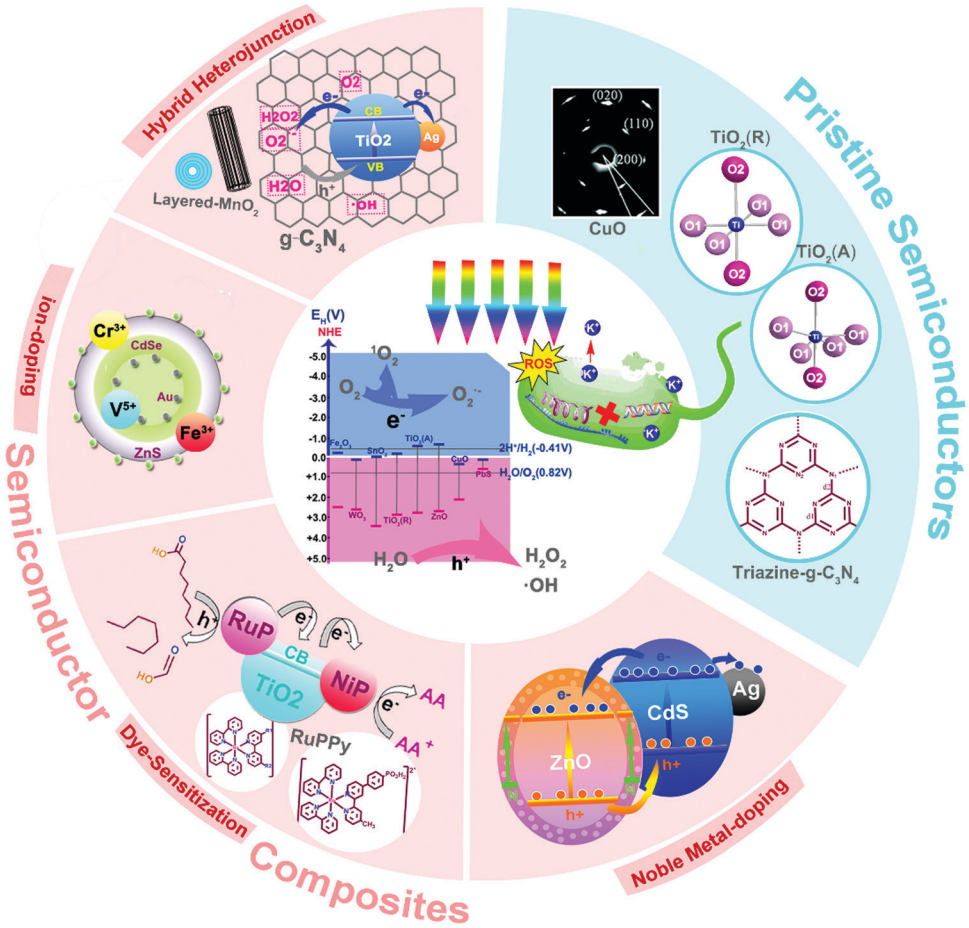

Fig. 1 Various photocatalytic semiconductor systems for photocatalytic bacterial inactivation.

2. Fundamentals of photocatalytic semiconductor hybrids for bacterial inactivation

2.1 Fundamentals of heterogeneous photocatalysis for bacterial inactivation

Knowledge on bacterial inactivation is crucial for the effective development of novel composite materials. Microbial disinfection driven by solar energy has attracted widespread attention as a sustainable green strategy, which achieves rapid disinfection through a powerful oxidation process without the requirement of additional chemical substances.[6] The key to achieve rapid photocatalytic disinfection is ROS-induced toxicity.

ROS is mainly involved in cellular oxidative stress, and although its inactivation mechanisms are not very clear to date, its potential mechanisms are as follows: (1) cell wall or cell membrane damage may be induced by intracellular K^+ leakage. For example, Lu and Thabet *et al.*[22,23] found that in the process of cells killing, photocatalysis alters the cell membrane permeability and leads to intracellular K^+ leakage. (2) Small enough engineered nanoparticles penetrate the cell membrane and photocatalysis occurs inside. NPs may indirectly attack intracellular substances by ROS or directly attack them to cause cell death. For example, it has been found that ultrafine TiO_2 particles can break bacterial plasmid DNA molecules.[24] (3) ROS causes intracellular acetyl-CoA oxidative/reductive injury, leading to cell respiratory system damage.[25] (4) Photo-generated ROS may cause intracellular overproduction of ROS, which induces oxidative stress. For instance, Wu *et al.*[26] reported that a red phosphorus/g-C_3N_4 composite system caused the sunlight-driven photogeneration of ROS, which could enter bacteria and then induce enhanced endogenous O^{2-} and H_2O_2 production. Also, Wang *et al.* invented various methods for the detection and tracing of intracellular ROS or other related substances.[27–33]

2.2 The photocatalytic mechanisms of semiconductor hybrids in photocatalytic bacterial inactivation

2.2.1 The band structure of semiconductors based on density functional theory (DFT) calculation. Generally, the energy band structure refers to the fact that the electronic states exhibited by electrons in a solid enable them to exist continuously in some energy ranges under the action of the potential field formed by the periodically distributed atomic nuclei, while the others are completely forbidden in other energy ranges. In a narrow sense, the electronic energy band structure refers to the dependence of the energy of a single electron state near the Fermi energy on the lattice wave vector k, which is also called the band diagram (band diagram).

The electronic energy band structure discussed here covers the meaning of the above-mentioned two aspects.

Specifically, first-principles electrons based on Kohn–Sham (KS) density functional theory based on the local density approximation (LDA) or generalized gradient approximation (GGA) structural theory play an increasingly important role in semiconductor physics, especially in the study of band gaps. The latter reformulates the complex quantum multisystem problem as a formal single-system problem by establishing the mapping relationship between a real multi-electron interaction system and a virtual non-interaction system with the same ground state electron density. Due to its conceptual intuition, the energy difference between the highest occupied molecular orbital (HOMO) and the lowest unoccupied molecular orbital (LUMO) is used to describe the band gap and is known as the Kohn–Sham band gap, which has been widely used to describe the electronic band structure properties of materials, *i.e.*,

$$\Delta\varepsilon = \varepsilon^{\mathrm{LUMO}} - \varepsilon^{\mathrm{HOMO}} \quad (1)$$

Moreover, for the dependence of the single-electron state energy near the Fermi energy on the lattice wave vector k, the band gaps with orbital energies corresponding to the same wave vector are called direct band gaps, whereas those with different wave vectors are called indirect band gaps. For many systems, LDA/GGA can give a qualitatively correct image of the electronic energy band structure, but because the pure ground state theory DFT ignores the consequences of excitation, the basic energy gap and optical transition can be clearly underestimated and revealed, and thus there is a systematic error in quantitative analysis. Compared to the LDA/GGA, the Heyd–Scuseria–Ernzerhof (HSE06) hybrid functional with range separation can usually reproduce the hybrid orbital of many semi-conductor band gaps more accurately. For more details, please refer to the literature.[34–38] Herein, we pay focus on whether the lowest excitation energy (whether direct or indirect) calculated by eqn (1) can be excited by ordinary visible light or ultraviolet light, given that the size and properties of the band gap contribute greatly to photocatalysis.

2.2.2 The photogenerated charge carriers and ROS. During photocatalysis, the photocatalytic material assimilates photon energy exactly equivalent to or larger than its own band gap. An electron with a negative charge (e^-) in the valence band (VB) of the semiconductor jumps towards the conduction band (CB), leaving a void with a positive charge (h^+) in the VB. The photogenerated h^+ and e^- diffusing on the surface of semiconductors act as strong oxidizing and reducing agents, respectively. They perform electrochemical redox reactions, which macroscopically presents the photoinduced chemical synthesis process. These photo-responsive and catalytic semiconductors are defined as photocatalysts. However, unsatisfactory recombination of charge carriers tends to occur, reducing their photocatalytic efficiency. The relaxed electrons will return to the conduction band directly or recombine with holes in traps.[39,40] These mechanisms are illustrated in Fig. 2.

ROS, mainly consisting of superoxide radical ($O_2^{\bullet -}$), hydrogen peroxide (H_2O_2), hydroxyl radical ($^\bullet OH$) and singlet oxygen ($^1O_2$),

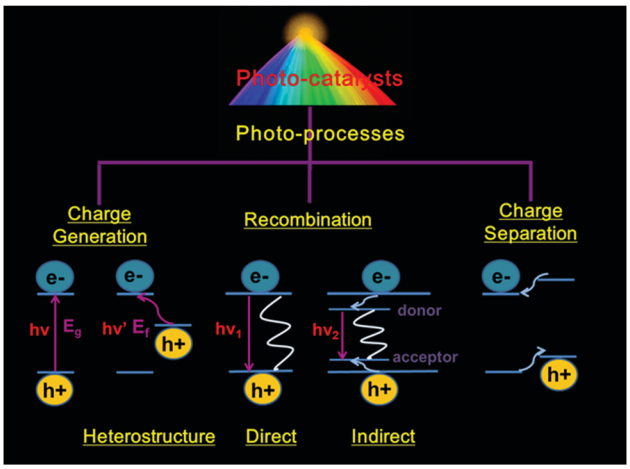

Fig. 2 Basic photo-process of photocatalysts. E_g: band gap of a semiconductor and E_f: Fermi energy of the immobilized noble metal particles. After photo-excitation, radiative and non-radiative recombination can occur, as depicted by the straight and wavy lines, respectively.

are also generated in the process of photocatalysis. When irradiated charge carriers are formed, $O_2^{\bullet -}$ appears *via* the interaction between oxygen and electrons. Also, $^\bullet OH$ will be formed through the oxidation of H_2O or OH^-. $^1O_2$ can be generated from the subsequent reduction of the superoxide anion or directly generated from oxygen (O_2) by utilizing the energy from recombination.[41,42] These processes can be depicted by eqn (2)–(5) as follows:

$$O_2 + e^- \rightarrow O_2^{\bullet -} \quad (2)$$

$$H_2O + h^+ \rightarrow {}^\bullet OH + H^+ \quad (3)$$

$$OH^- + h^+ \rightarrow {}^\bullet OH \quad (4)$$

$$O_2 \rightarrow {}^1O_2 \quad (5)$$

It should be noted that the bottom of the CB of the photocatalytic material should be more negative than the potential of $O_2/O_2^{\bullet -}$ or the top of VB should be more positive than the potential of $H_2O/^\bullet OH$ to produce redox reactions. The occurrence of redox reactions also requires certain thermodynamic conditions.[5]

2.3 The current research on photocatalytic semiconductor hybrids for bacterial inactivation

Photocatalytic bacterial inactivation has become an appealing direction for the application of semiconductors. However, the photocatalytic antibacterial mechanisms remain unclear such as the surface interactions between bacteria and semiconductors and ROS-induced antibacterial actions, which will attempt to be solved in the following sections with emphasis on the reactive sites and specific antibacterial mechanisms of each semiconductor. Also, a unified measurement of antibacterial ability of semiconductors is lacking, given that the photocatalytic antibacterial effect is affected by various internal/external conditions, such as preparation method, material morphology, catalyst concentration, reaction environment (such as pH,

temperature, solution, and light intensity),[10] which will be summarized and discussed in the tables below. For many semiconductors, they mainly depend on visible-light-driven energy, which is restricted to disinfection in the external environment, but does not meet the medical requirements of antibacterial or anti-inflammatory *in vivo*, demanding deeper photon penetration.[43] Also, cell compatibility and the evolution or degradation of materials in the physiological environment should be considered for further medical applications. 2D semiconductors seem to be more suitable in this regard, which will be discussed in detail.

3. Pristine semiconductors for bacterial inactivation

3.1 The classification of semiconductors

3.1.1 n-type semiconductor. Semiconductors are currently classified into p-type and n-type semiconductors according to their different charge carriers.[44] In n-type semiconductors, electrons serve as the main photo-generated carriers,[45,46] whereas positive charge carriers (holes) are the majority in p-type semiconductors.[47,48] Also, there is a significant difference in the mobility between them. It is widely recognized that n-type semiconductors possess a higher mobility due to the adequate electrons produced by oxygen vacancies,[49,50] together with the unimpeded electron-transport paths mainly composed of spatially spread metal s orbitals in the conduction-band minimum (CBM).[51] It should be noted that these spatially spread and isotropic orbitals result in a highly dispersed and delocalized CBM, facilitating a low electron effective mass, and therefore the photo-excited electron can move without limitation, making reduction reactions easy (Fig. 3).[52]

The typical n-type TiO_2 and ZnO as photocatalysts have been widely investigated; however, they still suffer from a wide bandgap from their O 2p orbitals to M 3d (M = Ti and Zn) orbitals,[55,56] which can only be excited by light in the UV region with a wavelength below 390 nm[57] and 370 nm,[58] respectively. When irradiated by enough photon energy, photocatalysis will occur on their surface as follows (using TiO_2 as an example):[59–61]

$$TiO_2 + h\nu\ (\lambda < 390\ \text{nm}) \rightarrow h_{vb}^{+} + e_{cb}^{-} \quad (6)$$

The photogenerated electron and/or hole react with the hydrated ($>Ti^{IV}OH$) surface functionality of TiO_2 to form $[Ti^{III}OH]$ and $[Ti^{IV}OH]^+$, as depicted in eqn (7) and (8), where $>Ti^{IV}OH$ represents the primary hydrated surface functionality of TiO_2.

$$e_{cb}^{-} + >Ti^{IV}OH \rightarrow [Ti^{III}OH] \quad (7)$$

$$h_{vb}^{+} + >Ti^{IV}OH \rightarrow [Ti^{IV}OH]^{+} \quad (8)$$

$[Ti^{III}OH]$ acts as a reducing agent to reduce oxygen into superoxide radicals, which can be subsequently reduced to $^1O_2$ by $[Ti^{III}OH]$, as shown in eqn (9) and (10). For eqn (11), water is oxidized to hydroxyl radicals by $[Ti^{IV}OH]^+$, which functions as an oxidant agent.

$$[Ti^{III}OH] + O_2 \rightarrow O_2^{\bullet -} + >Ti^{IV}OH \quad (9)$$

$$O_2^{\bullet -} + [Ti^{III}OH] \rightarrow {}^1O_2 \quad (10)$$

$$[Ti^{IV}OH^{\bullet}]^{+} + H_2O \rightarrow {}^{\bullet}OH + >Ti^{IV}OH \quad (11)$$

Serving as an h^+-trapper and e^--trapper, $[Ti^{IV}OH^{\bullet}]^+$ and $[Ti^{III}OH]$ contribute to the indirect recombination of charge carriers, respectively.

$$e_{cb}^{-} + [Ti^{IV}OH^{\bullet}]^{+} \rightarrow >Ti^{IV}OH \quad (12)$$

$$h_{vb}^{+} + [Ti^{III}OH] \rightarrow >Ti^{IV}OH \quad (13)$$

However, due to the low photoelectric conversion efficiency and high photogenerated charge carrier rate,[62] the effect of photogenic ROS is far from satisfactory. For example, Macyk *et al.*[63] reported the low efficiency of $^1O_2$ formation and sometimes even no generation of $^1O_2$ on pure TiO_2, whereas when the abundant OH^- groups on the surface of TiO_2 were substituted by other atoms such as $[PtCl_6]^{2-}$, the efficiency of the energy transfer pathway would be enhanced, and therefore generating $^1O_2$.

3.1.2 p-type semiconductors. For p-type semiconductors, CuO is a representative one,[64] which is attributed to the presence of negatively charged copper vacancies and interstitial oxygen.[65] However, its conductivity mechanism is still under

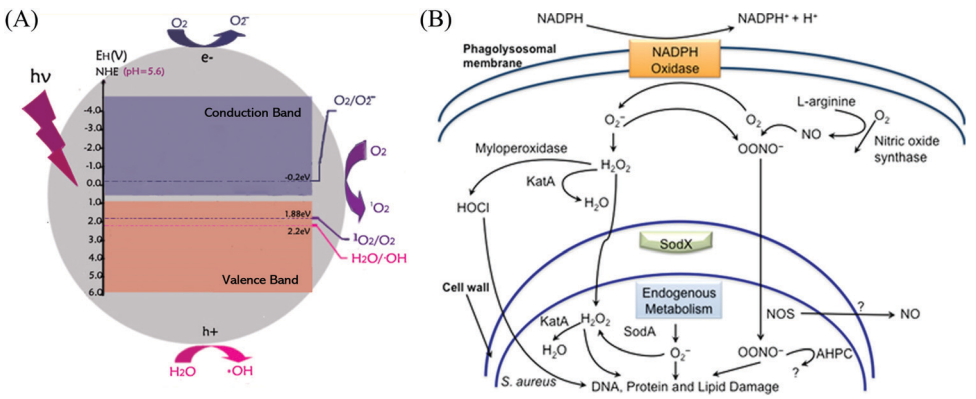

Fig. 3 (A) Edge locations of H_2O and O_2 in water at pH 5.6. The normal hydrogen electrode (NHE) is used as a reference. Reprinted from ref. 53. (B) Intracellular mechanism of ROS-induced bacterial inactivation. Reprinted from ref. 54.

debate. It is widely acknowledged that CuO has an open 3d shell level ($3d^9 4s^0$), instead of a closed one ($3d^{10}4s^0$), which can avoid absorption in the visible range from the d–d transition like Cu_2O,[66] endowing CuO with a direct and narrow band gap (about 1.2 eV in the bulk),[67] enabling it to absorb near infrared light.[67,68] According to Zhang,[69] the optical absorption spectrum for nanostructured CuO can cover nearly the whole visible range depending on various process parameters and measurement techniques.

Actually, the antibacterial activity of copper and copper oxide have not been well investigated, partially due to the rapid oxidation of metallic copper nanostructures exposed to air[70] and physical and chemical instability of copper oxides at room temperature, particularly in the presence of Cu^{2+}.[71] Akhavan[72] reported the superiority of bacterial disinfection using Cu compared with CuO nanoparticles, attributing to the better electron accepting ability of Cu, as a good electron acceptor, which led to an enhancement in antibacterial activity *via* disruption of the wall membrane of the bacteria.

Also, the photocatalytic reaction and photogenerated ROS present on the surface of CuO are as follows:[73,74]

$$CuO + h\nu\ (<660\ nm) \rightarrow CuO\ (e_{cb}^-, h_{vb}^+) \quad (14)$$

The excited electron can either react (a) directly with O_2, forming $O_2^{\bullet -}$ or (b) reduce the Cu^{2+} lattice to Cu^+, leading to the following reactions (15)–(17) with the formation of $O_2^{\bullet -}$ radicals:

$$CuO\ (e_{cb}^-) + O_2 \rightarrow CuO + O_2^{\bullet -} \quad (15)$$

$$CuO\ (e_{cb}^-) \rightarrow CuO\ (Cu^+) \quad (16)$$

$$CuO\ (Cu^+) + O_2 \rightarrow CuO\ (Cu^{2+}) + O_2^{\bullet -} \quad (17)$$

Reaction (18) shows that the equilibrium between H^+ and $O_2^{\bullet -}$ leads to the formation of the $HO_2^{\bullet}$ radical. Also, H_2O_2 can be produced either by $HO_2^{\bullet}$ (reaction (19)) or by (reaction (20)) as follows:

$$H^+ + O_2^{\bullet -} \rightarrow HO_2^{\bullet} \quad pK_a = 4.8 \quad (18)$$

$$CuO\ (Cu^+) + HO_2^{\bullet}\ (\text{partial } O_2^{\bullet -}) + H^+ \rightarrow CuO\ (Cu^{2+}) + H_2O \quad (19)$$

$$2Cu(I) + O_2 + 2H^+ \rightarrow 2Cu(II) + H_2O_2 \quad (20)$$

Notably, p-type semiconductors possess a low mobility, considering that the higher formation energy of the intrinsic acceptor and lower formation energy of the natural donor will harden the generation of holes.[75,76] Furthermore, owing to the anisotropy and O2p orbital with less overlap, the transfer of holes in the valence-band-maximum (VBM) is difficult, which reduces its mobility.[68] This low mobility of charge carriers hampers the development and further use of p-type semiconductors, remaining a challenge to researchers.[77]

The bandgap of some typical pristine semiconductors including nano TiO_2, ZnO, and CuO are illustrated in Fig. 4.

3.2 The active sites and catalytic activity

Photocatalytic reactions tend to occur at the active sites on the surface of the material, where clarification of the active site is beneficial to further understand the photocatalysis mechanism and improve the photoelectric conversion efficiency.[79] The active sites are normally located at the edge, unsaturated steps, and/or corner atoms of semiconductors.[80] The coordination of unsaturated transition metal (Ti, Cr, Fe, Mn, *etc.*) compounds are important in photocatalytic applications.[81] Generally, the lower the coordination number, the higher the chemical activity.[82] Fujitsuka *et al.*[83] identified the photocatalytic active sites of 6-coordinated configurational-TiO_2 at the single-molecule level, where they proposed that the surface hetero-junction (edges and corners) formed by the (001) planes and (101) planes can act as active sites to accumulate photogenerated electrons and holes. Zewail *et al.*[81] proposed the 5-coordinated $Ba_2Ti_2Si_2O_8$ photocatalyst, where photoexcited electrons are rapidly transferred from the apex oxygen to the central Ti atom, resulting in the separation of the two atoms and the transformation of the original $Ti^{4+}{=}O^{2-}$ double bond state into a Ti^{3+}–O^{1-} single bond, which acts as the active site of the catalytic reaction (Fig. 5).

It has been reported that the crystal structure also affects the photocatalytic activity of materials. Pang *et al.*[84] discovered the

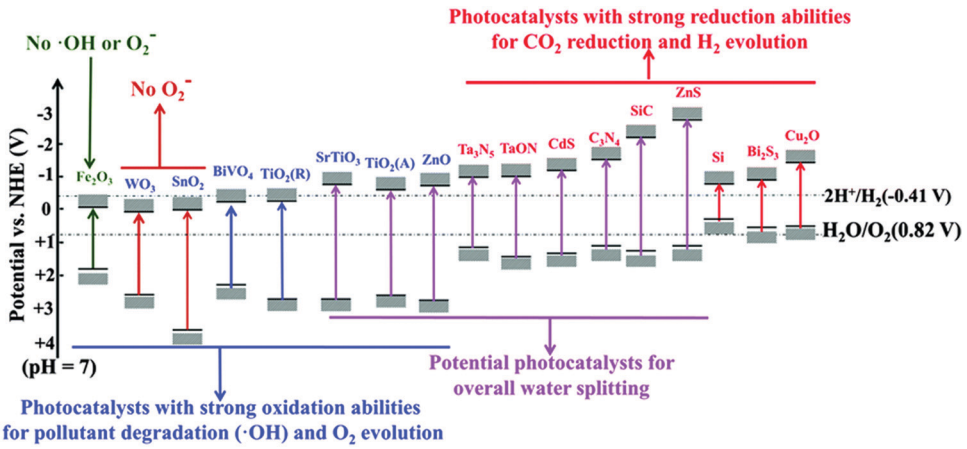

Fig. 4 Band gap of some typical pristine semiconductors (at pH = 7) and their potential applications. Reprinted from ref. 78.

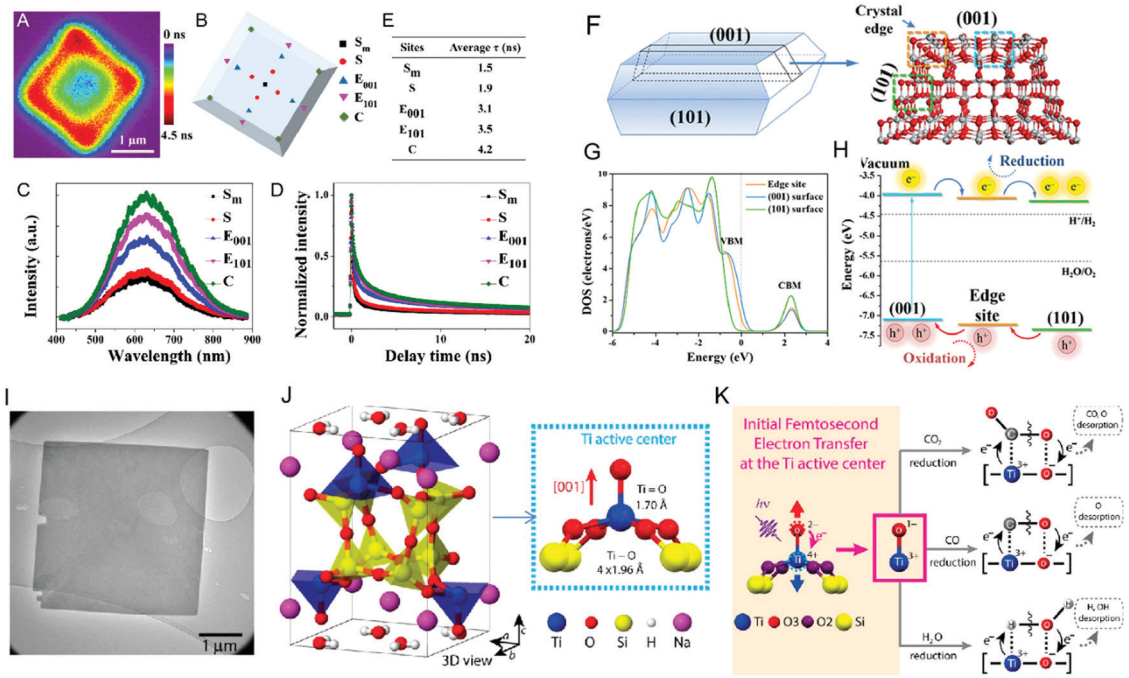

Fig. 5 Crystal structures and active sites of different coordination Ti (TiO_2 and $Ba_2Ti_2Si_2O_8$). (A) PL lifetime mapping of a single anatase TiO_2 particle shown with color bar. (B) Site distribution of a single anatase TiO_2 particle and its PL spectra (C) and lifetime (D). (E) Delay time of each site. (F) Crystal and electronic model of anatase TiO_2. (G) Different band structure characteristics between edge site and (001) and (101) surfaces. (H) Energy level structure of different photocatalytic sites and photogenerated carrier transfer process. (I) and (J) Bright-field image and schematic crystal structure of $Ba_2Ti_2Si_2O_8$. (K) Rapid electron transfer from O to central Ti when excited. (A)–(H) Reprinted from ref. 83. (I)–(K) Reprinted from ref. 81.

shape-dependent antibacterial behavior of Cu_2O, whose inactivation effect changed from broad-spectrum bacteriostasis to high selectivity with a morphology ranging from cubic to octahedral for different surface facets of its various crystal structures (such as (100) surfaces for cubes and (111) surfaces for octahedrons), exhibiting the respective adsorption and desorption behaviors towards bacteria.[84] According to Prasanna[85] and Gunder,[86] intrinsic defects such as the shallow defect state formed by Zn interstitials (Zni) and deep defect state formed by oxygen vacancies (VO) can reduce the charge carrier recombination efficiency. The introduction of structural defects or disorder enables a reduction in the coordination number of adjacent sites and affects the electronic structure of the catalyst to adjust the activity of its active sites.[87]

Besides, the interactions between the reactive states of a photocatalyst and the solvents around affect its photocatalytic activity. For example, Niu *et al.*[88] reported the differences in the antibacterial effects of ZnO NPs in different media. It was

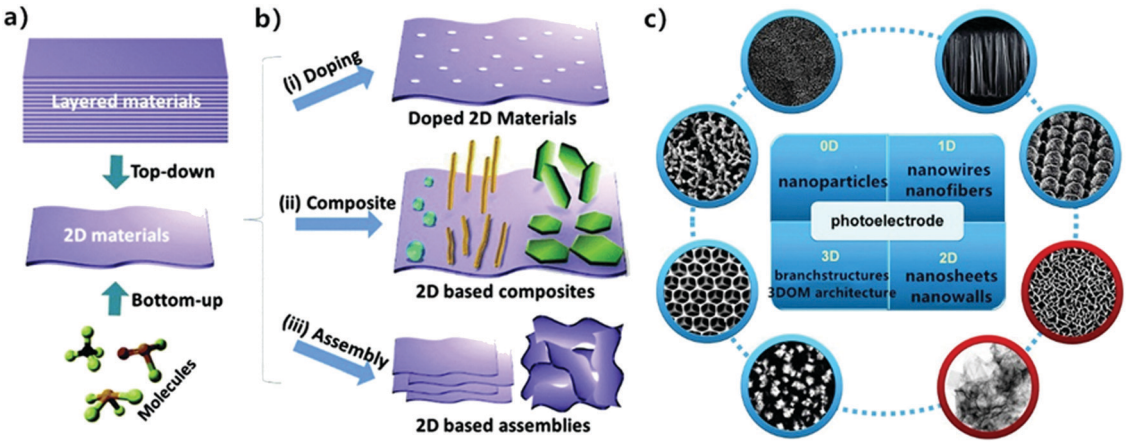

Fig. 6 Scheme of (a) "top-down" and "bottom-up" methods to synthesize 2D materials. (b) Modification of 2D materials as photocatalysts, consisting of (i) doping construction, (ii) compositing with other 0D/1D nanomaterials, and (iii) 3D structure assembled with 2D layers. Reprinted from ref. 100. (c) Basic geometrical motifs of different dimension materials. Reprinted from ref. 95.

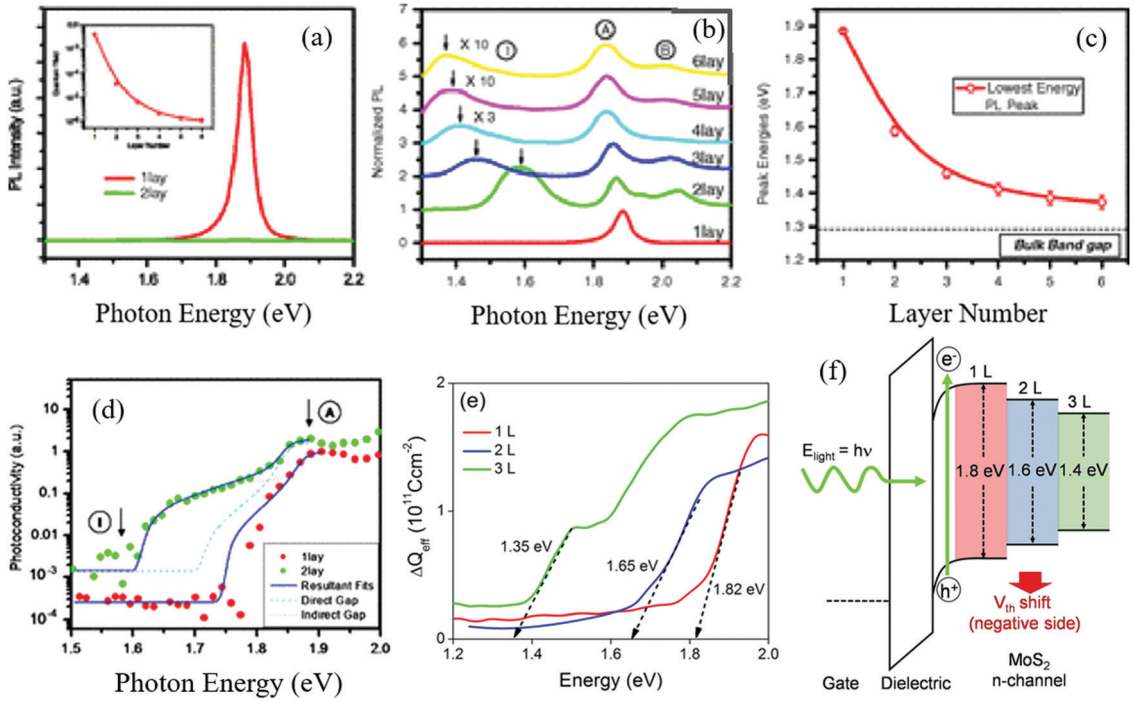

Fig. 7 (a) Photon energy of MoS_2 with single and two layers. (b) Relative photon energy of different numbers of MoS_2 layers. (c) Energy gap of different numbers of MoS_2 layers. (d) Photoconductivity spectra for 1-layer and 2-layer samples, (e) measurements of their band gap energy, and (f) photoelectric effects of MoS_2 with different layers, respectively. (a)–(d) Reprinted from ref. 116. (e) and (f) are Reprinted from ref. 117.

shown that ZnO NPs in DI water exhibited a better effect on *E. coli* of than in other electrolyte solutions because less aggregation of the particles occurred, with the greater generation of ROS. Also, the nano ZnO was positively charged in DI water, which facilitated the attachment of the ZnO NPs to the negatively charged *E. coli*. Gaffney's team described the solvation kinetics around the catalytic active site, showing that the structure of the photocatalyst changes with the structure of its solvated shell.[89] Muckerman[90] demonstrated that the catalytic activity exhibited at the interface between the semiconductor and solvent is caused by a complicated series of physical and chemical steps.

3.3 An overview of 2D nanomaterials

The scale of materials has a critical effect on their photocatalytic performance. For example, Lakshmi[91] found that ZnO nanoparticles (NPs) exhibited stronger inactivation than ZnO microparticles (MPs) because of their high surface area and

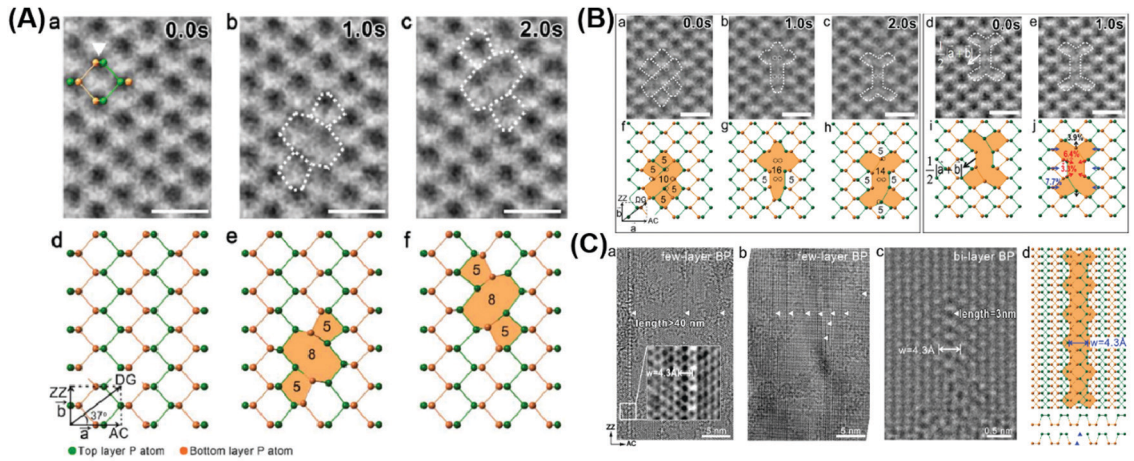

Fig. 8 Various vacancy defects of atomically thin BPs. (A) HRTEM images and the corresponding schematical atomic structures of the time-dependent formation and migration of binary vacancies (a–f). (B) HRTEM images and the corresponding schematic atomic structures of the time-dependent formation and migration of a tetra-vacancy (a–j). (C) TEM images of long vacancy line arrays existing in few-layer BP (a and b) and bi-layer BP (c), and (d) schematic crystal structure of the line vacancy corresponding to (c). Reprinted from ref. 120.

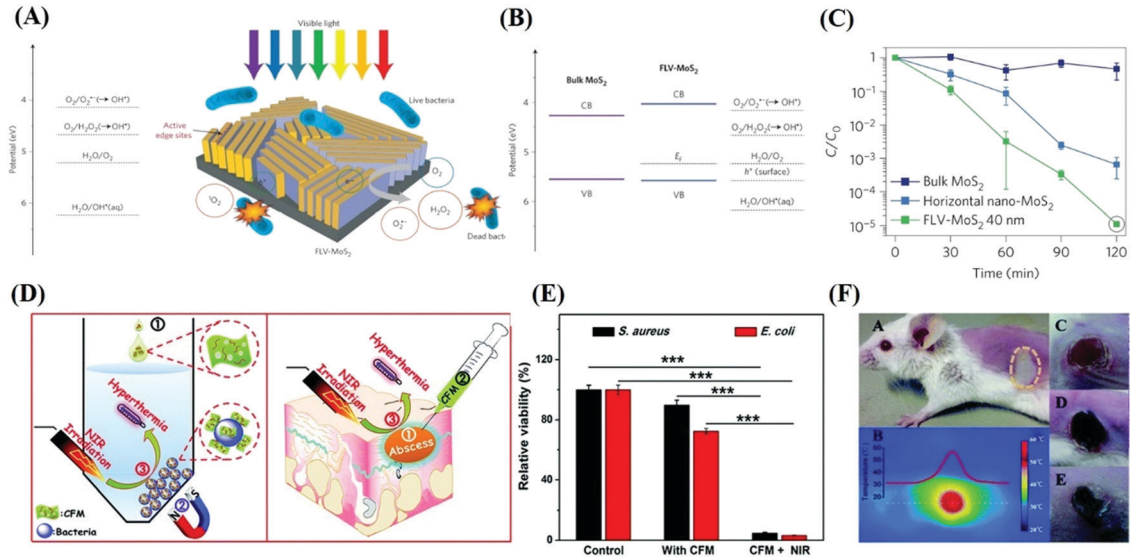

Fig. 9 Photocatalytic antibacterial effects of MoS_2 in response to various wavelengths. (A) Potential of ROS referring to the vacuum level and schematic illustration of photogenerated ROS-induced bacteria death in the present of optical light. (B) Band edge of two different MoS_2 with respect to the ROS formation potential. (C) Corresponding inactivation effects of three MoS_2-based materials. (A)–(C) Reprinted from ref. 122. (D) Photothermal disinfection effects *in vitro* and local infection treatment *in vivo* by MoS_2-based materials with NIR exposure. (E) Inactivation capability of CFM with or without NIR irradiation. (F) Serial characterization of photothermal therapy effects of CFM treatment in infected mouse *in vivo*. (D)–(F) Reprinted from ref. 124.

quantum size effect. Also, the 2D morphology of MoS_2 exhibits better antibacterial activity compared with raw MoS_2 powder (0D) due to its planar structure with more exposed active sites.[92] Two-dimensional (2D) nanomaterials first appeared when Ferrari *et al.*[93] successfully exfoliated mono-layered graphene from bulk graphite in 2014. Monolayer or thin-layer graphene is formed by a network of hexagonal enclosed carbons, which are stacked by van der Waals forces, with each layer spaced at 3.3 Å.[94] Owing to their intriguing physicochemical properties such as limited quantum effect, atomic thickness, high specific surface area, adjustable electronic structure, low recombination of electrons and holes, and abundant surface active sites,[95,96] 2D nanomaterials have become promising candidates in photocatalytic applications, and thus various methods for the preparation of 2D materials have been developed.[97,98] They mainly include two categories, one is the "top-down" exfoliation of layered materials and the other is the "bottom-up" synthesis of molecular precursors.[99] It has also been reported that a controllable layer number (thickness), dye doping construction and heterostructure composition during the preparation of 2D

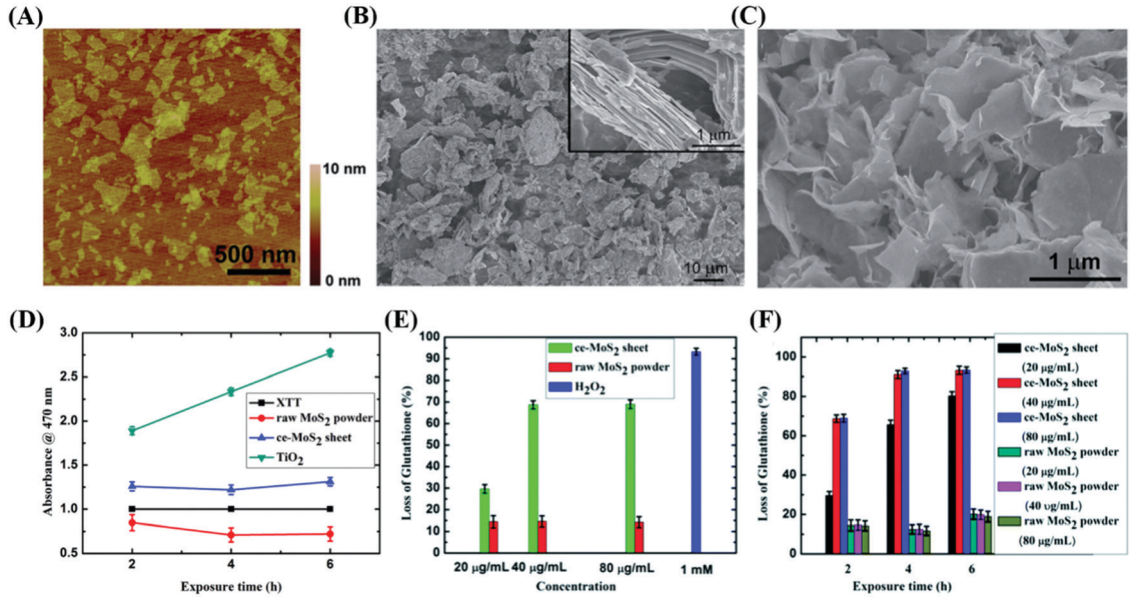

Fig. 10 Significant distinction in morphology and antibacterial properties between MoS_2 particles and sheets. Reprinted from ref. 129.

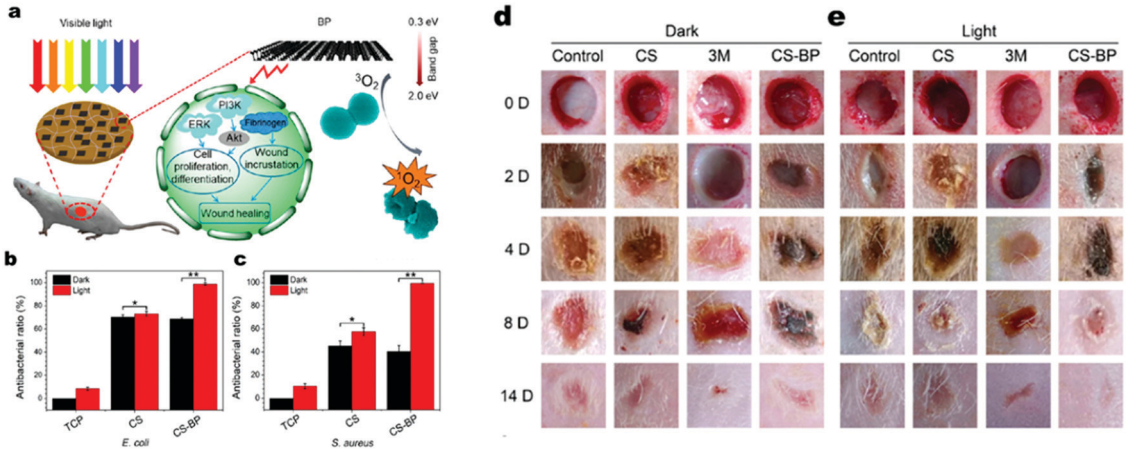

Fig. 11 Photocatalytic bacterial inactivation and would healing promotion by BP. (a) Schematic illustration of photocatalytic bacterial inactivation and wound healing by BP. (b) and (c) *In vitro* photocatalytic bacterial inactivation against two different bacteria. (d) and (e) *In vivo* wound healing process. Reprinted from ref. 137.

materials are critical to their photocatalytic properties and applications (Fig. 6).

3.3.1 The thickness-modulated energy gap and light absorption of 2D semiconductors. 2D nanostructures materials are mainly monolayer or thin-layer exfoliated from bulk their counterpart,[101] such as nanosheets[33,102] and nanowalls.[103,104] Also, the indirect energy gap of bulk materials differs from that of monolayer materials, which importantly exhibits a well-defined dependence on thickness.[105] For example, monolayer MoS_2 possesses a direct energy gap of about 1.8 eV, consisting of weak S–Mo–S coupling layers.[106] As the number of layers increases, the indirect band gap of the bulk material shifts downwards monotonically until its threshold due to the perpendicular quantum confinement.[105,107] Moreover, multiple-layer MoS_2 conventionally stacks in a staggered arrangement of Mo atom layers and S atom layers,[108] and the actual determining factor of band gap energy becomes the layer separation due to this arrangement[109,110] (Fig. 7). Similar to MoS_2, BP possesses a direct energy gap ranging from 2.0 to 0.3 eV (from bulk to monolayer), depending on the number of layers (or thickness[111,112]), endowing BP a tunable band gap width and light absorption and photo-excitation capacity by UV, visible or NIR light.[113] It should also be noted that the charge transport anisotropy in BP dominantly relies on the number of layers,[114,115] which provides a balance between the suppression of charge carrier recombination and wide light absorption range.

3.3.2 The photocatalytic active sites and disinfection performance. Increasing the specific surface area of materials

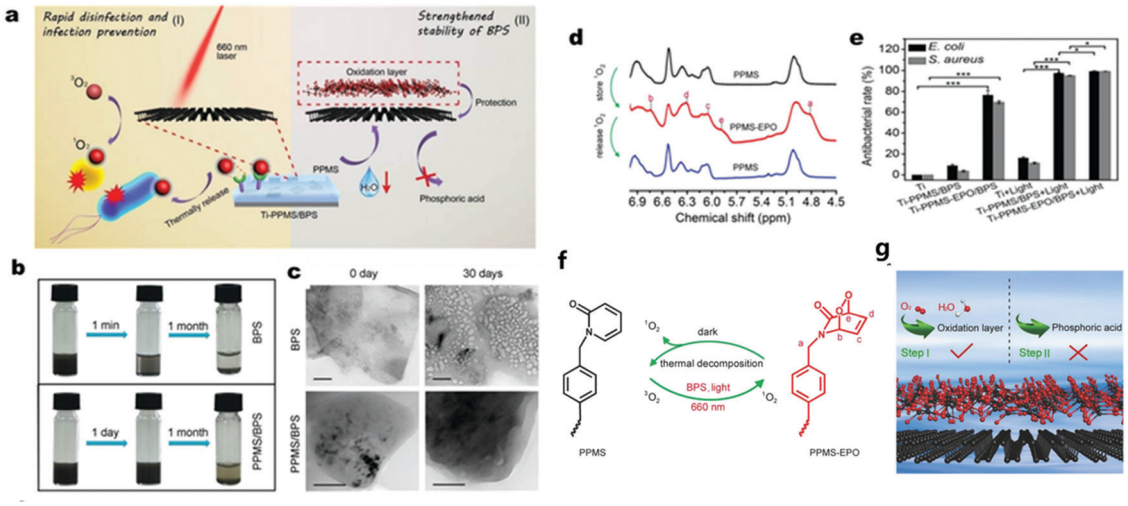

Fig. 12 Rapid bacterial inactivation and strengthened chemical stability of PPMS/BPS. (a) Schematic illustration of PPMS/BPS bacteria disinfection by singlet oxygen ($^1O_2$) with and without light, respectively. (b) Images of long-period dispersity and stability of PPMS/BPS in comparison to that of BPS. (c) Change in TEM characteristics of BPS and PPMS/BPS after one month. (d) ^1H NMR spectra of PPMS and PPMS-EPO illustrating their reversible structure change. (e) Antibacterial rate results for two different bacteria. (f) Mechanism of the reversible $^1O_2$ storage and release between PPMS and PPMS-EPO. (g) Graphical abstract of the protection of BPS with outer PPMS layers. Reprinted from ref. 136.

Table 1 Comparison of pristine semiconductors with different conditions for bacterial inactivation

Semiconductor	Type	Morphology	Preparation methods	Model bacteria	Initial condition 1 (CFU mL^{-1}) 2 amount of photocatalyst	Light condition		Inactivation efficiency	Radicals				Ref.
						λ (nm)	LPD (mW cm^{-2})		$^{\bullet}OH$	$^1O_2$	$O_2^{\bullet-}$	H_2O_2	
TiO_2	n	Nanoparticles	P25, purchased from Degussa Co.	*E. coli*	1: from 4.4×10^5 to 8.4×10^5 2: 1.0 g L^{-1}	300 to 420	NA	>99.9% for 2.25 log within 120 min	✓	NA	✓	✓	235
TiO_2	n	Film layers	Sol–gel approach	*Bacillus subtilis*	1: 10^7 2: P25 (10 g L^{-1})	UV light 310–390	40	>99.9% within 30 min	✓	NA	✓	NA	236
TiO_2	n	Nanosheets	Hydrothermal method	*S. mutans*	1: 1700 × g 2: 0–0.4 mg mL^{-1}	UV light at 365 nm	2.5	30 min	✓	NA	✓	NA	237
ZnO	n	Nanoparticles	Temperature and solvothermal synthesis	*S. aureus* strain	1: 1×10^8 (OD = 600 nm) 2: 5 mM, 60–420 μL	300–400	NA	99% within 6 h	✓	NA	✓	✓	238
ZnO	n	Flowers	Co-precipitation process	*P. aeruginosa*	1: 1×10^8 (OD = 600 nm) 2: 83.3 mM, 60 mL	Visible light	100	Completely inactive within 45 min	✓	NA	✓	NA	239
Fe_2O_3	n	Nanofilms	Electrochemical anodization of steel	*P. aeruginosa*	1: 2.0×10^7 2: 1 cm^2 film	Visible light ≥400	100	99.9% within 6 h	✓	NA	✓	NA	240
CuO	p	Powder	Sol–gel method	*E. coli*	1: 1×10^8 2: 6.15 μg	90%, ≥400	29.2	100% within 3 h	✓	NA	✓	✓	73
MoS_2	p	QDs	Sonication and solvothermal treatment of bulk MoS_2	*E. coli*, *S. aureus* subsp.	1: 1×10^6 2: 50 μg mL^{-1}	Visible light	NA	Less than 40% within 1 h	✓	✓	✓	NA	241
MoS_2	p	a: few-layered nano film b: bulk	*In situ* growth	*E. coli*	1: 1×10^6 2: from 0.1 g L^{-1} to 2 g L^{-1}	Visible light	NA	a: >99.999% b: 54% within 120 min	✓	✓	✓	✓	123
Cu_2O	p	Nanoparticles with 10 nm	Chemical deposition method	*E. coli*	1: 2×10^5 2: from 5 to 200 μg mL^{-1}	≥400	100	100% within 80 min	✓	NA	N	✓	242
Cu_2O	p	Films	Electrochemical deposition	*E. coli*	1: 2×10^7 2: NA	≥400	1200	100% within 6 h	N	N	N	✓	243
g-C_3N_4	n	Mesoporous	Self-condensation reaction of cyanamide	*E. coli K-12*	1: 2.5×10^6 CFU mL^{-1}, 100 mL 2: 1 mg mL^{-1}	Visible light (≤465 nm)	NA	100% at least 4 h	N	✓	N	✓	244
g-C_3N_4	n edges, hydrophilic groups	Nanofilms	Liquid-phase stripping method from bulk g-C_3N_4 powder	*S. aureus*, *E. coli*	1: 11.4 CFU cm^{-2} 2: 10 mg mL^{-1}	Visible light	30	93.7% ± 2.7% was removed by 0.62 J dosage for 120 min	✓	NA	✓	✓	245
RP	p	Nanosheets	Hydrothermal purification	*E. coli*	1: 0.5 $\log_{10}$ 2: 0.13 g mL^{-1}	Visible light	193	Complete inactivation was obtained within 60 min	✓	✓	✓	✓	246
BP	p	Nanosheets	Basic solvent exfoliation from bulk BP	*E. coli* and *S. aureus*	1: 10^7 2: 0.01–5 mg L^{-1}	LED light irradiation	5	>80% for all concentrations and 100% for 5 mg L^{-1} within 3 h	N	✓	N	NA	127

"NA" stands for "not analyzed during the study"; "✓" means can be detected during the study of role of ROS; and "N" refers to "not detected" or "not responsible for the photocatalytic bacterial inactivation" as proven by experiments.

remains a major strategy to proliferate their active sites due to the greater contact between semiconductors and reactive substrates and additional edges,[118] which can be achieved by morphology regulation from bulk to 2D counterparts. It has been reported that numerous exposed surface atoms in ultrathin 2D nanosheets tend to escape from the lattice, leading to the creation of defects.[80] Structural defects and disorder will cause a decrease in the coordination number of the central atoms, affecting the electronic structure and the activity of the reaction sites (Fig. 8).[119]

Due to their wide active edges, high charge carrier separation and special surface area, thin-layered nanosheets are capable of enhancing the photoproduction of multiple ROS, and ROS-induced oxidative stress has been proven to play a principle role in the disinfection mechanism.[121] For example, 2D MoS_2 nanosheets with few layers possess stronger inactivation behaviors in the presence of visible light compared with bulk MoS_2,[122] implying that the photocatalytic disinfection effects of MoS_2 materials can be improved by reducing their layer thickness and lateral size. According to Chong,[123] four types of ROS ($O_2^{\bullet-}$, $^1O_2$, $^\bullet OH$ and H_2O_2) were detected in MoS_2-based materials (Fig. 9(A)), among which H_2O_2 possess the strongest antibacterial ability (Fig. 10).

For their further application in the biomedical field, photocatalytic antibacterial agents should possess low cytotoxicity to avoid tissue inflammation or toxicity and high biodegradability with nontoxic decomposition products *in vivo*.[125,126] The degradation product of BP exists in form of $P_xO_y^{n-}$, which are nontoxic towards cells,[127] endowing the material low cyto-toxicity. Besides, it was revealed that BP can somehow reduce inflammation by down-regulating inflammatory cytokines such as IL-6 and up-regulating regenerative cytokines such as IL-10.[128] Besides, BP has good photo-thermal bacterial inactivation,[128] which may exhibit a synergetic effect on disinfection. It should be noted that unlike other common photocatalysts, the photo-excitation process of BP mainly produces $^1O_2$ upon excitation by O_2 (triplet oxygen) rather than $O_2^{\bullet-}$ or $^\bullet OH$ to achieve photocatalytic activity (Fig. 11).[127]

3.3.3 The deficiencies and limitations. Although the above-mentioned 2D semiconductors possess very different merits for photocatalytic disinfection, they still have some limitations as pure components. For example, the zero band gap property of graphene (including graphene oxide) impedes its application as a photocatalyst given that it is unable to generate photo-induced electrons or holes.[130,131] Besides, the carrier mobility MoS_2 displays a strong temperature and density dependence at low temperature ranges,[132,133] which suggests that it may not be an ideal photocatalyst. Also, BP nanosheets (BPS) suffer from poor chemical stability given that they tend to degrade in ambient oxygen and water, leading to unstable photocatalytic activity.[134,135] Therefore, strategies have been investigated to protect BPS from being oxidized.[135] For example, Wu *et al.*[136] reported poly(4-pyridonemethylstyrene) (PPMS) wrapped in the external layer of BPS to strengthen chemical stability of BPS and realize the storage and thermal-responsive release of photo-generated $^1O_2$ for on-demand antibacterial activity. Besides, PPMS was detected to capture some of the photo-generated $^1O_2$ *via* their reaction and later restore $^1O_2$ in the form of PPMS endoperoxide (PPMS-EPO). The stored $^1O_2$ was released through the reduction of PPMS-EPO to PPMS by thermal decomposition in the dark, which explained why the composite showed a disinfection effect even without irradiation (Fig. 12) and Table 1.

4. Semiconductor hybrid composites for enhanced photocatalytic bacterial inactivation

4.1 Noble metal-doped hybrid composites

4.1.1 The electron transfer and plasmonic effects of metal-semiconductors. Noble metals (Au, Ag, Ru, Ir, Pt, *etc.*) refer to metals with strong chemical inertness.[138] It has been proven that metals loaded on semiconductor materials as co-catalysts can significantly improve their photocatalytic performances by promoting the mobility of electrons,[139,140] and thus recent research has been focused on modifying pristine semiconductors.

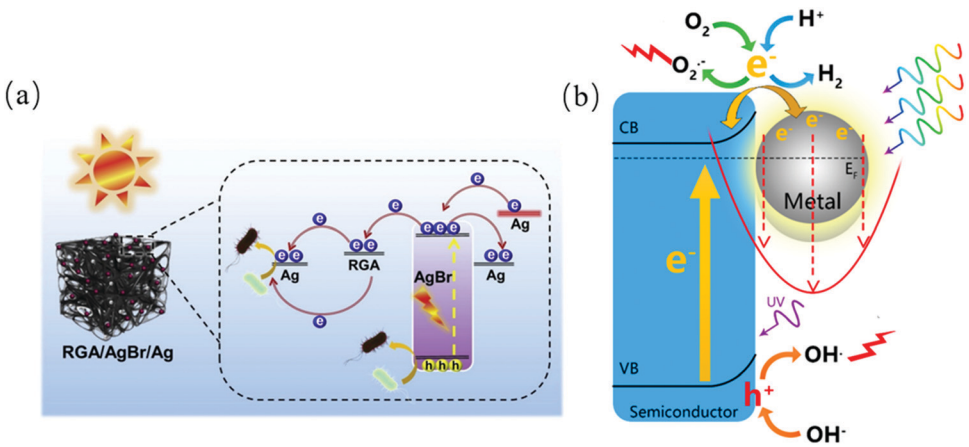

Fig. 13 (a) Schematic illustration of electron transfer in Ag-deposited RGO/AgBr photocatalyst[141] and (b) plasmonic-mediated photocatalysis.[147]

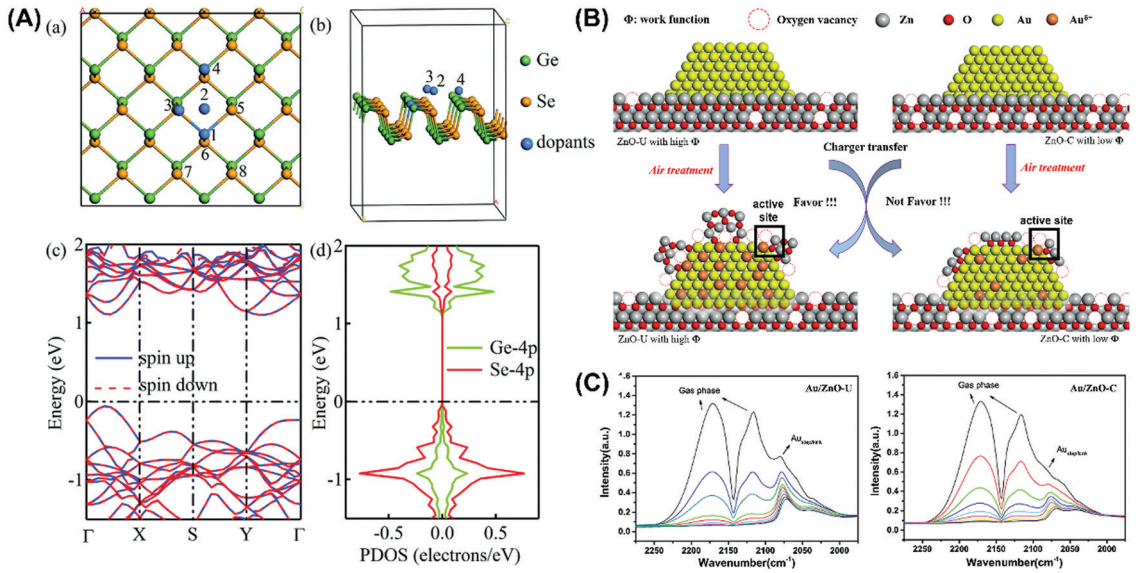

Fig. 14 Mechanism of dopant sites and creation of active sites for the introduction of noble metals. (A) Crystal lattice structure of noble metal-doped GeSe. (a) and (b) Location of doped metals with different perspectives. (c) Band structure and (d) partial density of states (PDOS) of monolayer GeSe. (B) Creation of active sites after Au doping with oxygen vacancy. (C) *In situ* FTIR spectra of CO adsorption for the study of adsorption sites and valence states of Au catalyst. (A) Reprinted from ref. 158. (B) and (C) reprinted from ref. 160.

For instance, Xin *et al.* confirmed that Ag nanoparticles deposited on a graphene oxide aerogel (RGA) can be applied as an electron delivery medium for improving the transfer of charge carriers.[141] Baig's team[142] used palladium-decorated silicon carbide (Pd–SiC) to inactivate sulfate-reducing bacteria (SRB). Pd–SiC showed superiority to SiC nanoparticles in photocatalytic disinfection, which can be attributed to the synthesis of Pd–SiC junctions, resulting in an increase in the separation of photo-generated charge carriers. Also, it exhibited a decrease in energy gap through the characterization of its diffuse reflectance spectra (DRS). Besides, some studies also indicate that more tight contact can be achieved between the atomic metal and semiconductors than that of metal clusters and semiconductors, which enhance the charge transfer for catalytic reactions.[143,144] The localized surface plasmonic resonance (LSPR) of noble metals have proven to be inducible in solar photocatalysis. LSPR is defined as specific oscillations of electrons and electromagnetic fields,[145] where a metal nanostructure strongly absorbs photon energy. Also, the plasmonic effect on photocatalysis can be classed as photon enhancement, hot electron injection and near-field enhancement.[146,147] For example, Yu *et al.* designed a plasmonic nanostructure with three

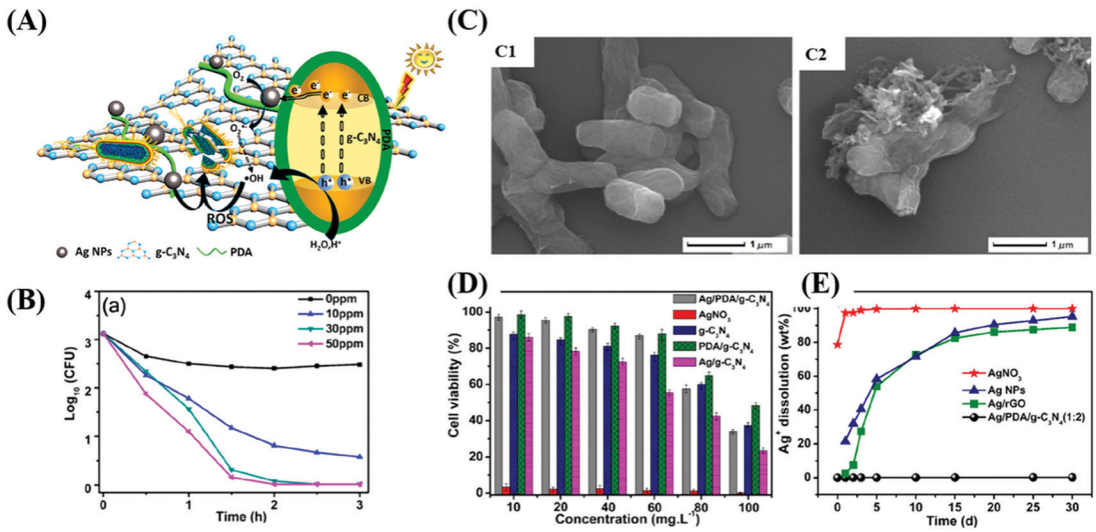

Fig. 15 Scheme showing the composition and biological performance of Ag/PDA/g-C_3N_4 photocatalysts. (A) Synthesis of the material *via* thermal treatment and *in situ* polymerization. (B) Disinfection curve of bacteria co-cultured with different concentrations of reagents. (C) Change in SEM image of *E. coli* after incubation with reagents. (D) Cytotoxicity of HUVEC cells treated with different materials. (E) Release of Ag^+ from different materials. Reprinted from ref. 180.

Table 2 Systematic review of the recent publications, showing the best doping of noble metals and ROS generation from different NPs

Num.	Materials	Powder size in diameter	Fabrication methods or main process	Wavelength range of light	Forms of noble metals	The mechanism for bacteria death	The (best) loading of metals	ROS				Ref.
								$^{\bullet}OH$	$O_2^{\bullet-}$	$^1O_2$	H_2O_2	
1	Ag/PDA/g-C_3N_4 nanoparticles	3.6 nm of AgNPs in Ag/PDA(1 : 4)-g-C_3N_4; 8.0 nm of AgNPs in Ag/PDA (1 : 2)-g-C_3N_4; 10.5 nm of AgNPs in Ag/PDA (1 : 1)-g-C_3N_4	Thermal treatment and *in situ* polymerization method	Visible light	Ag^+/Ag^0	Electrostatic adsorption, ROS generation; damage of *E. coli* bacteria cell membrane	21.3 wt% Ag/PDA (1 : 2)-g-C_3N_4	✓	✓	NA	✓	180
2	TiO_2/ACF–Pt electrode	<100 nm of Pt particles electrode	Ion sputtering and coating operation	UV light, <385 nm	Pt^0; Pt^{2+}; Pt^{4+}	ROS generation and ion release of Pt; damage to the plasma membrane *P. expansum* spores	NA	✓	✓	NA	NA	166
3	Ag/ZnO nanoparticle	~20 nm of Ag nanoparticle	Preparation of ZnO *via* solution combustion method, and adding $AgNO_3$	Under natural sunlight with 0.753 kW m^{-2} of average solar intensity	Ag^+/Ag^0	ROS generation and ion release of Ag; disruption of cell membrane and invasion of DNA structure	1 atom%	✓	N	NA	✓	248
4	RGA/AgBr/Ag nanofilm	80 nm of AgBr; too small to observe Ag in SEM	Low-temperature chemical reduction method	Visible light, $\lambda >$ 400 nm	Ag^+/Ag^0	ROS generation and ion release of Ag; *E. coli* rupture	NA	✓	✓	NA	NA	141
5	Bi_2MoO_6/Ag–AgCl microsphere	NA	AgCl sediment and Ag photoreduction on the surface of Bi_2MoO_6	Solar simulator 300 W Xe lamp	Ag^+/Ag^0	Surface plasmon resonance of Ag, ROS generation; destruction of *E. coli* cells membrane, and leakage of intracellular components	Mass ratio of AgCl to Bi_2MoO_6 is 15%	✓	N	NA	NA	249
6	Pb–$BiFeO_3$/rGO nanoparticle	3.1 nm of Pb–$BiFeO_3$/rGO	Hydrothermal method	Visible-light irradiation ($\lambda \geq$ 400 nm)	Pb^{2+}, Fe^{3+} Bi^{2+}/Bi^{3+}	ROS generation, the release of Bi^{2+}, Fe^{3+} and Pb^{2+}; cell membrane damage, nucleic acid and protein leakage	5 wt% rGO ($PbBiFeO_3$–0.5% rGO)	✓	N	N	N	250
7	Ag–Au/ZnO	4–100 nm of Ag–Au/ZnO	Precipitation-decomposition method	In nature visible light	Ag^+/Ag^0	ROS generation membrane damage	Au-1 wt% and Ag-5 wt%	✓	✓	NA	NA	251
8	Ag/TiO_2 nanofibers	NA	Mainly hydrothermal synthesis	Visible lamps (Goodly, F8T5/D 8 W)	Ag^+/Ag^0	ROS generation, the release of Ag^+; damage the cellular membrane and cause osmotic pressure imbalance of *S. aureus* and *E. coli*	5 mol%	N	✓	NA	NA	252

"✓" indicates the corresponding type of ROS ($^{\bullet}OH$, $O_2^{\bullet-}$, $^1O_2$, and H_2O_2), "N" indicates no significant ROS detected, and "NA" means "not available" or not provided in the literature.

components(CdS/Au/$SrTiO_3$),[148] where hot injections were injected from Au to the neighboring CdS/$SrTiO_3$, enabling a hot electron-assisted energy cascade for electron transfer, and thus photon absorption enhancement. The enhanced near-field amplitude effect applies to the case of insulation between a plasmonic metal and semiconductor. For instance, Wang *et al.* synthesized a plasmonic Au/TiO_2/Au couple for electromagnetic enhancement (Fig. 13).[148]

4.1.2 The active sites and optimal doping. Given that photoinduced reactions mainly occur on the surface of nanoparticle catalysts and are dominated by surface atoms,[143,149,150] the electron transfer between semiconductors and doped metal atoms may cause the surface metal atoms to act as electron-rich or electron-deficient active sites for the adsorption of reactants or desorption of products, and consequently enhance the catalytic performance.[151] Huang *et al.*[144] successfully synthesized monatomic silver chains from Ag particles *via* a simple thermal method. Also, this single-atom catalyst allowed the effective activation of lattice oxygen and oxygen molecules. Our team prepared a series of metal clusters that showed very surprising photochemical performances.[152–157] It was found that the doped metal atoms can exist either as substitutes for the original metal atoms or adsorbed on the surface. For example, He *et al.*[158] discovered that metal dopants were inclined to occupy the Ge sites rather than adsorb on the surface of GeSe (Fig. 14) and doping increased the oxidation of photogenic holes and/or the reduction of photogenic electrons. It was proven that the electron-deficient structure induced by black phosphorus-modified Pd nanoparticles improved the catalytic activity,[151] and the redox cycle formed between Pd^0 and Pd^{2+} also enhanced the activation of oxygen.[159] Besides, the interface between dopants and the semiconductor is also worth studying. According to Li *et al.*,[160] the insertion of Au into the ZnO lattice at the Au/ZnO interface leads to the formation of vacancies in the subsequently generated oxygen due to the charge mismatch, which increases the number of active sites on the catalyst surface. Nevertheless, it should be mentioned the strategy of metal doing has some disadvantages such as high cost, poor thermal stability and tightly controlled concentration of metals,[161,162] where excess metal can act as recombination centres, leading to a decline in quantum efficiencies. It was reported an Au content in the range of 1 to 5 wt% shows efficiency within 3% deviation,[162,163] which decreases once it exceeds 8 wt%.

4.1.3 ROS generation for antibacterial activity and biocompatibility. Studies on the use of metal-loaded semiconductors for bacterial disinfection have been widely reported.[164–167] However, they rarely discussed biosecurity issues, where the release of metal ions is beneficial for synergistic disinfection, but leads to an increase in toxicity.[168,169] Compared to other applications, photocatalytic sterilization demands higher requirements because photocatalysts have potential to be used in the disinfection of biological and medical devices.[170,171] International supervisory agencies have created serial nanomaterial supervisions and regulations,[172] through which the regulation, adaptability, biosafety and biocompatibility[173,174] of photocatalytic materials will need to be considered,[175] such as low cytotoxicity,[176] the controlled release of drug or metallic ions,[170] green synthesis of photocatalysts,[175] and stability and reusability.[174,177] It has been confirmed that cell death is probably due to the damage of the cell membrane integrity driven by photogenerated ROS, which can induce the release of components in bacteria, such as ions, phospholipids and proteins.[178,179] As shown in Fig. 15, Wu's team[180] synthesized a sterilized material silver/polydopamine/graphitic (Ag/PDA/g-C_3N_4), in which PDA/g-C_3N_4 was used as the carrier of silver to control the release of Ag^+. The modified PDA not only could promote the dissolvability and dispersibility of the graphitic, but was beneficial for the deposition of small-sized and highly dispersive Ag NPs. The Ag NPs contributed to the promotion of the photo-excited capacity of the system by broadening the range of light absorption and narrowing the energy gap.[181] It was indicated that $^{\bullet}OH$ and $O_2^{\bullet-}$ radicals are the dominant photoexcited radicals in disinfection by damaging the bacterial membrane. Also, the composite showed good cytocompatibility and hypotoxicity as evaluated by MTT assays and the detection of dissolved Ag^+ (Table 2).

4.2 Ion-doped hybrid semiconductors

Among the various photocatalysts, metal-oxide semiconductors have been widely applied due to their outstanding physicochemical properties.[182] Nevertheless, most oxide-based semiconductors are not accessible for the production of H_2 due to their very low CB edge position or optical light absorption due to high edge location of the VB, especially for d^0 transition metal oxides, which mainly depend on the O2p orbitals (>3.0 eV).[183,184] According to current research, doping has become one of the most effective strategies applied for the band structure modification, and therefore photocatalytic performance enhancement of semiconductors especially oxide-based semiconductors (Table 3).[185,186]

4.2.1 Cation-doped hybrid semiconductor photocatalysts. Metal cation doping enables the promotion of the photocatalytic effects of semiconductors by reducing their photogenerated charge carrier recombination rates, extending their photon absorption to the visible range and enhancing the interfacial charge-transfer reactions.[18,187] Choi *et al.*[188] demonstrated that doping with some transition metal cations could significantly improve the photoactivity of TiO_2, and a redshift occurred in the energy gap transition as the doping concentration increased, narrowing the band gap. However, they also discovered[188] that the introduction of Co^{3+} and Al^{3+} reduced the photoactivity for some catalytic reactions due to the reduction in quantum yields obtained during continuous wave photolysis. It was shown that metal ions could be incorporated into the TiO_2 lattice *via* substitution for certain Ti^{4+} ions, subsequently forming defects and oxygen vacancies.[189] Also, the ions can function as charge carrier traps, resulting in the inhibition of their recombination.[190,191]

$$M^{n+} + e_{cb}^{-} \rightarrow M^{(n-1)+} \quad \text{electron trap}$$

$$M^{n+} + h_{vb}^{-} \rightarrow M^{(n+1)+} \quad \text{hole trap}$$

Table 3 Anion/cation dopedsemiconductors and their inactivation activity

Doping type	Photocatalyst	Synthesis method or main process	Doping mechanism	Anion amount	Band gap (eV)	Photocatalytic antibacterial activity	Antibacterial mechanism	Ref.
Cation	Zr–Ag-*co*-doped TiO_2	Sol–gel method	Narrows the energy gap, inhibit charge carrier regeneration	5% mol silver and 10% mol zirconium	/	Complete inhibition of *E. coli* within 20 min under fluorescent light	Zr^{4+} increases adhesion; the toxicity of Ag^{+}; the photogenerated ROS	196
	Cu-MOFs	Hydration heating	Introduced Cu^{2+} can serve as the trap of charges	10 molar ratio Cu^{2+}	/	99.71% *S. aureus* was inactivated within 20 min	MOFs increase membrane permeation; synergistic effects of ROS and heat	256
	Fe^{3+} and Pb^{2+} co-doped zinc oxide	Microwave-assisted hydrothermal method	Forms defects in the crystalline lattice of TiO_2	8% Fe^{3+} and Pb^{2+}, respectively	3.15 → 3.06	Microwave-assisted hydrothermal method	Hydrophobicity of ZnO, electrostatic interaction	257
	Cd/Fe-*co*-doped zinc oxide	Sol–gel method	Replaces Zn^{2+} ions by cations and create defects in the pure ZnO crystalline structure	4% doping of (Cd, Fe) content	/	High inhibition activity of *P. aeruginosa* and *B. flexus*	Release of Zn^{2+} and ROS	258
	Cu-doped zinc oxide	Simple solvothermal route	Narrows the band gap by electronic transition	3.13 molar ratio of Cu ions	3.20 → 2.74	Complete inhibition of *E. coli* under visible light for 4 h	Release of Zn^{2+} and ROS, the rupture of cell membrane, inhibits growth.	194
	Mg^{2+}-doped TiO_2	High-energy ball milling	Forms defects in the crystalline lattice of TiO_2	20% Mg^{2+}	3.01 → 2.94	*E. coli* inhibition rate of 66.8%; *S. aureus* inhibition rate of 61.1%	The toxicity of Mg^{2+}; the presence of Ti^{3+} and Ti^{4+} enhances material photocatalysis; ROS	259
	La^{+} doped-TiO_2	High-energy ball milling	Forms defects in the crystalline lattice of TiO_2	10% La^{+}	3.01 → 2.95	*E. coli* inhibition rate of 87.4%; *S. aureus* inhibition rate of 80.7%	The toxicity of La^{+}; Ti^{3+} and Ti^{4+} enhance material photocatalysis; the presence of ROS	259
Anion	C–B co-doped TiO_2	Sol–gel technology	Narrows the band gap	/	3.21 → 3.16	High inhibition activity of *E. coli* and *S. aureus*	TiO_2(B) phase and B_2O_3 phase benefit antibacterial effects; the photogenerated $^{\bullet}OH$	260
	F&N co-doped TiO_2	Wet milling process	Surface fluorination and interstitial doping	F and N are (i) 7.45 at% and 2.83 at%, respectively	/	Complete inhibition of *E. coli* ($\sim 4.1 \times 10^6$ CFU mL^{-1}) within 60 min; light source: 4.2 mW cm^{-2}	The photogenerated ROS, especially $^{\bullet}OH$	212
	N-doped ZnO	Self-assembly combustion	Narrows energy gap with the blending of the 2p state of O	1.04% nitrogen content	/	Significant bacteriostatic zone with lamp illumination	The introduction of nitrogen could significantly enhance the antibacterial performance of ZnO nanocrystals	213
	C-doped anatase-rutile nano-heterojunctions	Microwave-assisted technique	C 2p states benefit band gap narrowing	/	3.16 → 2.90	C-doped nanoheterojunctions had a higher disinfection rate compared with the standard photocatalyst (0.0023 min^{-1} and −0.0081 min^{-1}, respectively)	Photogenerated ROS	261
	Cl-doped TiO_2	Atomic layer deposition	/	4% Cl content	/	Reduction in CFU of *C. albicans* up to 59.5% after UV treatment	Toxicity of Cl^{-}, photocatalytic activity	262
Cation/anion co-doping	Cu–N-*co*-doped TiO_2	Sol–gel process	Reduces the bandgap	0.75% Cu–N content	/	High inhibition activity of *E. coli* and *S. aureus*	Toxicity of TiO_2; the photogenerated ROS	263
	Mesoporous TiO_2 with Ni–S co-doping	Sol–gel method	Ni^{2+}: mingles in titanium dioxide lattice to suppress charge regeneration; sulfur: enters titanium dioxide lattice to decrease the energy gap	0.75% of Ni–0.25% of S	3.2 → 2.68	High inhibition activity of two types of bacteria	Photogenerated ROS, e^{-}/h^{+}, O_2^{-} and $^{\bullet}OH$	264
	Ta/N–TiO_2	Sol–gel method	Narrows energy band gap by mixing of N 2p and O 2p, the new form of N 2p–Ta 5d hybrid	The amount of Ta is 20 mol%	3.1 → 2.20	High inhibition activity of three types of bacteria cultured with 300 μg mL^{-1} Ta/N–TiO_2 powders for 2 h	Photogenerated charge carriers	221

Table 3 (*continued*)

Doping type	Photocatalyst	Synthesis method or main process	Doping mechanism	Anion amount	Band gap (eV)	Photocatalytic antibacterial activity	Antibacterial mechanism	Ref.
	B and Ce-*co*-doped TiO_2	Sol–gel procedure	Substitute B to occupy O sites	/	/	Bacteria cultured with materials all have large inhibition zone within 120 min	Smaller size of nanoparticle and higher specific area; broaden the range of visible-light response; surface hydroxyl groups; the toxicity produced by Ce^{3+}/Ce^{4+} ions	265
	F,Cu-*co*-doped TiO_2	Sol synthesis	Charge compensation between F^- and Ti^{4+} suppresses the regeneration of charge carriers	F: 0.3–0.5 at%, Cu: /	/	High antibacterial activity of the Cu-doped TiO_2 with or without light	Photogenerated ROS and copper ion toxicity, causing cell membrane rupture	266
	Co/F-*co*-doped ZnO	Soft chemical method	The introduction of Co and F reduced the particle size; the form of defects in the crystalline lattice	Co (1 at%) and F (1 at%)	3.32 → 3.28	Induced big zone of inhibition for four types of bacteria due to the addition of dopants	Due to the release of Zn^{2+} ions, the generation of ROS	267
	Sulfated and Eu-doped anatase	Precipitation	Formation of oxygen vacancy; Eu^{3+} dopants as an electron trap effect; lanthanoids reduce the titania band gap; increase surface area and pore volume	/	/	Effective antimicrobial action of TiO_2 nano-powders after exposure to UVA radiation within 60 min	Inactivation of intracellular proteins; local damage of cell wall	268

"/" means not mentioned.

Especially, some metal dopants (such as Fe and Cu ions) enable the creation of additional energy levels near the TiO_2 band, serving as charge traps.[189,192] Also, their enhanced response to visible light is also attributed to photo-induced interface charge shift from the holes in the VB of the semiconductor to the adsorbed ions (such as Cu(II) species) on the surface and multi-electron reduction catalyzed by their reductive species (such as Cu(I) ions).[189] For *in situ* Fe^{3+}-doped BiOCl, the doped Fe^{3+} not only acts as an "electron transfer bridge" to capture and transport electrons, but the active center of catalytic reactions.[193] Besides, the facet transition from the original BiOCl(001) to Fe–BiOCl(110) and (102) causes more exposure of the iron active sites. Various cation ion-doped hybrid semiconductors have been applied in the photocatalytic antibacterial field,[194,195] for example, Ag^+ (5% mol) and Zr^{4+} (10% mol) co-doped TiO_2 showed complete inhibition of *E. coli* within 20 min,[196] where Ag^+ and Zr^{4+} functioned to narrow the energy gap and inhibit the regeneration of charge carriers, respectively. The presence of zirconium was beneficial to increase the adhesion between the Zr–Ag co-doped TiO_2 particles and *E. coli via* electrostatic force. MOF doping with 10% Cu^{2+} (Cu_{10}MOF) strengthened the antibacterial activity and photothermal effect for bacteria-infected wounds, mainly due to the photon absorption caused by the d–d transition of Cu^{2+}[197] and its capture of electrons (Fig. 16(b and c)). Cu_{10}MOF also exhibited good biocompatibility *in vitro* and *in vivo*.[198] However, an increase in the doping concentration of Cu^{2+} (Cu_{20}MOF) resulted in an acceleration in electrons and holes regeneration and even a decline in their transfer velocity, which reduced the photocatalytic activity (Fig. 16(d)).

4.2.2 Anion-doped hybrid semiconductor photocatalysts. Vautier firstly found the that the introduction of nitrogen could strengthen the photo-degradation effects of TiO_2 towards carmine dye in the present of visible light in 2001,[200] followed by many other non-metal elements.[201–206] It has been reported that non-metal dopants are superior to most of the metal ions with less generation of recombination centers.[207] More vacancies or defects can be introduced into the original lattice after ion doping, which provide more active sites for photo-oxidation reactions.[208] For example, in N-doped ZnTe with an N-doped carbon layer,[209] the N atom inserted into the ZnTe lattice, leading to a slight reduction in the band gap and promotion of the charge transfer. Also, the N-doped carbon layers can be used as the active sites for subsequent reactions (Fig. 17(A)). In the case of N-doped TiO_2,[210] atom insertion similarly occurs in the lattice located above the conduction band and induces impurity levels with the introduction of Ti^{3+}, further narrowing the band gap (Fig. 17(B)). The enhanced response to visible light can be attributed to the presence of oxygen vacancies, Ti^{3+} and N species. Defects can serve as active sites according to the previous discussion. Kang *et al.*[211] designed a photocatalyst with inherent carbon defects (NCN/CDs) by removing N atoms, in which the defects bind to the adsorbed H_2O as oxidation sites for the formation of O_2 (Fig. 17(C)).

Non-metal dopants have been well investigated for improving the antibacterial performance of materials. For example,

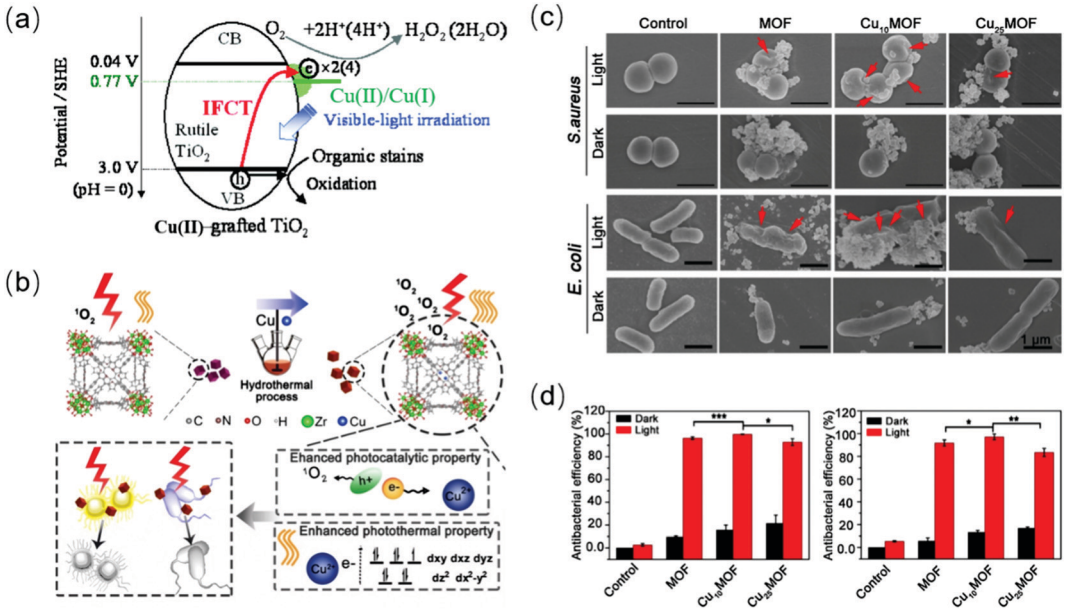

Fig. 16 Schematic illustration of the transition metal ion doping mechanism and its antibacterial effects upon exposure to light. (a) Possible photocatalytic mechanism of Cu(II)TiO_2, including interfacial charge transfer (IFCT) and multielectron reduction processes. (b) Schematic diagram of the increase in photocatalytic and photothermal effects in the system. (c) SEM images showing the destruction of the morphology and structure of bacteria cultured with Cu^{2+}-doped MOF under 660 nm light. (d) Evaluation of antibacterial action for different materials. (a) Reprinted from ref. 199. (b)–(d) Reprinted from ref. 198.

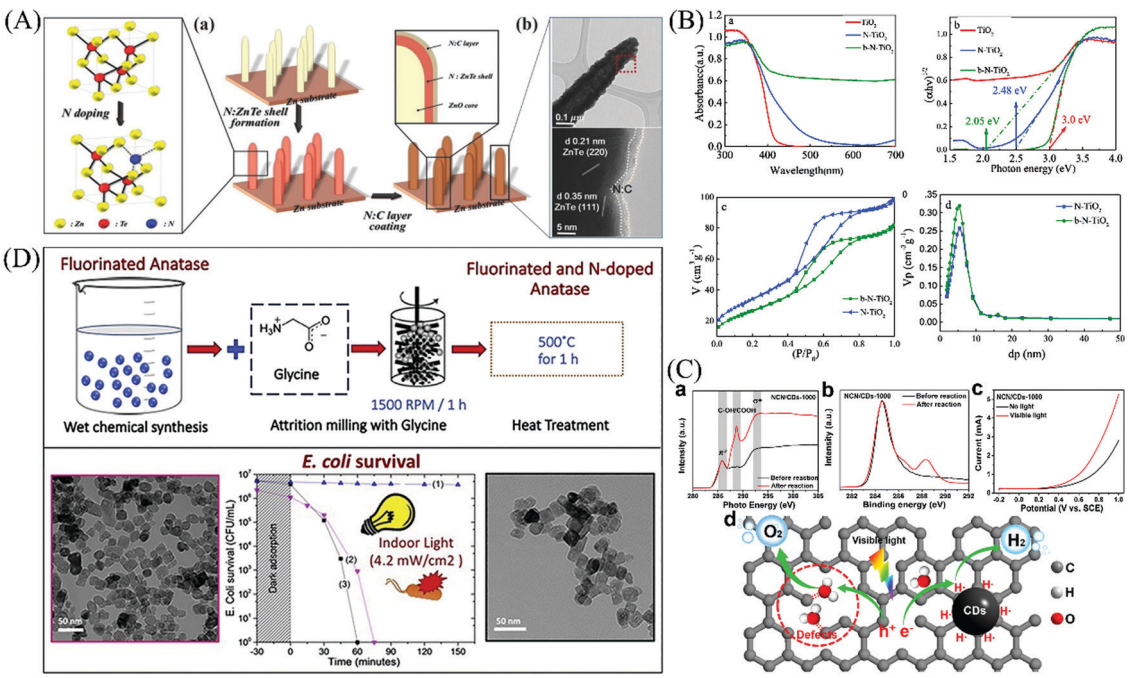

Fig. 17 Mechanism of anion-doped semiconductors. (A) Insertion of N atom in ZnTe lattice (a) and HRTEM images under low (upper) and high (below) magnification (b). Reprinted from ref. 209. (B) UV-visible solid absorption spectra (a) and band gap width (b) for N–TiO_2 systems. N_2 adsorption–desorption isotherm curves (c) and corresponding pore size distribution curve (d) of N–TiO_2 systems. Reprinted from ref. 210. (C) Photoactivation mechanism of photocatalysts with rich carbon defects. Reprinted from ref. 211. (D) Preparation and characterization of F&N-doped TiO_2 photocatalyst and its photocatalytic antibacterial effect. Reprinted from ref. 212.

Wu *et al.*[213] fabricated N-doped ZnO nano-crystallites *via* a simple self-assembly combustion technique, which showed an obvious bacteriostatic circle of bacteria cultured with materials under lamp illumination, indicating that the

incorporation of nitrogen into the ZnO lattice extended the light response and enhanced the antibacterial effect. Also, the inactivation ability of nanomaterials is mainly attributed to the photogeneration of ROS, where non-metal dopants are beneficial for the excitation of electrons through the overlap of non-metal the 2p levels and O 2p orbitals, leaving holes to produce the strongly oxidizing $^{\bullet}OH$.[214] Milosevic *et al.*[212] developed novel fluorine and nitrogen co-doped TiO_2 nanoparticles, in which the amount of fluorine reached 7.45 at%. They showed that the F&N co-doped TiO_2 was beneficial for disinfection due to its low agglomeration. It was further reported surface fluorination can help to induce the photogeneration of hydroxyl groups[215] and the formation of superficial Ti^{3+} donor energy levels located near the CB,[216] which accelerate the excitation of electrons, and therefore facilitate the continuous generation of ROS.

4.2.3 New strategy of co-doping hybrid with cations and anions. Single-element doping causes a problem in the process of photocatalytic enhancement because the doping level will become the recombination center of photo-generated charges[217] and even the impurity level formed by more discrete doping increases the migration and separation of light holes or electrons. Recent research results showed that by co-doping transition metals with non-metallic elements,[218] such as N–La,[219] S–La,[220] and N–Ta,[221] the co-doping defect level is passivated because the charge compensation of the anion and cation pairs is not likely to become a carrier recombination center.[219,222] The synergistic effects of co-doping contribute to the enhancement of photocatalysis because of the extension of the range of light absorption and low regeneration efficiency.[223]

For example, Phattalun's team[224] proposed a novel passivated co-doping method to produce vanadium–nitrogen (V–N) co-doped TiO_2, in which the V–N pair led to a reduction in the energy gap of TiO_2. V–N co-doping also has the potential to generate $^{\bullet}OH$ and $O_2^{\bullet-}$ due to the suitable band edges, which can serve as antibacterial agents.

4.3 Semiconductor hybrid heterojunctions

Although ion doping may serve as a solution to the rapid recombination of electrons and holes in semiconductor photocatalysts, it unavoidably reduces the oxidation and reduction potentials of the excited charge carriers and may be limited by the maximum doping ability, leading to an minor enhancement or even decrease in the photocatalytic bacterial inactivation.[39] Since the CdS/TiO_2 semiconductor hybrid system was firstly investigated and found to be able to transfer photogenerated electrons from the CB of CdS to TiO_2 in 1984,[225] it has become a hotspot for heterojunctions between two or three solid-state photocatalysts.[226,227] It was found that this type of transfer process can serve as a pathway for charge separation, which contributes to reducing or slowing down the recombination of charges, and therefore enhances the photocatalytic efficiency.[228,229] The past decades have witnessed the emergence of and subsequent expansion in the semiconductor hybrids for bacterial inactivation, which will be described in detail in the following sections. Besides, in the last Section 4.3.6, we discuss the heterojunctions of 2D materials, in which heterojunctions are defined and divided based on material dimensions rather than electron transport pathways, with emphasis on the interface contact effects between semiconductors with different dimensions.

4.3.1 Type II heterojunction hybrids. Typical heterojunction photocatalysts can be divided into three types depending on the band gap positions between two semiconductors (Fig. 18). According to Yu *et al.*,[230] only type-II heterojunction is efficient to enhance photocatalytic activity due to its appropriate band structure for the spatial separation of charge carriers.

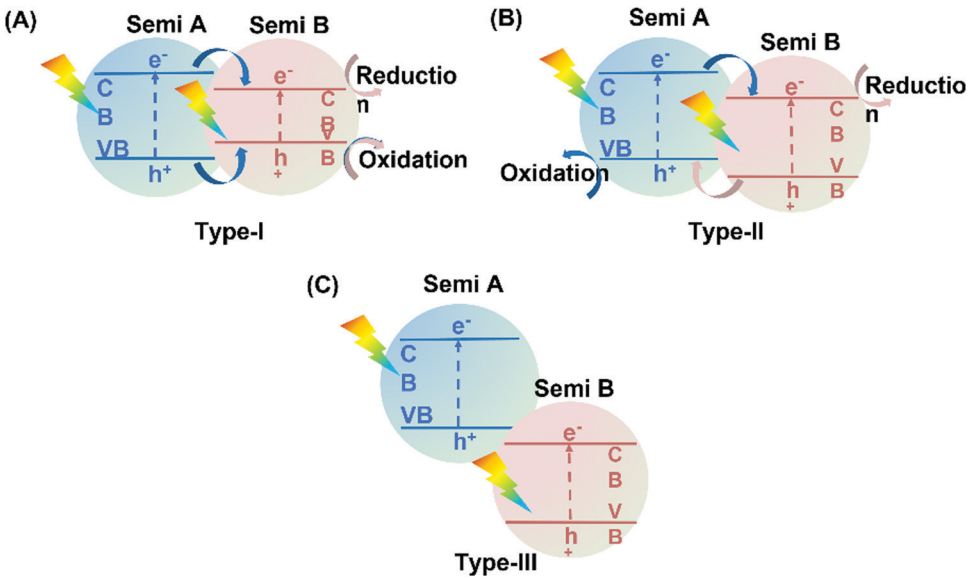

Fig. 18 Schematic illustration of electron transfer in the three different heterojunctions: (A) type-I, (B) type-II, and (C) type-III heterojunctions. Semi refers to semiconductor.

Table 4 Type II heterojunction semiconductor hybrids and their inactivation process

Semiconductor 1	Semiconductor 2	Methods	Bacteria	Light condition		Inactivation efficiency	Radicals				Mechanism of inactivation	Ref.
				λ (nm)	LPD (mW cm^{-2})		$^{\bullet}OH$	$^{1}O_2$	$O_2^{\bullet-}$	H_2O_2		
Bi_2WO_6	TiO_2	Hydrothermal method	*E. coli*	≥420	NA	100% within 4 h (for 40% TiO_2 doping)	✓	NA	✓	✓	Cell wall rupture & cellular component leakage	233
Fe_2O_3	AgBr	Electrospinning-calcination method	*E. coli K-12*	480–680	100	100% within 4 h	N	NA	N	✓	Cell membrane rupture	274
TiO_2	Cu_2O	Electrochemical deposition	*E. coli*	≥400	82	100% within 20 min	✓	NA	NA	NA	Deformation of cell membrane	275
Bi_2WO_6	$BiVO_4$	Hydrothermal method.	*P. aeruginosa*	≥420	NA	Almost all (99.99%) within 30 min	✓	NA	N	NA	Cell membrane rupture & cytoplasm leakage	276
AgBr	ZnO	Deposition–precipitation	*E. coli*	Visible light region	NA	87.5% within 315 min	✓	NA	✓	NA	Membrane degradation by h^+, $^{\bullet}OH$ and $O_2^{\bullet-}$	277
$ZnFe_2O_4$	ZnO	Thermal decomposition of precursors	*E. coli*	Visible light region	NA	100% for $ZnFe_2O_4$/ZnO with ratio 1 : 3 1 : 2 and 1 : 1	✓	NA	✓	NA	NA	278
TiO_2	CNT	Sol–gel method	*E. coli ATCC25922*	≥400	110	48% within 1 h; (BC: 21%)	✓	NA	✓	NA	NA	279
ZnO	CNT	Sol–gel method	*E. coli ATCC25922*	NA	110	100% within 10 min	✓	NA	✓	NA	NA	280
TiO_2	CeO_2	Microemulsion method	*E. coli*	350 500	1.5 kJ m^{-2}	k = 98.4; k = 9.9	NA	NA	NA	NA	NA	281
TiO_2 nanobelts	Ag_2O	Deposition-precipitation	*E. coli ATCC15597*	Visible light region	NA	Kill 4.7 log of viable *E. coli* within 3 h	N	NA	✓	✓	Cell membrane rupture	282
g-C_3N_4	α-Sulfur	Modified heat-etching method	*E. coli K-12*	UV (λ < 400 nm)	193	Kill 6 log of viable *E. coli* within 4 h	✓	✓	NA	✓	Cell membrane Degradation	283

"✓" represents that the radical was characterized and detected by ESR and the meanings of the other symbols are equivalent to that depicted in Table 1.

Type II heterojunctions have become common semiconductor photocatalysts used for bacterial inactivation,[231,232] detailed information of which can be found in Table 4. Jia[233] reported the synthesis of TiO_2–Bi_2WO_6 bi-nanosheets to increase the antibacterial activity, and systematically investigated the underlying mechanism of inactivation. In the scavenger and EPR study, it was found that both the photo-excited electrons and holes contribute to the inactivation. However, h^+ is the dominant factor. Also, as shown by the PCR and BCA assay, the components leaked were the genome and total protein. Moreover, the decrease in recombination of carriers was directly confirmed by the detection of the photocurrent, which makes it special among numerous studies. Ng[234] reported a natural-light-responsive magnetic Fe_2O_3–AgBr for the photo-induced disinfection for *E. coli* and studied the factors influencing its activity, including temperature, dissolved ions and pH. As shown by their results, at 37 °C or/and pH = 7.67, the semiconductor hybrids exhibited the best photocatalytic bacterial inactivation, but a detailed explanation how temperature and pH affect the inactivation was not demonstrated. Moreover, the existence of Ca^{2+} would promote the inactivation, while anions such as SO_4^{2-} would inhibit it given that a cation would offset the mutual repulsion between Fe_2O_3–AgBr and the bacterial membrane, both of which are negatively charged. The detailed inactivation data is shown in Table 4.

Generally, the geometrical structure of a heterojunction, especially its crystal plane, will greatly affect the charge redistribution at the heterointerface, and thus, change its photocatalytic efficiency. For example, Wu *et al.*[26] reported a novel RP/ZnO heterojunction wafery film for solar or LED-driven rapid, efficient and safe disinfection and investigated the effect of the crystal plane. It was determined that in the RP/ZnO heterojunction, the RP(001) and ZnO(002) plane had the largest charge reallocation *via* density functional theory (DFT) calculations, and therefore, exhibited the greatest stability. In this study, photo-generated e^- of the RP(001) plane jumped to the ZnO(002) plane, while h^+ generated in ZnO would transfer to the VB of RP. Compared with RP, the RP/ZnO hybrid system can generate more $^\bullet$OH *via* the oxidation of water to enhance the antibacterial effect, whereas compared to ZnO, the hybrid system had an increased response to visible light and even NIR light and ensured sufficient carrier separation. Through the combined action of $^\bullet$OH, $O_2^{\bullet-}$ and $^1O_2$, a strong and rapid inactivation effect was achieved. This study showed that ROS could sterilize bacteria by triggering the overproduction of ROS in cells and causing oxidative stress to promote bacterial apoptosis, as confirmed by DCFH. *S. aureus* has a thick cell wall, which can efficiently slow down the penetration of ROS into its cells and rupture of its cell membrane, and thus excess ROS can be more easily neutralized. However, ROS-scavenging enzymes in *E. coli* were rapidly destroyed, and thus *E. coli* was quickly overwhelmed, which explains why the hybrids showed a better and faster inactivation towards *E. coli* (Fig. 19).

Although the type II heterojunction is ideal for separating electron–hole pairs in space with potential differences between the components, the enhanced electron–hole separation is still insufficient to overcome the ultra-fast electron–hole recombination on the semiconductor.[247] Therefore, other types of heterojunctions have appeared to fill the gaps.

4.3.2 p–n heterojunction hybrids with noble metal nanoparticles. p–n heterojunctions contribute to the migration or separation of photo-generated electron–hole pairs, and therefore the photocatalytic performance.[253] Owing to their surface plasma resonance (SPR), high Fermi energy (E_f) and good antibacterial effect, noble metal nanoparticles, especially AgNPs, are widely used for the decoration of p–n semiconductor hybrids to improve their photocatalysis efficiency.

It is believed that AgNPs can be excited and generate electrons that transfer between other semiconductors. Jing *et al.* reported visible light-driven magnetic $CoFe_2O_4$/Ag/Ag_3VO_4[254] and $ZnFe_2O_4$/Ag/Ag_3VO_4[255] photocatalysts for highly efficient photocatalytic bacterial inactivation. In these systems, AgNPs generate plasma hot electrons, while Ag_3VO_4 and $CoFe_2O_4$ or $ZnFe_2O_4$ generate charge carriers. Due to the successive decline in the CB position, the electron would transfer from the AgNPs to Ag_3VO_4, and then to $CoFe_2O_4$ or $ZnFe_2O_4$. Meanwhile, the holes generated from $CoFe_2O_4$ or $ZnFe_2O_4$ would transfer to Ag_3VO_4, which greatly suppressed their recombination, and hence enhanced the photocatalytic antibacterial efficiency.

4.3.3 Z-scheme-type heterojunction hybrids. Z-scheme type heterojunctions are named after the Z-like shape of the charge process.[269] This type of heterojunction contains three parts, an electron mediator and two semiconductors labeled PS I and PS II. Generally, the semiconductor from which the photo-generated holes transfer is called PS I and the other is PS II. Z-scheme heterojunctions are currently divided into three types according to the electron mediator, including an acceptor/donor system (PS-A/D-PS system), an external conductor (PS–C–PS system) and a touch interface between (PS–PS system). Usually, in the latter two systems, the oxidation reaction occurs only in PS II and the reduction reaction only in PS I, whereas in the PS-A/D-PS system, the redox reaction can occur in both.[269] A schematic diagram of the three types of Z-scheme heterojunction hybrids is shown in Fig. 20.

Xia *et al.*[270] reported a novel g-C_3N_4/m-Bi_2O_4 PS–PS heterojunction system for enhancing the photocatalytic disinfection with a visible light source towards *E. coli* and investigated the different inactivation efficiencies caused by different ratios of g-C_3N_4 to m-Bi_2O_4, demonstrating that the optimal one was g-C_3N_4/m-Bi_2O_4 (1 : 0.5). The PL spectrum and photocurrent study further proved that the recombination process is mostly inhibited in g-C_3N_4/m-Bi_2O_4 (1 : 0.5), which directly improve its photocatalysis efficiency. Also, it is believed that the excess m-Bi_2O_4 can function as a recombination center of photo-generated electron–hole pairs to suppress the photo-induced activity when the m-Bi_2O_4 content is too high, corresponding to the higher efficiency of g-C_3N_4/m-Bi_2O_4 (1 : 1) compared to g-C_3N_4/m-Bi_2O_4 (1 : 0.5). Besides, the ROS production was also systematically investigated. Zeng *et al.*[271] successfully synthesized a highly dispersed TiO_2NC/WO_3NR/rGO composite for enhanced bacterial inactivation, which can be classified as a PS–C–PS system. Due to its excellent electron conductivity and

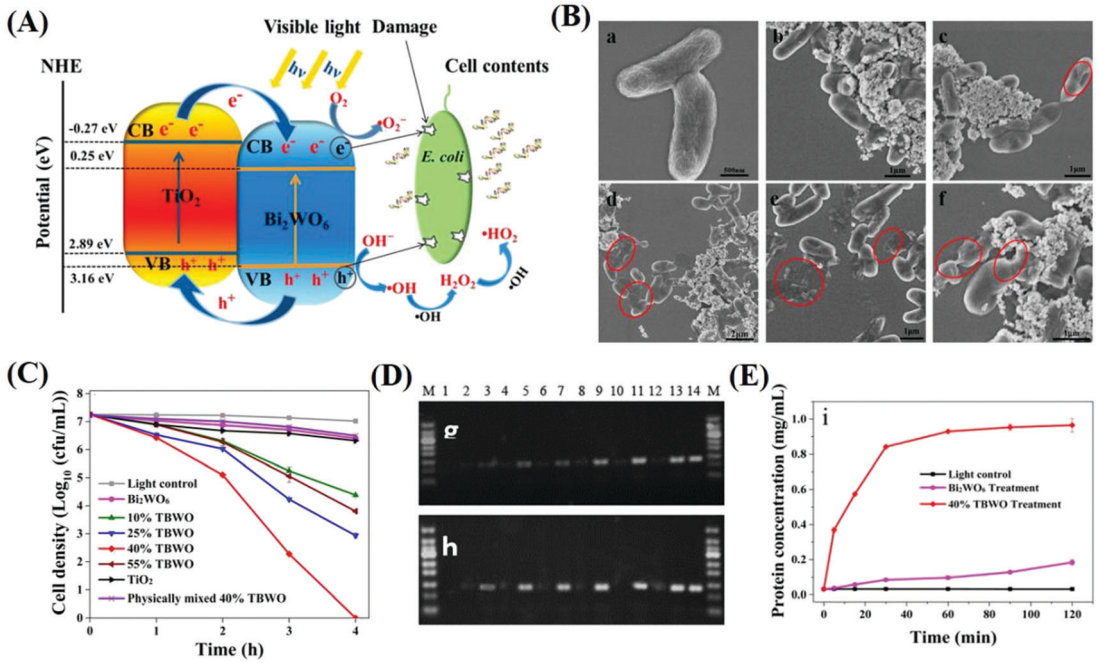

Fig. 19 Photocatalytic disinfection mechanism of a typical type II heterojunction, TiO_2-Bi_2WO_6 nanosheets (TBWO). (A) Schematic illustration of the antibacterial process of TBWO. (B) Inactivation effect of *E. coli* at different times under visible light. (C) Bactericidal kinetic curve of TBWO with different concentrations. (D) Detection of leakage of bacterial 16rsDNA and (E) total protein in *E. coli*. Reprinted from ref. 231.

mobility, the original p–n heterojunction TiO_2/WO_3 photocatalysis system would be converted into a Z-scheme heterojunction hybrid once rGO is applied. After modification by rGO, the photo-generated electrons would no longer transfer from TiO_2 to WO_3,

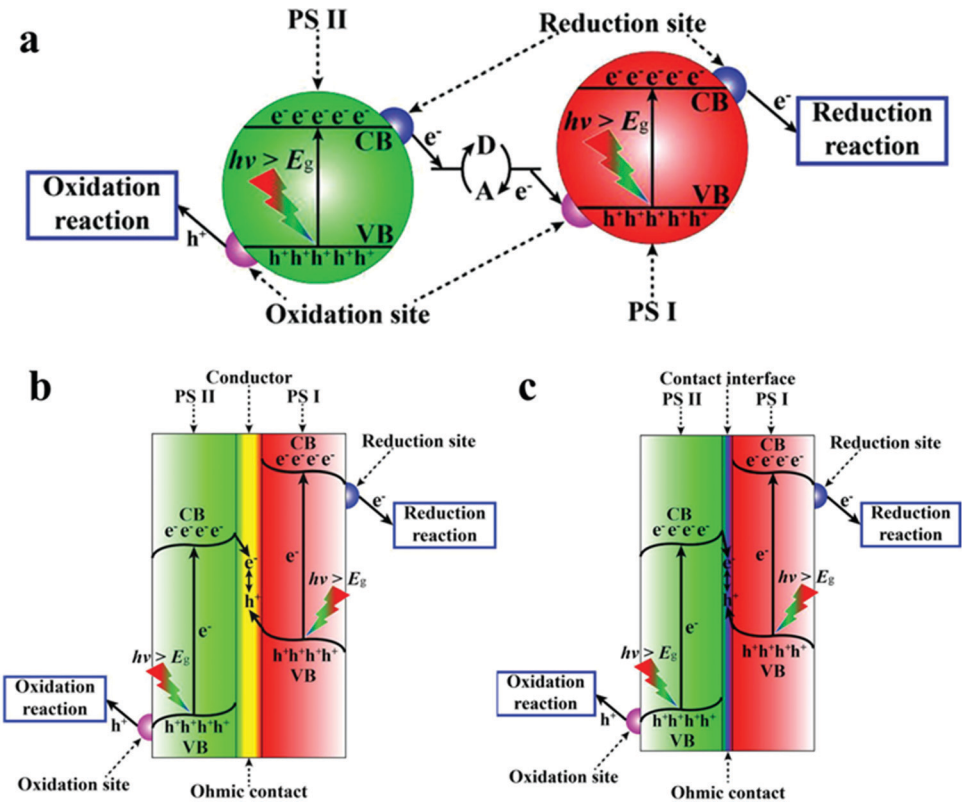

Fig. 20 Schematic diagram showing three types of Z-scheme heterojunctions: (a) PS-A/D-PS system; (b) PS–C–PS system, and (c) PS–PS system. Reprinted from ref. 269.

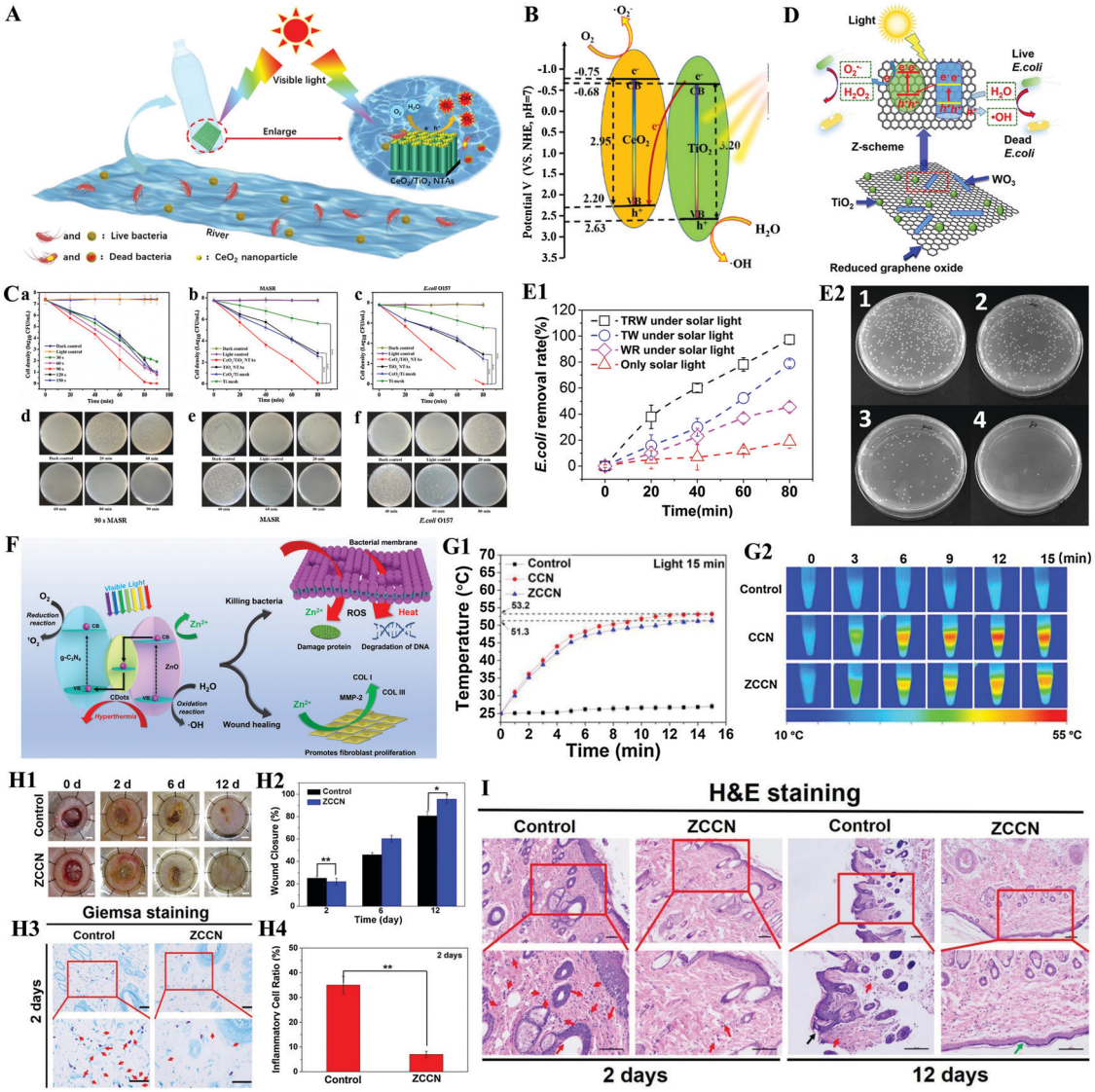

Fig. 21 Schematic illustration of the band structure and photocatalytic antibacterial behaviors for 3 types of Z scheme heterojunctions. (A) and (B) Band structure and photoinduced behaviors of the CeO_2/TiO_2 direct PS–PS heterojunction. (C) Time-dependent antibacterial effects of CeO_2/TiO_2 materials under different conditions. (D) Band structure and photoinduced behaviors of TiO_2/rGO/WO_3 heterojunction (PS–C–PS system). (E1) Antibacterial dynamic curve and (E2) antibacterial plate experiments of TiO_2/rGO/WO_3 system for different times. (F) Band structure and photoinduced behaviors of ZnO/CDot/g-C_3N_4 heterojunction (PS-A/D-PS system). (G1) Photothermal curves with visible light irradiation and (G2) corresponding infrared thermal photos for different materials. (H1) Photos of *S. aureus*-infected wounds treated/not treated with ZnO/CDots/g-C_3N_4 for different times and (H2) corresponding size of the wound. (H3) Infections in wound after 2 days of treatment showed by Giemsa staining images. (H4) Inflammatory cell ratio calculated from H&E staining data. (I) Skin tissue infections showed by H&E staining images at 2 and 12 days. (A)–(C) Reprinted from ref. 273. (D) and (E) Reprinted from ref. 271. (F)–(I) Reprinted from ref. 272.

whose CB is at +0.4 V and more positive than −0.33 V, the redox potential for $O_2^{\bullet-}/O_2$, in which case O_2 could not be reduced to $O_2^{\bullet-}$. Instead, the electrons generated by TiO_2 remained in its CB, the potential of which can thermodynamically produce both $O_2^{\bullet-}$ and H_2O_2. Wu *et al.*[272] synthesized a novel PS-A/D-PS system-ZnO/CDots/g-C_3N_4, in which CDots efficiently inhibited the recombination of photogenerated charge carriers, which served as electron mediators. This Z scheme heterojunction possessed photoresponsive antibacterial properties for synergistic effects by photoinduced ROS inactivation and photothermal therapy (CDots serve as photothermal material), resulting in the accelerated healing of infected wounds due to the release of Zn^{2+} with a promoting effect on cell proliferation (Fig. 21).

The other Z-scheme heterojunction hybrids and their detailed bacterial inactivation data are shown in Table 5.

4.3.4 S-scheme heterojunction hybrids. Type II heterojunctions separate photogenerated charges *via* the electric potential differences between their components because this type of heterostructure reduces the redox capacity of photogenerated electrons and holes.[290] For p–n heterostructures, this also causes the redox capacity for the reduction and oxidation processes occurring on semiconductors to have lower reduction

Table 5 Z-scheme heterojunction hybrids and their inactivation

PS I	PS II	Electron mediator	Preparation method	Model bacteria	Initial condition 1: (CFU mL^{-1}) 2: (mg)	Light condition		Inactivation efficiency	Radicals				Ref.
						λ (nm)	LPD ($mW\ cm^{-2}$)		$^{\bullet}OH$	$^{1}O_2$	$O_2^{\bullet-}$	H_2O_2	
g-C_3N_4	m-BiO_4	—	Hydrothermal	*E. coli K-12*	1: 1×10^6 2: 50	≥400	193	100% within 1.5 h (for g-C_3N_4 : Bi_2O_4 = 1 : 0.5)	GI	NA	#	GI	270
AgI	$BiVO_4$	—	Deposition-precipitation	*E. coli ATCC 25922*	1: 7×10^7 2: 20	≥420	NA	100% within 50 min (for 9.09% AgI contained)	NA	NA	N	N	284
TiO_2	WO_3	rGO	Hydrolysis-hydrothermal	*E. coli ATCC 11775*	1: 2×10^3 2: 30	Solar light	NA	97.3% within 80 min	GI	NA	SI	GI	271
g-C_3N_4	$Mg_{1.2}Ti_{1.8}O_5$	—	Sol–gel and ionothermal method	*E. coli*	1: 5×10^7 2: 0.01 mol	Solar light	300 W	100% over 100 min	GI	NA	GI	NA	285
AgBr	Ag_3VO_4	AgNPs	Ionic liquid-assisted precipitation	*E. coli*	1: 1×10^7 2: NA	≥420	NA	Almost all (99.99%) within 30 min	✓	NA	✓	NA	286
g-C_3N_4	ZnO	CDots	Thermal polymerization and one-pot method	*S. aureus* and *E. coli*	1: 1×10^7 2: 200 μg mL^{-1}	300–800 nm	NA	99.97% and 99.99% against *S. aureus* and *E. coli*, respectively in visible light for 15 min	✓	✓	NA	NA	272
BiO_{2-x}	BiOBr	—	High temperature hydrothermal method	*S. aureus* and *E. coli*	1: 1×10^7 2: 20	Visible light	NA	100% against *S. aureus* and *E. coli* in 20 min	✓	NA	✓	NA	287
CeO_2	AgBr	—	Simple sedimentation-precipitation method	*E. coli ATCC 25922*	1: 4.7×10^7 2: 0.4 mg mL^{-1}	Visible light, ≥400	300 W	99.7% against *E. coli* in 180 min	✓	NA	✓	NA	288
g-C_3N_4	BiOCl	—	Hydrothermal method	*E. coli (BL21)*	1: 1×10^6 2: 0.4 mg mL^{-1}	Visible light	300 W	96.5% against *E. coli* in 40 min	✓	NA	✓	NA	289

p.s.: "—" represents that it is a PS–PS system, in which case the interface between two semiconductors serves as the electron mediator; "GI" stands for "greatly improved" compared to pure PS I or/and PS II, while "SI" means "slightly improved"; "#" represents a greatly enhanced production *vs.* pure PS I but reduced production in comparison to pure PS II as the blank control; and "✓" refers to be detected but not considering the PS II contribution.

and oxidation potentials, respectively. The direct Z-scheme heterostructure can overcome the drawbacks of reduced photo-generated charge redox ability during the transfer process because electrons with a low reducing capacity tend to be quenched by holes with low oxidizability, while the longer transmission distance of the Z scheme due to the charge loss during the migration restricts its further application.[291] To fill these gaps, Yu *et al.*[292] proposed a novel of step-scheme heterojunction called S-scheme heterojunctions. This new type of heterojunction system mainly consists of two n-type semiconductor photocatalysts, which are used as an oxidation photocatalyst (OP) and reduction photocatalyst (RP), respectively.[293,294] The internal electric field formed at the interface of the two photocatalysts provides the driving force to promote charge transfer, which is beneficial to reduce the transport distance of photogenerated carriers with the cooperative interface between the two components.[229,295] As illustrated in Fig. 22(A), the photogenerated electrons from the lower CB of the OP will combine with the photogenerated holes on the VB of the RP, while strong photogenerated electrons and holes are retained in the CB of the RP and the VB of the OP, respectively, which causes a strong redox potential for the subsequent photochemical reaction.[296,297]

Due to the tight interface contact, large surface area and efficient separation of photoinduced electron–hole pairs,[299] the S-type heterojunction exhibits favorable catalytic activity and retains powerful photogenerated carriers, making it suitable for photoactivated disinfection. Yu *et al.*[298] reported that 0D/2D S-scheme heterojunction-CeO_2 QDs and polymeric carbon nitride (CeO_2/PCN) exhibited strong photocatalytic inactivation efficiency. The accumulated h^+ at CeO as the oxidation site was involved in the creation of $^{\bullet}OH$, while the gathered e^- at PCN was involved in the production of $O_2^{\bullet-}$. The S-scheme material exhibited high photocatalytic efficiency of 88.1% towards *S. aureus* with visible light, compared with 32.2% and 10.7% for single CeO and PCN, respectively. However, because of the novel ideas and the difficulty of construction of matched band structures, to date, there are only a few reports on photocatalytic disinfection using S-scheme heterojunctions.

4.3.5 Dual heterojunction hybrids. The definition of dual heterojunctions remains ambiguous, where some claim that a heterojunction with two semiconductors components can be called a (direct) dual heterojunction, such as the direct PS–PS system[318] and InGaP/GaAs dual heterojunction.[319] However, the majority consider that only ternary heterojunction photocatalysts can be classed as dual heterojunctions.[320,321] The lifetime of surface photogenerated carriers in ternary systems can be effectively improved by electron transfer between interfaces.[322] The most common type of dual heterojunction belongs Z-scheme dual heterojunctions.[320,323] In the Z scheme ternary system (PS–A/D–PS), photoexcited charge transfer occurs through solid mediators located at the interface of PS–PS, which promotes the electron transfer and energy conversion. As shown in Fig. 23(A), Niu *et al.*[324] reported a novel g-C_3N_4/Ti_3C_2 MXene/BP ternary system with a Z-scheme constructed *via* CN, Ti_3C_2 MXene and BP and another P-bridging effect between the N atom (CN with nitrogen deficiency) and P atom (BP nanosheet). The electron transfer from CN to the BP nanosheets and the shifter transfer of electrons can be attributed to the introduction of highly conductive MXene solid mediators. It was confirmed that $O_2^{\bullet-}$ and $^1O_2$ were the two major ROS species through scavenger and ESR experiments, which were created by the reaction between the photogenerated e^- and dissolved O_2 in the CB of the BP nanosheets, and the interaction between the accumulated h^+ and dissolved O_2 in the VB of CN, respectively. Zhou *et al.*[325] synthesized a dual Z-scheme tandem heterojunction (WS_2 QDs/MoS_2@WO_{3-x}) (Fig. 23(B)) because of the abundant edge active sites created by 2D MoS_2 and better special separation and transfer of photo-produced charges due to the O dopants and tandem heterojunction formation, which exhibited favorable photocatalytic activity. Besides, a heterojunction is not necessary for two different components, it can also be formed by different facets of one semiconductor. The exposed [101] and [001] facets of anatase TiO_2 are good catalytic sites for n–p heterojunction formation.[326] There have been studies on n–p–n dual heterojunctions constructed by the [101] and [001] facets of anatase TiO_2 and metal sulfide,[327,328] in which the photoinduced electrons from TiO_2 transfer to the [101] surface of TiO_2 rather than MoS_2, while the photoinduced holes from TiO_2 migrate to MoS_2, resulting in a higher separation efficiency (Fig. 23(C)).

4.3.6 2D heterojunction hybrids

4.3.6.1 The interface between different dimension hybrids. As shown in (Fig. 30), the interfaces between different dimension materials are diverse. 0D materials refer to point contact, 1D materials refer to line contact, and their 2D counterparts refer to surface contact. As mentioned above, compared to their 0D and 1D counterparts, 2D layered materials show distinguished photoelectric and photocatalytic properties mainly due to their larger contact surface, and thus more superficial active sites and efficient interfacial charge transfer. Due to their atomic thickness (less than 5 nm), 2D nanomaterials show flexible grid structures. They can be rounded into 0D materials as nanoparticles, rolled into 1D materials as nanotubes and nanowires or stacked into 3D architectures (Fig. 24(b)).[329]

4.3.6.2 Different dimensional heterojunction hybrids

(1) 0D/2D heterojunction hybrids. Wu *et al.*[331] successfully deposited a RP/GO composite array on a Ti substrate for rapid bacterial inactivation under irradiation *via* photodynamic and photothermal synergistic effects. In this study, the bandgap of RP was only 0.85 eV, making the absorption of UV to NIR light possible. Besides, the introduction of GO greatly enhanced the photocatalysis efficiency of RP given that the photo-generated e^- of RP transfers to the CB edge of GO formed by its antibonding π^* orbital, which significantly reduces recombination. The *in vitro* inactivation assay showed that at a bacterial concentration of 10^7 CFU mL^{-1}, Ti-RP killed 78.68% of *S. aureus*, while the efficiency reached 98.28% after the deposition of GO. The most interesting thing was that NIR irradiation exhibited better inactivation than irradiation with visible light, as confirmed by the shorter illumination period. This phenomenon

Table 6 Typical 2D hybrid material-based composite photocatalysts and ROS generation from different NPs

Dimensionality	2D material-based composite	Methods	Bacteria and their concentration	Wavelength range	Inactivation efficiency	ROS	ROS radicals				Ref.
							$^{\bullet}OH$	$^{1}O_2$	$O_2^{\bullet-}$	H_2O_2	
0D/2D	Ag–ZnO nanoparticle/g-C_3N_4 nanosheet	One-pot hydrothermal process	*E. coli* 10^6 CFU mL^{-1}	Very low intensity UV light (2.2 W cm^{-2}, 20%)	100% under 3 h	Y	N	N	✓	NA	300
	Bi_2MoO_6/Ag nanoparticle/g-C_3N_4 nanosheet	Facile hydrothermal strategy	*E. coli* and *S. aureus*	500 W halogen lamp ($\lambda >$ 400 nm)	99.6% within 80 min under visible light	Y	✓	NA	✓	✓	301
	Vanadium–TiO_2 porous discrete/g-C_3N_4 nanosheet	Facile calcination and ultrasonic dispersion facilitated hydrothermal techniques	*E. coli* (G−) and *S. aureus* (G+) bacteria	Visible light (384–440 nm)	Efficiency over 99.5% for 60 min	Y	✓	NA	✓	✓	302
	Ag nanoparticle/g-C_3N_4 nanosheet	Hydrothermal as well as photo-assisted reduction	*S. aureus* 10^7 CFU mL^{-1}	500 W Xe lamp with 420 nm filter	Inactivation time: 180 min	Y	N	NA	✓	N	303
	Ag nanoparticle/g-C_3N_4 nanosheet	Microemulsion technique	*E. coli 1337-H* 8.9 × 10^9 CFU mL^{-1}	UV light with 385 nm and visible light with 515 nm	Inactivation time: 60 min	Y	✓	NA	N	N	304
	m-Bi_2O_4 nanoparticle/g-C_3N_4 nanosheet	One-pot hydrothermal method	*E. coli K-12* 10^6 CFU mL^{-1}	Xenon lamp (300 W) with UV light filter	Completely inactivate *E. coli* within 1.5 h	Y	✓	NA	✓	✓	270
	ZnO@stellerite nanoparticle/g-C_3N_4 nanosheet	Coupled hydro thermal-thermal polymerization process	*S. aureus* 10^7 CFU mL^{-1}	Visible light irradiation ($\lambda <$ 420 nm)	Nearly 90% disinfection rate for 2 h	Y	N	NA	✓	✓	305
1D/2D	PDA nanofibers/g-C_3N_4@Ag nanosheet	30 mg of g-C_3N_4 powder, 40 mg of HAD, 60 mg mL^{-1} $AgNO_3$ aqueous solution	*E. coli* $OD_{600} \approx 1$	Visible light	100% under 3 h	Y	N	✓	✓	NA	306
	TNA (titanium nanotube array)/g-C_3N_4 nanosheet	Electrochemical anodization	*E. coli*	500 W Xe lamp	Reached 100% for 60 min	Y	N	NA	✓	NA	307
	Au nanorods (NR)/TiO_2 nanobelts (NBs)	TiO_2 NBs were synthesized *via* a hydrothermal method, and then immersed in $HAuCl_4$/NaOH aqueous solution by a photoreduction method to obtain Au NR/TiO_2 NB	*E. coli*, ATCC 25922	Visible source: a 300 W Xe arc lamp with a cutoff filter ($\lambda <$ 400 nm) NIR light source: 250 W infrared lamp with a cutoff filter ($\lambda <$ 760 nm)	Reached 65% for 120 minutes with visible light; 49% for 120 min with NIR light	Y	✓	NA	✓	NA	308
	ZnO nanorod (NR)/RGO nanosheet	GO sheet was synthesized from graphite flake *via* a modified Hummers' method, then RGO–ZnO NR was synthesized *via* typical hydrothermal method	*E. coli* (MTCC-4296) and *S. aureus* (MTCC-3196)	Natural sunlight	Almost 100% towards *E. coli* and *S. aureus* for 60 min	Y	✓	NA	NA	NA	309
	TiO_2 nanotube arrays (TiNT)/g-C_3N_4 layer	One-step chemical vapor deposition (CVD) technique	*E. coli*	Visible light at 420 nm	~84% for 3 h	Y	✓	NA	NA	✓	310
	ZnO nanoflowers/V_2O_5 nanowires (NWs)	V_2O_5 NWs were synthesized by a hydrothermal method, and ZnO/V_2O_5 NW_S were prepared *via* one-pot method	*S. aureus* (ATCC25923) 10^6 CFU mL^{-1}	Stimulated sunlight (300–2500 nm) with xenon lamp	99.8% for 12 h	Y	NA	NA	NA	NA	311

Table 6 (*continued*)

Dimensionality	2D material-based composite	Methods	Bacteria and their concentration	Wavelength range	Inactivation efficiency	ROS	ROS radicals				Ref.
							$^{\bullet}OH$	$^{1}O_2$	$O_2^{\bullet-}$	H_2O_2	
2D/2D	g-C_3N_4 nanosheet/red P hybrid nanosheets	Ultrasonic-assisted wet chemical method	*E. coli* 10^7 CFU mL^{-1}	300 W Xe lamp	Inactivation time: 120 min	Y	N	NA	✓	✓	312
	$Mg_{1.2}Ti_{1.8}O_5$ (mT) nanoflakes/g-C_3N_4 (CN) nanosheets	Sol–gel method and ionothermal method, respectively	*E. coli* 5×10^7 CFU mL^{-1}	300 W Xe lamp with an Am1.5 filter	Total *E. coli* was eliminated by mT/CN within 100 min	Y	✓	NA	✓	NA	285
	RGO nanosheets/g-C_3N_4 (CN) sheets	Modified heat-etching method	*E. coli K-12* 2×10^6 CFU mL^{-1}	300 W Xe lamp with UV light filter	4 h of VL irradiation	Y	✓	NA	✓	✓	283
	WO_3–metal nanoporous sheet/g-C_3N_4 nanosheet (metal = Cu, Ag, Au)	g-C_3N_4 nanosheets were deposited on WO_3–metal nanoporous sheet by electrochemical method	NA	White light source	Inactivation time: 120 min	Y	✓	NA	✓	✓	313
	Bi_2MoO_6(BM) nanoplates/g-C_3N_4 sheets (CNN)	*In situ* solvothermal method	*E. coli* 2.5×10^7 CFU mL^{-1}	300 W Xe lamp equipped with a UV cutoff filter ($\lambda <$ 420 nm)	99.99% within 4 h for 10%, 30%, 40%-BM/CNN; 99.99% within 2.5 h for 10%, 30%, 40%-BM/CNN	Y	✓	NA	✓	NA	314
	PEG-MoS_2/rGO-streptomycin sulfate (SS) nanoflakes	Traditional hydrothermal method was used to fabricate tPEG–MoS_2/rGO nanoflowers, the as-prepared nanoflowers of PEG–MoS_2/rGO were exfoliated into nanoflakes	*E. coli* and *S. aureus* 10^8 CFU mL^{-1}	NIR, 808 nm, 2.0 W cm^{-2}	Beyond 90% within 4 h for PEG–MoS_2/rGO–SS towards *E. coli* and *S. aureus*	Y	✓	NA	✓	✓	315
	BiOI/BiOBr nanoflakes/g-C_3N_4 nanosheets	g-C_3N_4 was synthesized by the thermal polycondensation of urea, the pure BiOBr, BiOI and g-C_3N_4/BiOI/BiOBr composite were prepared by chemical precipitation	*E. coli* ATCC 15597 10^9 CFU mL^{-1}	300 W xenon lamp with a UV cutoff filter ($\lambda <$ 400 nm)	Almost all *E. coli* cells were killed for 3 h	Y	✓	NA	✓	NA	316
	TiO_2–Bi_2WO_6 binanosheet	Two-step hydrothermal method	*E. coli* 10^9 CFU mL^{-1}	300 W xenon lamp with a UV cutoff ($\lambda <$ 420 nm)	The count of bacteria remained 10° with 40% TBWO (100 μg mL^{-1}) for 4 h	Y	✓	NA	✓	NA	317

"Y" indicates total ROS ($^{\bullet}OH$, $O_2^{\bullet-}$, $^{1}O_2$, H_2O_2, h^+, and e^-) were detected, "N" indicates no significant ROS were detected, "✓" indicates the corresponding type of ROS was detected, and NA means "not available" or not provided in the literature.

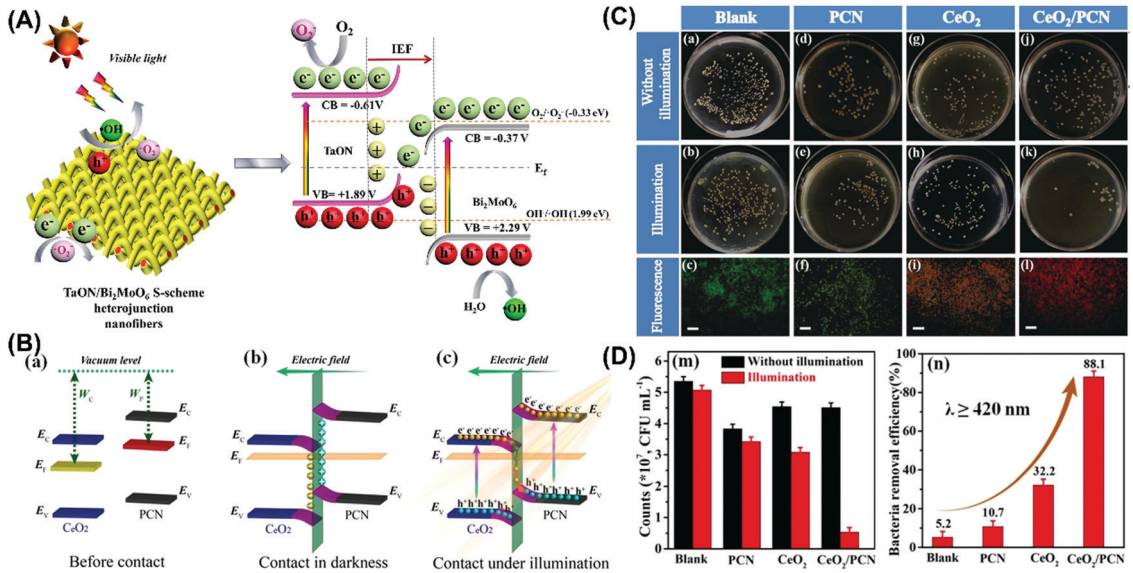

Fig. 22 Photogenerated electron transfer and photocatalytic inactivation of S-scheme heterojunctions. (A) Photogenerated electron transport mechanism of S-scheme heterostructure (TaON/Bi_2MoO_6 as an example). (B) Electron transfer and photocatalytic inactivation effects and numerical calculation of CeO_2/PCN with different conditions. (A) Reprinted from ref. 297. (B)–(D) Reprinted from ref. 298.

was attributed to the photothermal effect of RP under NIR irradiation, where the heat would inhibit the reactivity of proteins and the metabolism of bacteria, promoting the rupture of their cell membrane by ROS. Besides, it was reported that RP/GO hybrid composites also exhibited inactivation under common LED light irradiation and biofilm clearance, which broaden their practical application.

(2) 1D/2D heterojunction hybrids. Dissimilar dimensional photocatalysts show unique properties owing to their diverse electron performances in disparate confined dimensions.[332] Vertically aligned 1D nanostructures, including nanowires, nanotubes, nanorods, and nanofibers,[99] display various merits as photocatalysts because of their large aspect-ratio and aligned pathway for direct electron and optical exciton transmission.[333]

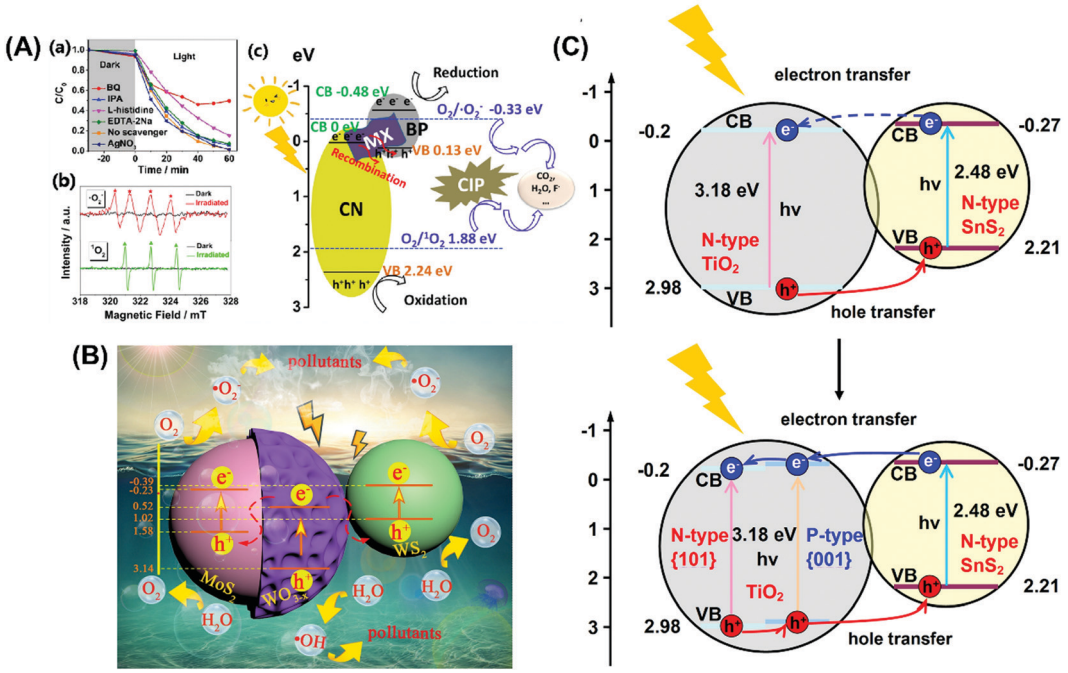

Fig. 23 Band structure and electron transfer of dual heterojunctions. (A) (a) and (b) Detection of photogenerated ROS species in g-C_3N_4/Ti_3C_2 MXene/BPs. (c) Band structure and redox reactions with visible light. (B) Band structure and ROS generation in WS_2 QD/MoS_2@WO_{3-x} core–shell dual Z-scheme tandem heterojunctions. (C) Creation of n–p–n heterojunctions with the (101) and (001) facets of anatase TiO_2 and SnS_2. (A) Reprinted from ref. 324. (B) Reprinted from ref. 325. (C) Reprinted from ref. 328.

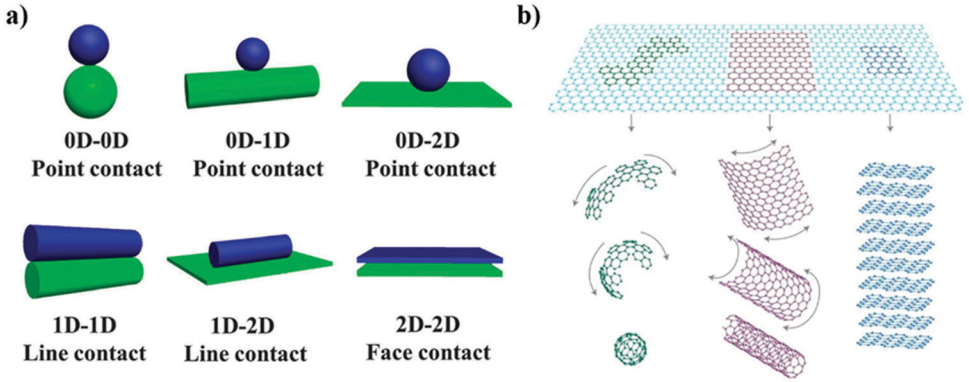

Fig. 24 (a) Scheme of the specific contact interface of 0D/0D, 0D/1D, 0D/2D, 1D/1D, 1D/2D and 2D/2D nanomaterials. Reprinted from ref. 330. (b) 2D graphene nanosheets can be circled to balls (0D material), rolled into tubes (1D material) or folded into 3D graphite. Reprinted from ref. 329.

The two materials in heterostructures can be tightly combined with opposite surface charges, leading to sufficient interfacial contact in the heterostructures.[334] Therefore, the architecture of 1D/2D heterostructure hybrids can combine the advantages of two materials and overcome the drawbacks of the single units.[332,335]

In the last five years, research on 1D/2D heterostructure hybrids has become a hot topic and many 1D/2D materials have appeared, such as 1D CdS nanowires/2D $BiVO_4$ nanosheets,[332] 1D Nb_2O_5 nanorods/2D g-C_3N_4 nanosheets,[336] 1D TiO_2 nanofibers/2D MoS_2 nanosheets,[337] 1D WO_{3-x} nanowires/g-C_3N_4 nanosheets,[338] 1D$NiCo_2S_4$ nanowires and 2D layered-δ MnO_2.[339]

(3) 2D/2D heterojunction hybrids. As mentioned above, 2D semiconductors are promising photocatalysts due to their great properties.[340] Thus, it can be predicted that 2D/2D heterojunction hybrids may have better photocatalysis efficiency. Cheng *et al.*[341] developed 2D/2D heterojunction photocatalysts by coupling g-C3N4 (CN) nanosheets with oxygen vacancies confined in Bi20TiO32 (BTO) mesoporous nanosheets with exposed (001) facets *via* a facile hydrothermal process with the assistance of post-treatment.

Besides, the majority of the developed photocatalytic materials are at least one metal-based or metal-containing composites. However, these photocatalysts would release toxic metal ions, which pose a great threat to human health. Therefore, 2D/2D heterojunction hybrids for bacterial inactivation are in great demand. Zhang *et al.*,[342] for the first time, fabricated a metal-free BP/g-C_3N_4 2D/2D heterojunction for visible light-driven water disinfection. In the *in vitro* antibacterial assay, BP/g-C_3N_4 exhibited around a seven-times inactivation efficiency comparing to bare g-C_3N_4 given that the photogenerated e^- could transfer from g-C_3N_4 to BP, which greatly enhanced the charge carrier separation.

4.4 Dye-sensitized hybrid semiconductors

4.4.1 The basic principle of dye-sensitized hybrid semiconductors. Dye-sensitization, which was first proposed by Grätzel *et al.*[343] as a satisfying strategy to improve the activity of dye-sensitized solar cells (DSSCs), has been widely used to improve the photo-quantum efficiency and broaden the photo-absorption response of photocatalysts.[344] The use of dye-sensitizers has matured considerably in photocatalytic applications such as photodynamic antimicrobial chemotherapy (PACT).[345,346] PACT relies on the generation of ROS in the presence of photosensitizer (PS) molecules under illumination. The PS tends to be NIR absorbing dyes, such as phthalocyanines,[347] porphyrins,[348,349] and porphins,[350] which are beneficial to reduce the interference of self-absorption and spontaneous fluorescence of tissue, and enhance the tissue penetration depth under illumination.[346] Nevertheless, PSs suffer from weak hydrophilicity, strong aggregation, high doses, and low biocompatibility.[351,352] It seems a feasible scheme to address these issues by using materials as suitable conjugates for PSs as delivery systems against microorganisms. For example, combination of dye and semiconductor (dye-sensitized semiconductors) has become an effective modification strategy for both dyes and semiconductors as photocatalysts, which effectively absorb visible or even NIR light, where efficient semiconductor stimulation can be an alternative approach of great use.[353] As illustrated in Fig. 25, in a typical dye-sensitized photocatalyst, the CB value of the semiconductor is lower than the dye LUMO value, while higher than its HOMO,[343,354] in

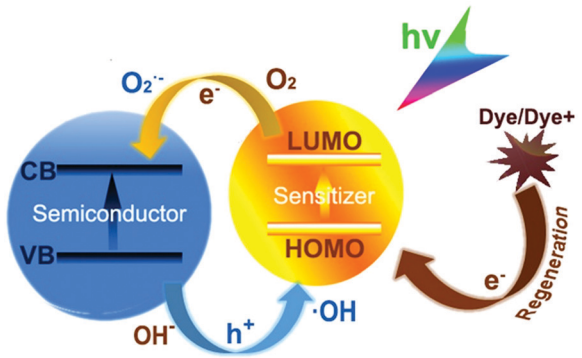

Fig. 25 Mechanism of the photocatalytic reaction on a dye-sensitized hybrid semiconductor.

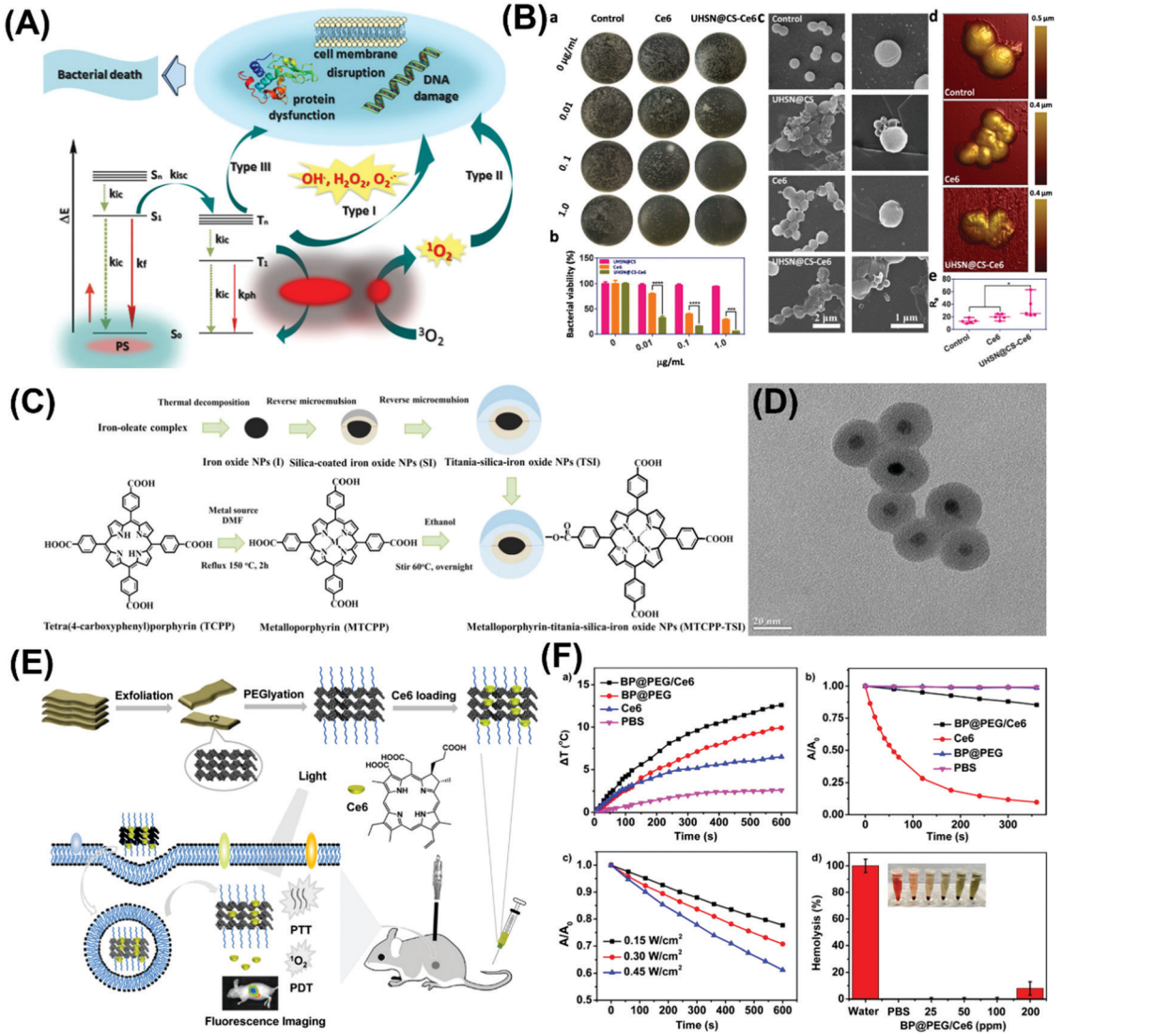

Fig. 26 Photoinduced bacterial disinfection for dye-sensitized semiconductors. (A) Mechanism of photodynamic antibacterial therapy. Reprinted from ref. 379. (B) Photodynamic antibacterial effect of Ce6 modified with hollow SiO_2/chitosan. Reprinted from ref. 380. (C) Synthesis of FeO_x–SiO_2–TiO_2–metalloporphyrins and (D) their TEM images. (C) and (D) Reprinted from ref. 371. (E) Schematic illustration of the synthesis of BP@PEG/Ce6. (F) Photothermal evaluation and cytocompatibility (hemolysis test) of the as-prepared NPs in (E). (E) and (F) Reprinted from ref. 377.

which the dye serves as an antenna, enabling visible light to be received and resulting in the follow-up behaviors of photo-induced reactions *via* the injection of electrons into the CB of the semiconductor.[355] This procedure is principally follows two steps: (1) the photogenerated electrons of the illuminated dye molecules transfer from the HOMO to the LUMO and (2) the transfer of electrons from the LUMO of the dye to the CB of the semiconductor. As reported by Zhang,[356] besides the dye and semiconductor, the co-catalyst and sacrificial electron donor used for dye recycle also play dominant roles in photoactivity. Currently, noble metal-based (Pt, Ru, Rh, and Pd)[357–361] and noble-metal-free[362–365] co-catalysts have been comprehensively investigated to extract photogenerated carriers. Also, research has revealed that the electron donor species[366–368] can influence the oxidation half reaction,[369,370] which prominently impacts the overall photoactivity of dye-sensitized semiconductors.

4.4.2 Antibacterial activity of dye-sensitized hybrid semiconductors. Dyes as photosensitizers can trigger photodynamic antibacterial behaviors (Fig. 26(A and B)), making them potential antibacterial materials acting on deeper issues in response to NIR light. In the dye-sensitized semiconductor system, dyes are loaded into semiconductors (as a drug delivery platform) *via* physical encapsulation, adsorption or chemical coupling, which further improves the drug delivery efficiency and avoids the inherent drawbacks of dyes (such as poor water solubility). TiO_2 with a wide band gap has been functionalized by dye sensitization in recent years. For example, Insin *et al.*[371] prepared FeO_x–SiO_2–TiO_2–metalloporphyrin compounds with a wide light response (Fig. 26(C)), good dispersion in solution and high photoactivation effects. Giridhar *et al.*[372] evaluated *p*-methyl red, an azobenzene compound, for the photocatalytic enhancement of TiO_2, which could serve as photo switches

when attached to TiO_2, rendering the system photo responsive to external illumination. Besides, research on manipulating the surface of titanium natural dyes with biological safety and economic advantages has been well investigated to sensitize TiO_2.[373] Xing's team proved that three natural dyes (including alizarin red, fuchsin acid, and alizarin) as modified sensitizers of anatase could efficiently extend its optical absorption edge, and therefore increase its antimicrobial efficiency.[374] For other semiconductors, anthocyanin (a type of natural molecule)-sensitized ZnO proved to increase the bacterial loss by ~10% compared to naked ZnO nanoparticles under solar simulator light.[375] It was proven that the 2D material g-C_3N_4 nanosheets sensitized with Cu diphenylamine complexes were accessible to eliminate pathogens, in which the layered structure with delocalized π-electrons of Cu–biphenylamine complexes serves well in the charge transfer process of photocatalysis.[376] Moreover, some dyes possess favorable optothermal effects, and thus dye-sensitized systems can be used for bacterial inactivation with synergetic photothermal and photocatalytic therapy.[377] Photogenerated ROS remains a principal antibacterial mechanism of dye-sensitized semiconductors, causing cell membrane rupture, and therefore intracellular DNA and protein leakage.[178,179] The photogenerated ROS processes can be depicted in eqn (21)–(28) below:[378]

$$\text{Dye} + \text{semiconductor} \rightarrow \text{dye–semiconductor} \quad (21)$$

$$\textit{trans}\ \text{dye–semiconductor} \rightarrow \textit{cis}\ \text{dye}^*\text{–semiconductor} \quad (22)$$

$$\textit{cis}\ \text{dye}^*\text{–semiconductor} \rightarrow \text{semiconductor} + \text{decomposed dye} \quad (23)$$

$$\text{Dye} + \text{semiconductor} + O_2 \rightarrow \text{semiconductor} + \text{decomposed dye} + O_2^{-} \quad (24)$$

$$O_2^{\bullet -} + H^+ \rightarrow HO_2 \quad (25)$$

$$HO_2^{\bullet} + H^+ + e(\text{CB–}TiO_2) \rightarrow H_2O_2 \quad (26)$$

$$2O_2^{\bullet -} + 2H^+ \rightarrow 2OH^{\bullet} + O_2 \quad (27)$$

$$OH^{\bullet} + \text{cell} \rightarrow \text{damaged cell} \quad (28)$$

4.4.3 Common types of dye-sensitizer hybrids and their photocatalytic inactivation application. Research on manipulating the surface of photocatalysts with highly active, safe and inexpensive dyes has become a critical hotspot in photocatalytic disinfection recently.[344] According to the current research, dye sensitizers principally include natural organic dyes such as chlorophyll,[381,382] cytochrome *c*,[383,384] anthocyanin,[375,385] and alizarin red,[386,387] as well as artificial composite dyes, such as porphyrin compounds,[388,389] phthalocyanine compounds[390] and polypyridyl complexes.[391–393]

4.4.3.1 Photocatalytic mechanism of porphyrin-based functional nano-systems for bacterial inactivation. As the photosynthesis reaction center of green plants, porphyrin with a planar π-conjugated aromatic macrocycle[394] benefits the enhancement of electron coupling and transfer of photogenerated carriers.[395] Owing to its wide visible light absorption range (400–800 nm),[396] porphyrin is frequently applied as a photon-trapping antenna molecule and co-catalyst in photocatalytic models.[397] It has been reported that self-assembled molecular aggregates are candidate models for energy transfer processes,[398] which resemble the photon-collected congeries in photosynthetic bacteria.[399] Porphyrins naturally self-assemble into aggregates of π-conjugated molecules due to their easily modified porphyrin ring,[400] and thus there are numerous porphyrin derivatives. For example, Wang's team[401] synthesized supra-amphiphiles by combining a heteroditopic porphyrin amphiphile with zinc, which could be further used in controllable self-assembly applications. According to the report of Wang *et al.*,[402] porphyrin J-aggregates could be self-assembled by two porphyrins with opposite ionic charges. In the case of porphyrin-sensitized semiconductors, Ghosh *et al.*[403] well investigated the photoelectron-transfer mechanism in porphyrin aggregates, and observed an enhancement in charge carrier separation at the porphyrin/TiO_2 interface (Fig. 27). According to Sorgues,[404] the zinc tetracationic porphyrin $[ZnTmePyP]^{(4+)}$ was successfully synthesized through electrostatic complexation of porphyrin and polyoxometalates (POm), and later the occurrence of electron jump from the porphyrin to the POm was observed in the presence of visible light.

Furthermore, some porphyrin derivatives have been applied for photodynamic therapy (PDT). He *et al.*[405] chose the second-generation photosensitizer hematoporphyrin monomethyl ether (HmmE) to sensitize TiO_2 nanocomposites owing to its good photodynamic effects, low toxicity in the dark and fast removal rate.[406] Also, the HmmE–TiO_2 NCs showed strong ROS generation capability and inactivation effect of KB cells (type of cancer cells). Besides, 5,10,5,20-tetraphenyl-21*H*,23*H*-porphine nickel (TPPN) was applied to doped titanium dioxide *via* the sol–gel method. The TiO_2/TPPN thin film was employed for the disinfection of the plant pathogen *E. carotovora* subsp. with a visible spectrum response, which showed over 90% bacteriostasis rate with white light (>400 nm) illumination for 60 min.[406] As illustrated in Fig. 28(A), the synthesis of a 2D nanostructure diporphyrin honeycomb membrane consisting of TiO_2, protoporphyrin IX, and hemin (TiO_2/PPIX/Hem) was reported *via* dehumidifying with bidentate binding.[407] The generation of an anodic photocurrent was observed on the surface of the PS/TiO_2/PPIX/FTO electrode through electron transfer processes (Fig. 28(B)), and therefore proved its high photoactivity. Due to its inactivation effect, it showed the highest inhibition of *Bacillus subtilis* cultured with TiO_2/PPIX/Hem under visible light compared with TiO_2/PPIX and naked TiO_2. Also, the TiO_2/PPIX/Hem group further exhibited a much more rapid bacterial clearance rate in bactericidal kinetics characteristics. Furthermore, Wang *et al.* used water-soluble porphyrin–tetra sulphonatophenyl porphyrin (TSPP)–TiO_2 nanowhiskers for the early diagnosis of inflammation together with bio-imaging and treatments of microbial infections.[408–413]

4.4.3.2 Photocatalytic mechanism of polypyridine-based functional nano-systems for bacterial inactivation. Polypyridine

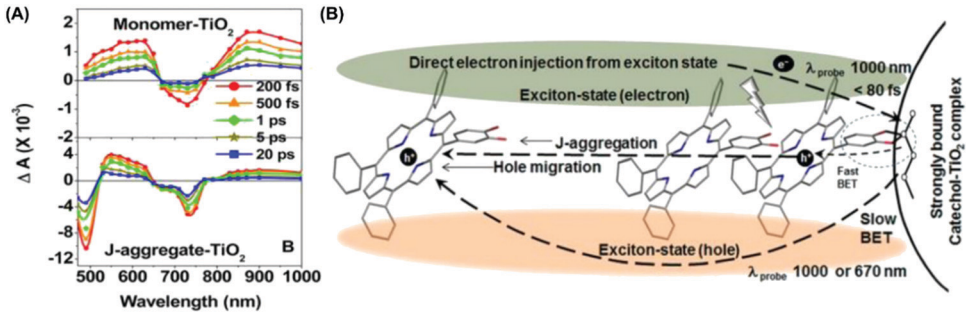

Fig. 27 (A) Distinction of absorption spectra between monomer- and J-aggregated porphyrin–TiO_2 NP_S with different delay times. (B) Mechanism of charge-carrier shift in the J-aggregate porphyrin–TiO_2 system. Reprinted from ref. 403.

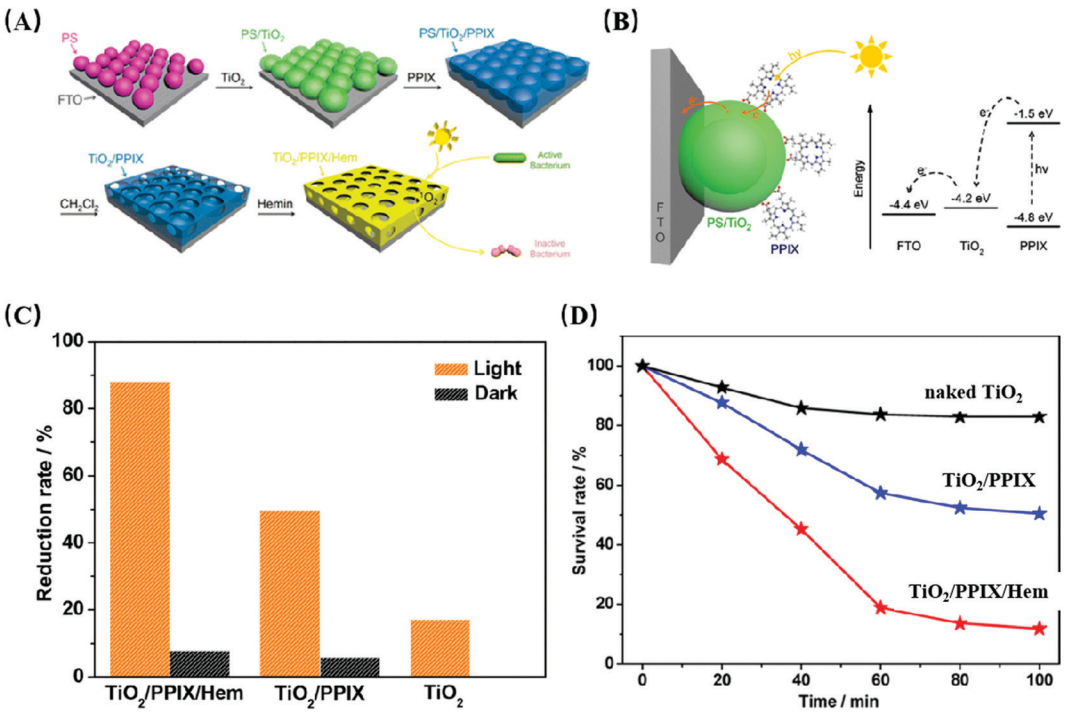

Fig. 28 (A) Schematic illustration of the synthesis of the TiO_2/PPIX/Hem composite membrane. (B) Electron jump mechanism of the PS/TiO_2/PPIX/FTO rheophore system under visible light. (C) Antibacterial activity toward *Bacillus subtilis* with or without illumination for 100 min. (D) Bactericidal kinetics of different materials in the presence of light for 100 min. Reprinted from ref. 407.

generally exists in the form of transition metal-containing polypyridine derivatives.[414–420] Adamso *et al.* first reported that the excited bipyridyl ruthenium *Ru $(bipy)_3^{2+}$ can be used as a sensitizer and e^- transfer reductant in 1972,[421] realizing the hopeful perspective of polypyridine derivatives as dye sensitizers. Thus far, the inorganic chromophores Ru(II) polypyridyl complexes have been comprehensively applied for photocatalytic applications, which is attributed to the favorable photoelectric and photochemical properties, including high molar absorptivity in the visible spectrum, thermal stability, and excited-state reactivity.[414,422] In a metal-centered system, photon absorption gives rise to the generation of metal-to-ligand charge-transfer (MLCT) excited states, including singlet or triplet multiplicity.[422,423] The redox potentials of these photoexcited MLCT states are high enough for them to act as energy donors, electron donors, or electron acceptors when reacting with other solute molecules.[422] Therefore, these systems may be subjected to the photo-accumulation of charges *via* the continuous absorption behaviors of single photons.[424,425] In the case of other transition metals, Bernhard proposed six heterogeneous iridium compounds as highly efficient photosensitizers *via* photo-physical measurements and quenching and electrochemical studies.[426] According to the report of Liang *et al.*,[427] porous polymers modified with rhenium-metalated polypyridine were fabricated *via* a simple oxidative coupling method. They displayed an enhanced photoactive performance and photothermal stability, which highlights the prospective of polypyridine complexes serving as photocatalysts *via* synergistic catalysis. Based on preliminary research, photosensitizers play a dual role in photocatalysis-initiating reactions and controlling

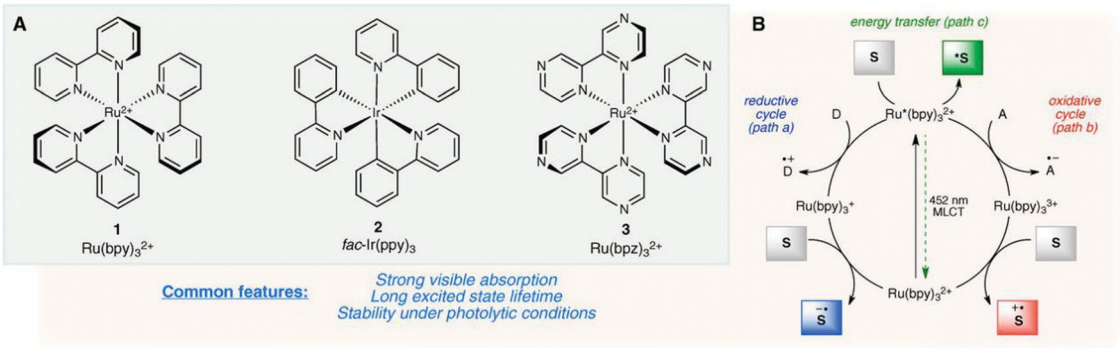

Fig. 29 (A) Structures of Ru(II) and Ir(III) polypyridyl complexes used as photosensitizers in photo-catalyst systems. (B) Photoinduced $Ru^*(bpy)_3^{2+}$ used as electros mediators, receiving or donating electrons. Reprinted from ref. 429.

stereoselectivity *via* an electron or energy transfer process (Fig. 29).[428]

Some polypyridine complexes are promising antibacterial candidates. Polypyridyl ligands have been identified to be lipophilic in nature, which endows polypyridyl good biocompatibility owing to the easy access and interaction between the materials and the cell lipopolysaccharide layer (LPS).[430] It was illustrated that the intercalation in biochemistry is a process that can be extensively used to explain the mechanisms of the inactivation of cells for some drugs,[391] and the heterocyclic polypyridyl group of molecules has been proven to be typical intercalators.[431,432] According to Zhang *et al.*, the electron-acceptor group and large hydrophobic group in the intercalative ligand are beneficial for the combination of ruthenium compounds with DNA.[433] The biological application of Ru(II) polypyridyl compounds is increasing due to the awareness of the good bioactive properties of ruthenium for the inactivation of cancer, microorganisms, and even viruses.[434,435] For example, a titanium alloy coated with a ruthenium complex exhibited hopeful antibacterial and antifungal activity and low cytotoxicity to mammalian cells, representing that ruthenium complexes are broad-spectrum antibacterial materials.[434] Matshwele's team[391] synthesized Ru(II)/(III) complexes as antibacterial agents, which exhibited high inactivation capability towards non-drug-resistant bacterial species such as *S. aureus* and *K. pneumoniae*, and even their drug-resistant strains such as MRSA and MDR *K. pneumoniae*. The bacterial DNA was completely denatured, as shown by the characterization of DNA gel electrophoresis, indicating the strong affinity of Ru(II)/(III) complexes towards DNA, and further inducing DNA cleavage by intercalation. According to Nambagari,[392] three new cobalt(III) polypyridyl complexes were successfully proven to possess antibacterial properties. Our team proved that a ferrocene-substituted carborane ruthenium(II)–arene complex (FcRuSB) can be utilized as an inducer to effectively reverse the drug resistance of pathogens.[436] Yi *et al.*[393] also confirmed that three iridium(III) polypyridyl compounds are promising antibacterial candidates.

4.4.3.3 Natural organic dye hybrids for bacterial inactivation

(1) Chlorophyll. Naturally occurring pigments (such as chlorophyll, cytochrome, and vitamin B12) play crucial roles in various life processes and are referred as the "pigments of life".[437] Chlorophyll, belonging to the class of porphyrin macrocycle derivatives, has been extensively employed as a photosensitizer in light-harvesting systems, which is because porphyrin-based compounds with 18π-electron conjugated macrocycles possess distinguished catalytic, photochemical and photophysical properties.[438,439] These materials are expected to strongly absorb in the visible and even NIR region as efficient photocatalysts.[440] Bevilacqua *et al.*[381] analyzed the absorption spectra of chlorophyll enabled in the near UV and visible light range. Moreover, pheophytin (Pheo-) a and b (with no Mg(II) ion) displayed a slight red-shift compared with the integrated chlorophyll.

Chlorin derivatives, including chlorophylls as Mg-containing chlorins, are presently investigated for antimicrobial PDT to inactivate some important microbial pathogens.[441] For example, Ferro's team[442] proved the strong inactivation activity of liposome-delivered chlorophyll a towards *S. aureus* (MRSA), which was more pronounced with selective targeting using liposome as carriers. Kustov *et al.*[443] successfully synthesized water-soluble chlorophyll pigments as novel potential photosensitizers to deal with bacteria and fungi. They indicated that chlorophyll with a positive charge (such as $N(CH_3)_3^+$ groups) could treat wound infections and bacterial biofilms. Similarly, another positively charged chlorophyll derivative, lysine–chlorin E6(pL–c_{e6}) conjugates, are effective against pathogens in the oral cavity, while oral epithelial cells can be well preserved.[441] Particularly, some naturally antibacterial materials such as antimicrobial peptides all have a pronounced polycationic charge, which plays an important role in binding with negatively charged bacteria due to electrostatic attraction.[444,445]

(2) Cytochrome c. Cytochrome *c* (Cyt *c*) is a hemeprotein intensely combined with the inner mitochondria membrane by electrostatic interactions. It serves as a vital electron transporter in the respiratory chain.[446,447] Wang *et al.*[448] firstly reported that Cyt *c* could be used as a carrier of porphyrin-based photosensitizers to improve their photoinactivation efficiency against the Gram-negative bacteria *E. coli*. It was shown that the positively charged porphyrin Cyt *c* was on the surfaces of bacteria *via* TEM measurement and fluorescence confocal microscopy.

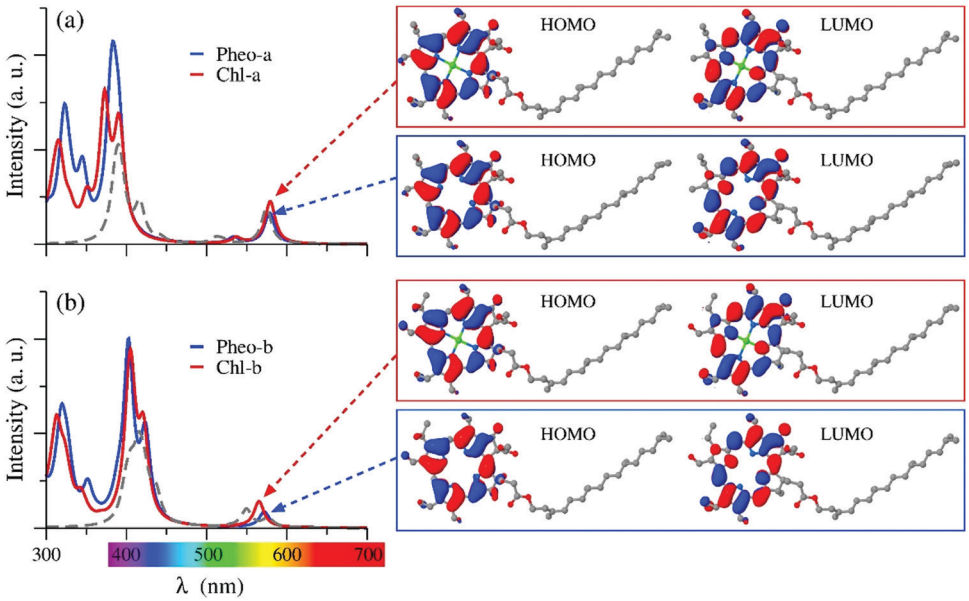

Fig. 30 Absorption spectra of Chl-a and Pheo-a systems (a) and Chl-b a Pheo-b systems (b). Reprinted from ref. 381.

Also, the ζ potential analysis clearly demonstrated that porphyrin Cyt *c* and *E. coli* were efficiently integrated *via* electrostatic interactions.

(3) Rubiadin. Rubiadin, also named alizarin, is a typical medium dye extracted from the root of Rubiaceae.[449] Rubiadin has exhibited strong inhibition towards a wide range of bacteria, especially to *Staphylococcus aureus* in recent studies.[450,451] The photogenic superoxide anion ($O_2^{\bullet-}$) and singlet molecular oxygen ($^1O_2$) have been shown to be principle mechanisms of this dye for bacterial inactivation, revealing its potential as a drug for photodynamic antimicrobial chemotherapy.[452] It was reported that Alizarin Red S sensitization of TiO_2 broadened its light absorption range and improved the photo-quantum efficiency, and therefore enhanced the antimicrobial activity of TiO_2.[373] Rubiadin also exhibited low toxicity in mice *via* acute toxicity trials,[451] which reflects the good biocompatibility of this dye for further medical applications. For example, rubiadin derivatives have been applied as a biological dressing for improving the protection and preventing bacterial infection of skin.[453]

(4) Anthocyanin. Anthocyanins are naturally occurring polyphenols[454] that contribute to the high antioxidant activity in some plants.[455] They are well known due to their low cost, hydrophilia owing to their hydroxyl groups (•OH), and biosafety as sensitized dyes.[385,456,457] Hilal *et al.*[375] observed that anthocyanin-sensitized ZnO nanoparticles increased the loss of *E. coli* by 10% compared to naked ZnO under the same light conditions. It was shown that the photoinactivation process resulted in the mineralization of the bacterial membrane and intracellular organic components, which leaked after cell rupture. Moreover, the compounds from the photodegradation of anthocyanin were confirmed to be mineral and innoxious, revealing its potential as a sensitized dye. Tu's team[458] invented a smart calcium alginate fiber modified by anthocyanin dyed–hydroxypropyl trimethyl ammonium chloride chitosan (HACC). It was shown that the modification of anthocyanin dyed–HACC had strengthened the dyeing and antibacterial activity of calcium alginate fiber, which is a potential candidate for wound healing.

4.4.4 Application limitation and prospect of dye-sensitized semiconductors. In the photoinduced process, the dye is always inevitably degraded by oxidation, resulting in a limited number of cycles of the materials. Although porphyrin and polypyridine-based semiconductors have been widely used due to their good photosensitization activity, consideration should be given to the biotoxicity of metal-based dyes, which may degrade to harmful substances in solution under photochemical conditions, and thus each dye should be considered for its form of existence after degradation. In addition, synthetic dyes should be observed for incidental effects and adverse drug interactions.[459] Thus, it seems that natural pigments are more attractive. The inherent drawbacks of dyes, for example, poor photon/thermal stability, poor water solubility, and low affinity for bacteria hinder their further applications.[460,461] Some claim more specific requirements, including simplified and cheap synthetic procedures, acceptable stability, preferential binding or absorption by target cells or tissues, and low side effects. Thus, the strategy of functional encapsulation or modification of dye-sensitized semiconductors as a nanocarrier and delivery platform has been employed to improve their physicochemical properties, material utilization, and selectivity of target bacteria.

5. Conclusion and prospects

In this review, we comprehensively discussed the research status of the modification strategies of photocatalytic semiconductors for bacterial inactivation, including band structure

analysis, synthetic techniques, mechanism of photogenerated charge separation and reactive sites, ROS-induced antibacterial mechanism, and biosafety issues for further medical applications. Although the photo-induced antibacterial strategy has attracted extensive attention, research on the design and application of photoactive hybrid semiconductors for bacterial inactivation remains in its infancy, and thus further developments are evidently required. Some challenges should be considered before further large-scale applications.

5.1 Limitations and challenges

(1) In current research, more semiconductor hybrids depend on visible-light-driven energy with limited light penetration depth, which only suits for bacteria disinfection in the environment or superficial wounds, but not deep tissue infections such as organs inflammations.[462]

(2) *E. coli* or *S. aureus* are used as the model bacteria in most reports. However, different bacteria possess distinct physiological structures and death mechanisms, and thus it is required to explore the distinctions of the interactions between photocatalytic semiconductors and different bacteria. Besides, the existing photocatalytic semiconductors can deal with bacteria due to their broad-spectrum antibacterial properties, but they have no selectivity for bacteria and cannot achieve specific selection and treatment of target bacteria.

(3) The photocatalytic antibacterial activity is affected by various factors such as material morphology, synthesis technique, dosage, irradiation intensity and time, and the reaction environment such as pH and solute species. At present, it is difficult to compare two different modification strategies because an operational evaluation standard has not been developed for photocatalysis. In addition, the actual application environment of photocatalysis is more complicated. For example, it is inclined to hypoxia and low pH in bacterial infections.[463] The affinity of photocatalytic materials and bacteria, antibacterial activity and stability of photocatalytic semiconductors in a specific microenvironment remains unclear.

(4) Although photo-induced ROS generation has become a hopeful route to kill antibiotic-resistant bacteria and biofilm rapidly and effectively, the photo-sensitive performance of antibacterial properties occurs only in the presence of light. Furthermore, long-time light exposure may cause phototoxicity and even tissue hypoxia, which largely restrict the clinical application of photoactive semiconductors.

(5) At present, most photocatalytic semiconductors are still in the laboratory stage, and many problems remain for further commercial industrial applications, such as simplified synthesis routes suitable for large-scale production and long-term assessment of product environmental impacts.

5.2 Future prospects

(1) A more comprehensive and in-depth investigation of the photo-induced antibacterial mechanisms of semiconductor hybrids is crucial for their further optimization and enhancement of their photocatalytic performance, which is beneficial for the design and development of photocatalytic antibacterial semiconductors. The mechanism of the interaction between photocatalytic semiconductors and bacteria, including photo-induced ROS antibacterial behaviors and the interface reactions between both need to be further revealed and understood. Advanced *in situ* characterization technology and theoretical calculations may facilitate the exploration of the relevant mechanisms, which may significantly deepen our understanding on the photocatalytic antibacterial process.

(2) For the further practical use of photocatalytic semiconductors for antibacterial applications, researchers have designed and developed some photocatalytic reactors[464] with the aim of the expansion from the laboratory-scale process to commercially/industrially feasible applications and promotion of the recovery and reuse of photocatalysts. These reactors are also beneficial to enhance ROS generation and storage, which may solve the contradiction between high efficiency and long-acting inactivation.

(3) Synergistic antibacterial strategies should be considered in further applications. With the use of two or more inactivation mechanisms, synergistic antibacterial strategies exhibit enhanced antibacterial effects, and meanwhile avoid the cell cytotoxicity and drug resistance caused by the excessive use of a single ingredient. For example, photocatalysis and physical contact effects, in which the sharp edges of semiconductors can stab bacteria.[465] Photocatalysis and photothermal effects,[466] in which photon energy can be converted into heat to cause photothermal ablation of bacteria. Photocatalysis and the release of metal ions, in which the release behaviors of copper ions is beneficial to kill bacteria.[248] Besides, magnetic photocatalytic materials such as Fe_3O_4 can utilize magnetism to improve the separation and recovery of the material and even achieve magnetic targeting to bacterial infections.[467]

(4) Functional surface modifications of photocatalytic semiconductors can further improve their effects. For example, photocatalytic semiconductors such as dye-sensitized semiconductors possess relatively poor hydrophilicity, which can be improved by introducing O-containing functional groups, such as hydroxyl (–OH) and carboxyl (–COOH).[468] To overcome the unsatisfactory biocompatibility of metal-based semiconductors, biological coatings such as PDA or chitosan can be modified on their surface to improve their biocompatibility and adhesion to bacteria.[180] In addition, physical encapsulation or chemical coupling can be used to construct a semiconductor carrier and delivery platform (such as SiO_2 microspheres) to improve the delivery efficiency of antibacterial drugs or achieve a sustained release function.[371]

(5) With the rise of theranostics, the visualization and specific identification of bacterial infections are of great significance. Semiconductors can be combined with imaging molecules (such as fluorescent molecules/radionuclide molecules) to achieve visual imaging of bacteria;[469] meanwhile, specific recognition molecules (such as lectin for food-borne pathogens[470]) of bacteria can be coupled to improve the targeting and selectivity to the target bacteria and realize real-time dynamic monitoring of antibacterial effects. Thus, the theranostic strategy has become an appealing direction for photocatalytic disinfection.

Abbreviation

ROS	Reactive oxygen species
2D	Two dimensional
0D	One dimensional
1D	One dimensional
NIR	Near infrared ray
G(+)	Gram-positive
G(−)	Gram-negative
BPs	Black phosphorus
PL intensity	Photoluminescence intensity
HRTEM	High resolution transmission electron microscopy
Redox	Oxidation–reduction reactions
CFM	Chitosan functionalized magnetic MoS_2
EPR study	Electron paramagnetic resonance study
PCR assay	Polymerase chain reaction assay
BCA assay	Bicinchoninic acid assay
Ce6	Chlorin e6

Conflicts of interest

The authors declare that they have no known competing financial interests or personal relationships that could have appeared to influence the work reported in this paper.

Acknowledgements

This work was supported by the National Natural Science Foundation of China (91753106), Primary Research & Development Plan of Jiangsu Province (BE2019716), and the National Key Research and Development Program of China (2017YFA0205300).

References

1 J. Perez, F. Javier Contreras-Moreno, F. Javier Marcos-Torres, A. Moraleda-Munoz and J. Munoz-Dorado, *Comput. Struct. Biotechnol. J.*, 2020, **18**, 2547–2555.
2 L. A. Rantz, *Calif. Med.*, 1954, **81**, 1–3.
3 P. B. Mead, *Semin. Perinatol.*, 1977, **1**, 101–111.
4 J. S. Pitton, *Ergeb. Physiol., Biol. Chem. Exp. Pharmakol.*, 1972, **65**, 15–93.
5 Z. Zhou, B. Li, X. Liu, Z. Li, S. Zhu, Y. Liang, Z. Cui and S. Wu, *ACS Appl. Bio Mater.*, 2021, **4**, 3909–3936.
6 Y. Liu, X. Zeng, X. Hu, Y. Xia and X. Zhang, *Sol. RRL*, 2021, **5**, 2000594.
7 N. A. Daub, F. Aziz, M. Aziz, J. Jaafar, W. N. W. Salleh, N. Yusof and A. F. Ismail, *Water, Air, Soil Pollut.*, 2020, **231**, 461.
8 X. Kong, X. Liu, Y. Zheng, P. K. Chu, Y. Zhang and S. Wu, *Mater. Sci. Eng., R*, 2021, **145**, 100610.
9 Y. Hu, Q. Li, H. Liu, B. Kong and Q. Chen, *Food Sci.*, 2020, **41**, 232–238.
10 P. Ganguly, C. Byrne, A. Breen and S. C. Pillai, *Appl. Catal., B*, 2018, **225**, 51–75.
11 A. Fujishima and K. Honda, *Nature*, 1972, **238**, 37–38.
12 T. Matsunaga, R. Tomoda, T. Nakajima and H. Wake, *FEMS Microbiol. Lett.*, 1985, **29**, 211–214.
13 M. D. Hernandez-Alonso, F. Fresno, S. Suarez and J. M. Coronado, *Energy Environ. Sci.*, 2009, **2**, 1231–1257.
14 M. S. Zhu, C. Y. Zhai, L. Q. Qiu, C. Lu, A. S. Paton, Y. K. Du and M. C. Goh, *ACS Sustainable Chem. Eng.*, 2015, **3**, 3123–3129.
15 H. M. Sung-Suh, J. R. Choi, H. J. Hah, S. M. Koo and Y. C. Bae, *J. Photochem. Photobiol., A*, 2004, **163**, 37–44.
16 A. B. Djurisic, Y. H. Leung and A. M. C. Ng, *Mater. Horiz.*, 2014, **1**, 400–410.
17 L. Armelao, D. Barreca, G. Bottaro, A. Gasparotto, C. Maccato, C. Maragno, E. Tondello, U. L. Stangar, M. Bergant and D. Mahne, *Nanotechnology*, 2007, **18**(37), 375709.
18 W. Choi, A. Termin and M. R. Hoffmann, *J. Phys. Chem.*, 1994, **98**, 13669–13679.
19 R. Asahi, T. Morikawa, T. Ohwaki, K. Aoki and Y. Taga, *Science*, 2001, **293**, 269–271.
20 F. I. Alzakia, B. Tang, S. J. Pennycook and S. C. Tan, *Mater. Horiz.*, 2020, **7**, 3325–3338.
21 M. Zeng, M. Chen, D. Huang, S. Lei, X. Zhang, L. Wang and Z. Cheng, *Mater. Horiz.*, 2021, **8**, 758–802.
22 W. Wang, Y. Yu, T. An, G. Li, H. Y. Yip, J. C. Yu and P. K. Wong, *Environ. Sci. Technol.*, 2012, **46**, 4599–4606.
23 Y. Wang, F. Huang, D. Pan, B. Li, D. Chen, W. Lin, X. Chen, R. Li and Z. Lin, *Chem. Commun.*, 2009, 6783–6785, DOI: 10.1039/b912137d.
24 T. Ashikaga, M. Wada, H. Kobayashi, M. Mori, Y. Katsumura, H. Fukui, S. Kato, M. Yamaguchi and T. Takamatsu, *Mutat. Res.*, 2000, **466**, 1–7.
25 P. C. Maness, S. Smolinski, D. M. Blake, Z. Huang, E. J. Wolfrum and W. A. Jacoby, *Appl. Environ. Microbiol.*, 1999, **65**, 4094.
26 J. Li, X. Liu, L. Tan, Y. Liang, Z. Cui, X. Yang, S. Zhu, Z. Li, Y. Zheng, K. W. K. Yeung, X. Wang and S. Wu, *Small Methods*, 2019, **3**, 1900048.
27 Y. Y. Zhang, X. Y. Bai, X. M. Wang, K. K. Shiu, Y. L. Zhu and H. Jiang, *Anal. Chem.*, 2014, **86**, 9459–9465.
28 G. Chen, J. Wang, C. Wu, C.-Z. Li, H. Jiang and X. Wang, *Langmuir*, 2012, **28**, 12393–12399.
29 H. C. Chang, X. M. Wang, K. K. Shiu, Y. L. Zhu, J. L. Wang, Q. W. Li, B. A. Chen and H. Jiang, *Biosens. Bioelectron.*, 2013, **41**, 789–794.
30 L. Wang, Y. Y. Zhang, C. S. Cheng, X. L. Liu, H. Jiang and X. M. Wang, *ACS Appl. Mater. Interfaces*, 2015, **7**, 18441–18449.
31 C. H. Li, X. L. Liu, Y. Y. Zhang, Y. Chen, T. Y. Du, H. Jiang and X. M. Wang, *Anal. Chim. Acta*, 2016, **933**, 66–74.
32 Y. K. Zheng, W. W. Liu, Y. Chen, H. Jiang and X. M. Wang, *J. Mater. Chem. B*, 2018, **6**, 3650–3654.
33 R. M. Mazhabi, L. Q. Ge, H. Jiang and X. M. Wang, *Biosens. Bioelectron.*, 2018, **107**, 54–61.
34 V. Ivády, I. A. Abrikosov, E. Janzén and A. Gali, *Phys. Rev. B: Condens. Matter Mater. Phys.*, 2013, **87**(20), 205201.
35 Y. Zhao and D. G. Truhlar, *J. Chem. Phys.*, 2009, **130**, 074103.
36 S. Cavo, J. A. Berger and P. Romaniello, *Phys. Rev. B*, 2020, **101**(11), 115109.

37 C.-F. Fu, X. Wu and J. Yang, *Adv. Mater.*, 2018, **30**, 1802106.
38 R. G. Parr, S. R. Gadre and L. J. Bartolotti, *Proc. Natl. Acad. Sci. U. S. A.*, 1979, **76**, 2522.
39 R. Marschall, *Adv. Funct. Mater.*, 2014, **24**, 2421–2440.
40 S. Bai, L. L. Wang, Z. Q. Li and Y. J. Xiong, *Adv. Sci.*, 2017, **4**(1), 1600216.
41 A. Lipovsky, L. Levitski, Z. Tzitrinovich, A. Gedanken and R. Lubart, *Photochem. Photobiol.*, 2012, **88**, 14–20.
42 G. Munuera, A. Navio and V. Rivesarnau, *J. Chem. Soc., Faraday Trans. 1*, 1981, **77**, 2747–2749.
43 Z. Yuan, B. Tao, Y. He, J. Liu, C. Lin, X. Shen, Y. Yu, C. Mu, P. Liu and K. Cai, *Biomaterials*, 2019, **217**, 119290.
44 V. A. Johnson and K. Larkhorovitz, *Phys. Rev.*, 1951, **82**, 763.
45 X. X. Sun, X. Q. Wang, P. Wang, B. W. Sheng, M. Li, J. Su, J. Zhang, F. Liu, X. Rong, F. J. Xu, X. L. Yang, Z. X. Qin, W. K. Ge and B. Shen, *Opt. Mater. Express*, 2017, **7**, 904–912.
46 Y. F. Yan, W. J. Yin, Y. L. Wu, T. T. Shi, N. R. Paudel, C. Li, J. Poplawsky, Z. W. Wang, J. Moseley, H. Guthrey, H. Moutinho, S. J. Pennycook and M. M. Al-Jassim, *J. Appl. Phys.*, 2015, **117**(11), 112807.
47 F. X. Ye, A. Ohmori and C. J. Li, *Surf. Coat. Technol.*, 2004, **184**, 233–238.
48 T. T. Zheng, J. Y. Xu, Z. J. Zhang and H. B. Zeng, *RSC Adv.*, 2015, **5**, 99658–99663.
49 Y. Y. Hu, N. Berdunov, C. A. Di, I. Nandhakumar, F. J. Zhang, X. K. Gao, D. B. Zhu and H. Sirringhaus, *ACS Nano*, 2014, **8**, 6778–6787.
50 Y. Miyoshi, K. Takahashi, T. Fujimoto, H. Yoshikawa, M. M. Matsushita, Y. Ouchi, M. Kepenekian, V. Robert, M. P. Donzello, C. Ercolani and K. Awaga, *Inorg. Chem.*, 2012, **51**, 456–462.
51 C. L. Guo, Z. Tian, Y. J. Xiao, Q. X. Mi and J. M. Xue, *Appl. Phys. Lett.*, 2016, **109**(20), 203104.
52 J. Cao, J. D. Querales-Flores, A. R. Murphy, S. Fahy and I. Savic, *Phys. Rev. B*, 2018, **98**(20), 205202.
53 Y. Li, W. Zhang, J. Niu and Y. Chen, *ACS Nano*, 2012, **6**, 5164–5173.
54 F. Vatansever, W. C. M. A. de Melo, P. Avci, D. Vecchio, M. Sadasivam, A. Gupta, R. Chandran, M. Karimi, N. A. Parizotto, R. Yin, G. P. Tegos and M. R. Hamblin, *FEMS Microbiol. Rev.*, 2013, **37**, 955–989.
55 K. W. Goodman and V. E. Henrich, *Phys. Rev. B: Condens. Matter Mater. Phys.*, 1994, **50**, 10450–10456.
56 C. M. Yim, C. L. Pang and G. Thornton, *Phys. Rev. Lett.*, 2010, **104**(3), 036806.
57 N. Serpone, *J. Phys. Chem. B*, 2006, **110**, 24287–24293.
58 O. Lupan, L. Chow, G. Y. Chai, L. Chernyak, O. Lopatiuk-Tirpak and H. Heinrich, *Phys. Status Solidi A*, 2008, **205**, 2673–2678.
59 J. Kiwi and V. Nadtochenko, *Langmuir*, 2005, **21**, 4631–4641.
60 M. Wang, J. Ioccozia, L. Sun, C. Lin and Z. Lin, *Energy Environ. Sci.*, 2014, **7**, 2182–2202.
61 R. Konaka, E. Kasahara, W. C. Dunlap, Y. Yamamoto, K. C. Chien and M. Inoue, *Redox Rep.*, 2001, **6**, 319–325.
62 R. Shen, D. Ren, Y. Ding, Y. Guan, Y. H. Ng, P. Zhang and X. Li, *Sci. China Mater.*, 2020, **63**, 2153–2188.
63 A. Jańczyk, E. Krakowska, G. Stochel and W. Macyk, *J. Am. Chem. Soc.*, 2006, **128**, 15574–15575.
64 F. P. Koffyberg and F. A. Benko, *J. Appl. Phys.*, 1982, **53**, 1173–1177.
65 A. O. Musa, T. Akomolafe and M. J. Carter, *Sol. Energy Mater. Sol. Cells*, 1998, **51**, 305–316.
66 G. Moretti and H. P. Beck, *Surf. Interface Anal.*, 2019, **51**, 1359–1370.
67 Q. Zhang, K. Zhang, D. Xu, G. Yang, H. Huang, F. Nie, C. Liu and S. Yang, *Prog. Mater. Sci.*, 2014, **60**, 208–337.
68 Z. Wang, P. K. Nayak, J. A. Caraveo-Frescas and H. N. Alshareef, *Adv. Mater.*, 2016, **28**, 3831–3892.
69 Q. B. Zhang, K. L. Zhang, D. G. Xu, G. C. Yang, H. Huang, F. D. Nie, C. M. Liu and S. H. Yang, *Prog. Mater. Sci.*, 2014, **60**, 208–337.
70 O. Akhavan, *J. Phys. D: Appl. Phys.*, 2008, **41**, 235407.
71 E. Apen, B. R. Rogers and J. A. Sellers, *J. Vac. Sci. Technol., A*, 1998, **16**, 1227–1232.
72 O. Akhavan and E. Ghaderi, *Surf. Coat. Technol.*, 2010, **205**, 219–223.
73 A. Torres, C. Ruales, C. Pulgarin, A. Aimable, P. Bowen, V. Sarria and J. Kiwi, *ACS Appl. Mater. Interfaces*, 2010, **2**, 2547–2552.
74 M. Paschoalino, N. C. Guedes, W. Jardim, E. Mielczarski, J. A. Mielczarski, P. Bowen and J. Kiwi, *J. Photochem. Photobiol., A*, 2008, **199**, 105–111.
75 T. Kaneto, K. W. Kim and M. A. Littlejohn, *Phys. Rev. B: Condens. Matter Mater. Phys.*, 1993, **47**, 16257–16266.
76 S. Kobayashi, M. Saitoh, Y. Nakabayashi and K. Uchida, *Appl. Phys. Lett.*, 2007, **91**(20), 203506.
77 A. D. de Meux, G. Pourtois, J. Genoe and P. Heremans, *Phys. Rev. B*, 2018, **97**(4), 045208.
78 X. Li, J. Yu and M. Jaroniec, *Chem. Soc. Rev.*, 2016, **45**, 2603–2636.
79 J. Xing, H. B. Jiang, J. F. Chen, Y. H. Li, L. Wu, S. Yang, L. R. Zheng, H. F. Wang, P. Hu, H. J. Zhao and H. G. Yang, *J. Mater. Chem. A*, 2013, **1**, 15258–15264.
80 Y. F. Sun, S. Gao, F. C. Lei and Y. Xie, *Chem. Soc. Rev.*, 2015, **44**, 623–636.
81 B. K. Yoo, Z. X. Su, J. M. Thomas and A. H. Zewail, *Proc. Natl. Acad. Sci. U. S. A.*, 2016, **113**, 503–508.
82 Y. Wang, H. Sun, S. Tan, H. Feng, Z. Cheng, J. Zhao, A. Zhao, B. Wang, Y. Luo, J. Yang and J. G. Hou, *Nat. Commun.*, 2013, **4**, 2214.
83 W. K. Wang, J. J. Chen, Z. Z. Lou, S. Kim, M. Fujitsuka, H. Q. Yu and T. Majima, *Proc. Natl. Acad. Sci. U. S. A.*, 2019, **116**, 18827–18833.
84 H. Pang, F. Gao and Q. Y. Lu, *Chem. Commun.*, 2009, 1076–1078, DOI: 10.1039/b816670f.
85 V. Lakshmi Prasanna and R. Vijayaraghavan, *Langmuir*, 2015, **31**, 9155–9162.
86 R. Gunder, J. A. Marquez-Prieto, G. Gurieva, T. Unold and S. Schorr, *CrystEngComm*, 2018, **20**, 1491–1498.
87 J. Xie, H. Zhang, S. Li, R. Wang, X. Sun, M. Zhou, J. Zhou, X. W. Lou and Y. Xie, *Adv. Mater.*, 2013, **25**, 5807–5813.

88 Y. Li, J. Niu, W. Zhang, L. Zhang and E. Shang, *Langmuir*, 2014, **30**, 2852–2862.
89 T. B. van Driel, K. S. Kjaer, R. W. Hartsock, A. O. Dohn, T. Harlang, M. Chollet, M. Christensen, W. Gawelda, N. E. Henriksen, J. G. Kim, K. Haldrup, K. H. Kim, H. Ihee, J. Kim, H. Lemke, Z. Sun, V. Sundstrom, W. K. Zhang, D. L. Zhu, K. B. Moller, M. M. Nielsen and K. J. Gaffney, *Nat. Commun.*, 2016, **7**, 13678.
90 X. A. Shen, Y. A. Small, J. Wang, P. B. Allen, M. V. Fernandez-Serra, M. S. Hybertsen and J. T. Muckerman, *J. Phys. Chem. C*, 2010, **114**, 13695–13704.
91 V. Lakshmi Prasanna and R. Vijayaraghavan, *Langmuir*, 2015, **31**, 9155–9162.
92 X. Yang, J. Li, T. Liang, C. Ma, Y. Zhang, H. Chen, N. Hanagata, H. Su and M. Xu, *Nanoscale*, 2014, **6**, 10126–10133.
93 A. C. Ferrari, F. Bonaccorso, V. Fal'ko, K. S. Novoselov, S. Roche, P. Boggild, S. Borini, F. H. Koppens, V. Palermo, N. Pugno, J. A. Garrido, R. Sordan, A. Bianco, L. Ballerini, M. Prato, E. Lidorikis, J. Kivioja, C. Marinelli, T. Ryhanen, A. Morpurgo, J. N. Coleman, V. Nicolosi, L. Colombo, A. Fert, M. Garcia-Hernandez, A. Bachtold, G. F. Schneider, F. Guinea, C. Dekker, M. Barbone, Z. Sun, C. Galiotis, A. N. Grigorenko, G. Konstantatos, A. Kis, M. Katsnelson, L. Vandersypen, A. Loiseau, V. Morandi, D. Neumaier, E. Treossi, V. Pellegrini, M. Polini, A. Tredicucci, G. M. Williams, B. H. Hong, J. H. Ahn, J. M. Kim, H. Zirath, B. J. van Wees, H. van der Zant, L. Occhipinti, A. Di Matteo, I. A. Kinloch, T. Seyller, E. Quesnel, X. Feng, K. Teo, N. Rupesinghe, P. Hakonen, S. R. Neil, Q. Tannock, T. Lofwander and J. Kinaret, *Nanoscale*, 2015, **7**, 4598–4810.
94 F. Schedin, A. K. Geim, S. V. Morozov, E. W. Hill, P. Blake, M. I. Katsnelson and K. S. Novoselov, *Nat. Mater.*, 2007, **6**, 652–655.
95 M. Zhou, X. W. Lou and Y. Xie, *Nano Today*, 2013, **8**, 598–618.
96 J. Wang, H. Shi, L. Jiang and L. Liu, *J. Funct. Mater.*, 2019, **50**(10), 10063–10073.
97 K. Khan, A. K. Tareen, M. Aslam, R. U. R. Sagar, B. Zhang, W. C. Huang, A. Mahmood, N. Mahmood, K. Khan, H. Zhang and Z. Y. Guo, *Nano-Micro Lett.*, 2020, **12**(1), 167.
98 X. D. Sun, L. T. Shi, H. W. Huang, X. M. Song and T. Y. Ma, *Chem. Commun.*, 2020, **56**, 11000–11013.
99 B. Luo, G. Liu and L. Wang, *Nanoscale*, 2016, **8**, 6904–6920.
100 B. Luo, G. Liu and L. Z. Wang, *Nanoscale*, 2016, **8**, 6904–6920.
101 J. Fu, J. Yu, C. Jiang and B. Cheng, *Adv. Energy Mater.*, 2018, **8**, 1701503.
102 W. J. Wang, J. C. Yu, D. H. Xia, P. K. Wong and Y. C. Li, *Environ. Sci. Technol.*, 2013, **47**, 8724–8732.
103 Z. H. Li, W. L. Wang, Q. Liu, Z. G. Zhang and X. M. Fang, *Mater. Res. Bull.*, 2018, **106**, 152–161.
104 W. W. Wang, L. Wang, W. B. Li, C. Feng, R. Qiu, L. K. Xu, X. D. Cheng and G. Q. Shao, *Mater. Lett.*, 2019, **234**, 183–186.
105 C. Lee, H. Yan, L. E. Brus, T. F. Heinz, J. Hone and S. Ryu, *ACS Nano*, 2010, **4**, 2695–2700.
106 Z. Liang, R. Shen, Y. H. Ng, P. Zhang, Q. Xiang and X. Li, *J. Mater. Sci. Technol.*, 2020, **56**, 89–121.
107 K. F. Mak, C. Lee, J. Hone, J. Shan and T. F. Heinz, *Phys. Rev. Lett.*, 2010, **105**, 136805.
108 S. M. Shinde, K. P. Dhakal, X. Chen, W. S. Yun, J. Lee, H. Kim and J. H. Ahn, *NPG Asia Mater.*, 2018, **10**, e468.
109 Z. He and W. Que, *Appl. Mater. Today*, 2016, **3**, 23–56.
110 T. B. Wendumu, G. Seifert, T. Lorenz, J. O. Joswig and A. Enyashin, *J. Phys. Chem. Lett.*, 2014, **5**, 3636–3640.
111 R. J. Tian, R. X. Fei, S. Q. Hu, T. S. Li, B. J. Zheng, Y. Shi, J. L. Zhao, L. J. Zhang, X. T. Gan and X. M. Wang, *Phys. Rev. B*, 2020, **101**, 7.
112 V. Tran, R. Soklaski, Y. Liang and L. Yang, *Phys. Rev. B: Condens. Matter Mater. Phys.*, 2014, **89**, 235319.
113 T. Sakthivel, X. Huang, Y. Wu and S. Rtimi, *Chem. Eng. J.*, 2020, **379**, 122297.
114 S. Banerjee and S. K. Pati, *Phys. Chem. Chem. Phys.*, 2016, **18**, 16345–16352.
115 R. Xu, J. Yang, Y. Zhu, H. Yan, J. Pei, Y. W. Myint, S. Zhang and Y. Lu, *Nanoscale*, 2016, **8**, 129–135.
116 K. F. Mak, C. Lee, J. Hone, J. Shan and T. F. Heinz, *Phys. Rev. Lett.*, 2010, **105**, 4.
117 H. S. Lee, S.-W. Min, Y.-G. Chang, M. K. Park, T. Nam, H. Kim, J. H. Kim, S. Ryu and S. Im, *Nano Lett.*, 2012, **12**, 3695–3700.
118 Y. Li, X. Li, H. Zhang, J. Fan and Q. Xiang, *J. Mater. Sci. Technol.*, 2020, **56**, 69–88.
119 Y. F. Sun, Q. H. Liu, S. Gao, H. Cheng, F. C. Lei, Z. H. Sun, Y. Jiang, H. B. Su, S. Q. Wei and Y. Xie, *Nat. Commun.*, 2013, **4**, 2899.
120 F. Yao, Y. Cai, Z. Xiao, G. Zhang, R.-J. Xie and C. Jin, *2D Mater.*, 2020, **8**, 025004.
121 X. Tian, Y. Sun, S. Fan, M. D. Boudreau, C. Chen, C. Ge and J.-J. Yin, *ACS Appl. Mater. Interfaces*, 2019, **11**, 4858–4866.
122 C. Liu, D. S. Kong, P. C. Hsu, H. T. Yuan, H. W. Lee, Y. Y. Liu, H. T. Wang, S. Wang, K. Yan, D. C. Lin, P. A. Maraccini, K. M. Parker, A. B. Boehm and Y. Cui, *Nat. Nanotechnol.*, 2016, **11**, 1098–1104.
123 C. Liu, D. Kong, P. C. Hsu, H. Yuan, H. W. Lee, Y. Liu, H. Wang, S. Wang, K. Yan, D. Lin, P. A. Maraccini, K. M. Parker, A. B. Boehm and Y. Cui, *Nat. Nanotechnol.*, 2016, **11**, 1098–1104.
124 W. T. Zhang, S. Shi, Y. R. Wang, S. X. Yu, W. X. Zhu, X. Zhang, D. H. Zhang, B. W. Yang, X. Wang and J. L. Wang, *Nanoscale*, 2016, **8**, 11642–11648.
125 J. A. Lemire, J. J. Harrison and R. J. Turner, *Nat. Rev. Microbiol.*, 2013, **11**, 371–384.
126 M. Tatullo, F. Genovese, E. Aiello, M. Amantea, I. Makeeva, B. Zavan, S. Rengo and L. Fortunato, *Materials*, 2019, **12**, 11.
127 W. Liu, Y. Zhang, Y. Zhang and A. Dong, *Chem. – Eur. J.*, 2020, **26**, 2478–2485.
128 J. Shao, C. Ruan, H. Xie, Z. Li, H. Wang, P. Chu and X.-F. Yu, *Adv. Sci.*, 2018, **5**, 1700848.

129 S. M. Shinde, K. P. Dhakal, X. Chen, W. S. Yun, J. Lee, H. Kim and J.-H. Ahn, *NPG Asia Mater.*, 2018, **10**, e468.
130 C. Y. Lan, Z. Shi, R. Cao, C. Li and H. Zhang, *Nanoscale*, 2020, **12**, 11784–11807.
131 B. Liu, H. H. Tai, H. Y. Liang, E. Y. Zheng, M. Sahoo, C. H. Hsu, T. C. Chen, C. A. Huang, J. C. Wang, T. H. Hou and C. S. Lai, *Mater. Chem. Front.*, 2020, **4**, 1756–1763.
132 B. W. H. Baugher, H. O. H. Churchill, Y. F. Yang and P. Jarillo-Herrero, *Nano Lett.*, 2013, **13**, 4212–4216.
133 K. Kaasbjerg, T. Low and A. P. Jauho, *Phys. Rev. B*, 2019, **100**(11), 115409.
134 G. Z. He, T. Dong, Z. C. Yang and P. Ohlckers, *Chem. Mater.*, 2019, **31**, 9917–9938.
135 S. Thurakkal and X. Y. Zhang, *Adv. Sci.*, 2020, **7**(2), 1902359.
136 L. Tan, J. Li, X. Liu, Z. Cui, X. Yang, K. Yeung, H. Pan, Y. Zheng, X. Wang and S. Wu, *Small*, 2017, **14**, 1703197.
137 C. Mao, Y. Xiang, X. Liu, Z. Cui, X. Yang, Z. Li, S. Zhu, Y. Zheng, K. Yeung and S. Wu, *ACS Nano*, 2018, **12**(2), 1747–1759.
138 J. M. Pirie, *Chem. Ind.*, 1951, 65.
139 M. Zhu, X. M. Liu, L. Tan, Z. D. Cui, Y. Q. Liang, Z. Y. Li, K. Wai, K. Yeung and S. L. Wu, *J. Hazard. Mater.*, 2020, **383**, 121122.
140 F. Raza, D. Yim, J. H. Park, H. I. Kim, S. J. Jeon and J. H. Kim, *J. Am. Chem. Soc.*, 2017, **139**, 14767–14774.
141 X. Xin, S. H. Li, N. Zhang, Z. R. Tang and Y. J. Xu, *Appl. Catal., B*, 2019, **245**, 343–350.
142 U. Baig, M. A. Gondal, M. A. Dastageer, A. B. Khalil and S. M. Zubair, *J. Photochem. Photobiol., B*, 2018, **187**, 113–119.
143 Y. Peng, B. Z. Lu and S. W. Chen, *Adv. Mater.*, 2018, **30**, 25.
144 Z. Huang, X. Gu, Q. Cao, P. Hu, J. Hao, J. Li and X. Tang, *Angew. Chem., Int. Ed.*, 2012, **51**, 4198–4203.
145 S. C. Warren and E. Thimsen, *Energy Environ. Sci.*, 2012, **5**, 5133–5146.
146 S. K. Cushing and N. Wu, *J. Phys. Chem. Lett.*, 2016, **7**, 666–675.
147 W. Fan and M. K. Leung, *Molecules*, 2016, **21**(2), 180.
148 S. Yu, Y. H. Kim, S. Y. Lee, H. D. Song and J. Yi, *Angew. Chem., Int. Ed.*, 2014, **53**, 11203–11207.
149 L. M. Lai, X. R. Jiang, S. Y. Han, C. Q. Zhao, T. Y. Du, F. U. Rehman, Y. K. Zheng, X. Q. Li, X. L. Liu, H. Jiang and X. M. Wang, *Langmuir*, 2017, **33**, 9018–9024.
150 T. Y. Du, C. Q. Zhao, F. U. Rehman, L. M. Lai, X. Q. Li, Y. Sun, S. H. Luo, H. Jiang, M. Selke and X. M. Wang, *Nano Res.*, 2017, **10**, 2626–2632.
151 Z. He, R. Liu, C. Xu, Y. Lai, W. Shan and J. Liu, *Appl. Catal., B*, 2021, **285**, 119775.
152 Y. Lei, F. Mehmood, S. Lee, J. Greeley, B. Lee, S. Seifert, R. E. Winans, J. W. Elam, R. J. Meyer, P. C. Redfern, D. Teschner, R. Schlogl, M. J. Pellin, L. A. Curtiss and S. Vajda, *Science*, 2010, **328**, 224–228.
153 C. S. Wang, J. Y. Li, C. Amatore, Y. Chen, H. Jiang and X. M. Wang, *Angew. Chem., Int. Ed.*, 2011, **50**, 11644–11648.
154 X. Y. Lv, W. Ge, Q. W. Li, Y. L. Wu, H. Jiang and X. M. Wang, *ACS Appl. Mater. Interfaces*, 2014, **6**, 11025–11031.
155 C. Q. Zhao, T. Y. Du, F. U. Rehman, L. M. Lai, X. L. Liu, X. R. Jiang, X. Q. Li, Y. Chen, H. Zhang, Y. Sun, S. H. Luo, H. Jiang, M. Selke and X. M. Wang, *Small*, 2016, **12**, 6255–6265.
156 J. Ye, X. W. Dong, H. Jiang and X. M. Wang, *J. Mater. Chem. B*, 2017, **5**, 691–696.
157 S. Shaikh, F. U. Rehman, T. Y. Du, H. Jiang, L. H. Yin, X. M. Wang and R. J. Chai, *ACS Appl. Mater. Interfaces*, 2018, **10**, 26056–26063.
158 Y. Zhao, X. Li, H. Li and L. He, *New J. Chem.*, 2021, **45**, 15378–15385.
159 X. Weng, B. Shi, A. Liu, J. Sun, Y. Xiong, H. Wan, S. Zheng, L. Dong and Y.-W. Chen, *Appl. Surf. Sci.*, 2019, **497**, 143747.
160 G. D. Wu, G. Q. Zhao, J. H. Sun, X. Z. Cao, Y. F. He, J. T. Feng and D. Q. Li, *J. Catal.*, 2019, **377**, 271–282.
161 L. Jiang, X. Yuan, Y. Pan, J. Liang, G. Zeng, Z. Wu and H. Wang, *Appl. Catal., B*, 2017, **217**, 388–406.
162 R. Kavitha, P. M. Nithya and S. Girish Kumar, *Appl. Surf. Sci.*, 2020, **508**, 145142.
163 L. Zhou, H. Y. Zhang, H. Q. Sun, S. M. Liu, M. O. Tade, S. B. Wang and W. Q. Jin, *Catal. Sci. Technol.*, 2016, **6**, 7002–7023.
164 C. Moslah, G. A. Mousdis, M. Kandyla, G. Petropoulou and M. Ksibi, in *Nanostructured Materials for the Detection of Cbrn*, ed. J. Bonca and S. Kruchinin, 2018, pp. 71–89, DOI: 10.1007/978-94-024-1304-5_6.
165 M. A. Barakat, R. I. Al-Hutailah, E. Qayyum, J. Rashid and J. N. Kuhn, *Environ. Technol.*, 2014, **35**, 137–144.
166 S. F. Su, L. M. Ye, Q. M. Tian, W. B. Situ, X. L. Song and S. Y. Ye, *Appl. Surf. Sci.*, 2020, **515**, 145964.
167 L. Shang, B. Li, W. Dong, B. Chen, C. Li, W. Tang, G. Wang, J. Wu and Y. Ying, *J. Hazard. Mater.*, 2010, **178**, 1109–1114.
168 R. Gupta, N. K. Eswar, J. M. Modak and G. Madras, *Catal. Today*, 2018, **300**, 71–80.
169 L. Q. Mei, S. Zhu, W. Y. Yin, C. Y. Chen, G. J. Nie, Z. J. Gu and Y. L. Zhao, *Theranostics*, 2020, **10**, 757–781.
170 G. Pedroza-Herrera, I. E. Medina-Ramirez, J. A. Lozano-Alvarez and S. E. Rodil, *Catal. Today*, 2020, **341**, 37–48.
171 Q. Zhang, X. M. Liu, L. Tan, Z. D. Cui, Z. Y. Li, Y. Q. Liang, S. L. Zhu, K. W. K. Yeung, Y. F. Zheng and S. L. Wu, *Chem. Eng. J.*, 2020, **383**, 123088.
172 V. Amenta, K. Aschberger, M. Arena, H. Bouwmeester, F. B. Moniz, P. Brandhoff, S. Gottardo, H. J. P. Marvin, A. Mech, L. Q. Pesudo, H. Rauscher, R. Schoonjans, M. V. Vettori, S. Weigel and R. J. Peters, *Regul. Toxicol. Pharmacol.*, 2015, **73**, 463–476.
173 A. Zane, R. Zuo, F. A. Villamena, A. Rockenbauer, A. M. D. Foushee, K. Flores, P. K. Dutta and A. Nagy, *Int. J. Nanomed.*, 2016, **11**, 6459–6470.
174 R. Masa, A. Deak, G. Braunitzer, Z. Toth, J. Kopniczky, I. Pelsoczi-Kovacs, K. Ungvari, I. Dekany and K. Turzo, *J. Nanosci. Nanotechnol.*, 2018, **18**, 3916–3924.
175 V. Rodríguez-González, C. Terashima and A. Fujishima, *J. Photochem. Photobiol., C*, 2019, **40**, 49–67.
176 A. J. Misra, S. Das, A. P. H. Rahman, B. Das, R. Jayabalan, S. K. Behera, M. Suar, A. J. Tamhankar, A. Mishra,

C. S. Lundborg and S. K. Tripathy, *J. Colloid Interface Sci.*, 2018, **530**, 610–623.
177 R. Wang, B. Zhang, Z. Liang, Y. He, Z. Wang, X. Ma, X. Yao, J. Sun and J. Wang, *Appl. Catal., B*, 2019, **241**, 167–177.
178 Y. Li, W. Zhang, J. F. Niu and Y. S. Chen, *ACS Nano*, 2012, **6**, 5164–5173.
179 P. C. Maness, S. Smolinski, D. M. Blake, Z. Huang, E. J. Wolfrum and W. A. Jacoby, *Appl. Environ. Microbiol.*, 1999, **65**, 4094–4098.
180 Y. Y. Wu, Y. Z. Zhou, H. Xu, Q. G. Liu, Y. Li, L. L. Zhang, H. G. Liu, Z. G. Tu, X. N. Cheng and J. Yang, *ACS Sustainable Chem. Eng.*, 2018, **6**, 14082–14094.
181 Y. Wu, L. Zhang, Y. Zhou, L. Zhang, Y. Li, Q. Liu, J. Hu and J. Yang, *Chin. J. Catal.*, 2019, **40**, 691–702.
182 I. Teixeira, J. Quiroz, M. Homsi and P. Camargo, *J. Braz. Chem. Soc.*, 2020, **31**, 211–229.
183 A. Kasahara, K. Nukumizu, T. Takata, J. N. Kondo, M. Hara, H. Kobayashi and K. Domen, *J. Phys. Chem. B*, 2003, **107**, 791–797.
184 H. Kato and A. Kudo, *J. Phys. Chem. B*, 2001, **105**, 4285–4292.
185 Y. H. Xu, H. R. Chen, Z. X. Zeng and B. Lei, *Appl. Surf. Sci.*, 2006, **252**, 8565–8570.
186 X. L. Liu, H. Jiang, J. Ye, C. Q. Zhao, S. P. Gao, C. Y. Wu, C. H. Li, J. C. Li and X. M. Wang, *Adv. Funct. Mater.*, 2016, **26**, 8694–8706.
187 A. Mittal, B. Mari, S. Sharma, V. Kumari, S. Maken, K. Kumari and N. Kumar, *J. Mater. Sci.: Mater. Electron.*, 2019, **30**, 3186–3207.
188 W. Y. Choi, A. Termin and M. R. Hoffmann, *J. Phys. Chem.*, 1994, **98**, 13669–13679.
189 H. Yu, H. Irie, Y. Shimodaira, Y. Hosogi, Y. Kuroda, M. Miyauchi and K. Hashimoto, *J. Phys. Chem. C*, 2010, **114**, 16481–16487.
190 S. K. Loeb, P. J. J. Alvarez, J. A. Brame, E. L. Cates, W. Choi, J. Crittenden, D. D. Dionysiou, Q. Li, G. Li-Puma, X. Quan, D. L. Sedlak, T. David Waite, P. Westerhoff and J.-H. Kim, *Environ. Sci. Technol.*, 2019, **53**, 2937–2947.
191 L. Brus, *J. Phys. Chem.*, 1986, **90**, 2555–2560.
192 M. I. Litter, *Appl. Catal., B*, 1999, **23**, 89–114.
193 Z. F. Shen, F. F. Li, J. R. Lu, Z. D. Wang, R. Li, X. C. Zhang, C. M. Zhang, Y. W. Wang, Y. F. Wang, Z. P. Lv, J. X. Liu and C. M. Fan, *J. Colloid Interface Sci.*, 2021, **584**, 174–181.
194 K. Z. Qi, X. H. Xing, A. Zada, M. Y. Li, Q. Wang, S. Y. Liu, H. X. Lin and G. Z. Wang, *Ceram. Int.*, 2020, **46**, 1494–1502.
195 S. Yadav and G. Jaiswar, *J. Chin. Chem. Soc.*, 2017, **64**, 103–116.
196 P. Sanitnon, S. Chiarakorn, C. Chawengkijwanich, S. Chuangchote and T. Pongprayoon, *J. Aust. Ceram. Soc.*, 2020, **56**, 579–590.
197 Z. Zha, S. Zhang, Z. Deng, Y. Li, C. Li and Z. Dai, *Chem. Commun.*, 2013, **49**, 3455–3457.
198 D. L. Han, Y. J. Han, J. Li, X. M. Liu, K. W. K. Yeung, Y. F. Zheng, Z. D. Cui, X. J. Yang, Y. Q. Liang, Z. Y. Li, S. L. Zhu, X. B. Yuan, X. B. Feng, C. Yang and S. L. Wu, *Appl. Catal., B*, 2020, **261**, 12.
199 H. Irie, K. Kamiya, T. Shibanuma, S. Miura, D. A. Tryk, T. Yokoyama and K. Hashimoto, *J. Phys. Chem. C*, 2009, **113**, 10761–10766.
200 M. Vautier, C. Guillard and J. M. Herrmann, *J. Catal.*, 2001, **201**, 46–59.
201 C. L. Yu, H. B. He, Q. Z. Fan, W. Y. Xie, Z. Liu and H. B. Ji, *Sci. Total Environ*, 2019, **694**, 133727.
202 M. A. Mohamed, N. A. Rahman, M. F. M. Zain, L. J. Minggu, M. B. Kassim, J. Jaafar, S. Samad, M. S. Mastuli and R. J. Wong, *J. Alloys Compd.*, 2020, **820**, 153143.
203 J. C. Yu, J. G. Yu, W. K. Ho, Z. T. Jiang and L. Z. Zhang, *Chem. Mater.*, 2002, **14**, 3808–3816.
204 W. Wang, M. O. Tade and Z. P. Shao, *Prog. Mater. Sci.*, 2018, **92**, 33–63.
205 X. Bai, J. Jia, Y. Y. Du, X. Y. Hu, J. L. Li, E. Z. Liu and J. Fan, *Appl. Surf. Sci.*, 2020, **503**, 144298.
206 M. Rahbar, M. Mehrzad, M. Behpour, S. Mohammadi-Aghdam and M. Ashrafi, *Nanotechnology*, 2019, **30**(50), 505702.
207 V. Etacheri, C. Di Valentin, J. Schneider, D. Bahnemann and S. C. Pillai, *J. Photochem. Photobiol., C*, 2015, **25**, 1–29.
208 Q. Q. Yin, R. Qiao and G. X. Tong, *Prog. Chem.*, 2014, **26**, 1619–1632.
209 Y. J. Jang, M. D. Bhatt, J. Lee, S. H. Choi, B. J. Lee and J. S. Lee, *Adv. Energy Mater.*, 2018, **8**, 1702636.
210 H. Zhang, Y. Zhang, J. Yin, Z. Li, Q. Zhu and Z. Xing, *Chem. Phys.*, 2018, **513**, 86–93.
211 C. Zhu, M. Zhu, Y. Sun, Y. Zhou, H. Huang, Y. Lifshitz, S.-T. Lee, J. Zhong, Y. Liu and Z. Kang, *Appl. Catal., B*, 2018, **237**, 166–174.
212 I. Milošević, S. Rtimi, A. Jayaprakash, B. van Driel, B. Greenwood, A. Aimable, M. Senna and P. Bowen, *Colloids Surf., B*, 2018, **171**, 445–450.
213 M. Zheng and J. Wu, *Appl. Surf. Sci.*, 2009, **255**, 5656–5661.
214 K. Qi, B. Cheng, J. Yu and W. Ho, *J. Alloys Compd.*, 2017, **727**, 792–820.
215 Y. Xu, K. Lv, Z. Xiong, W. Leng, W. Du, D. Liu and X. Xue, *J. Phys. Chem. C*, 2007, **111**, 19024–19032.
216 C. Di Valentin, G. Pacchioni and A. Selloni, *J. Phys. Chem. C*, 2009, **113**, 20543–20552.
217 N. U. M. Nor and N. A. S. Amin, *J. CO2 Util.*, 2019, **33**, 372–383.
218 F. Amano, M. Nakata, J. J. M. Vequizo and A. Yamakata, *ACS Appl. Energy Mater.*, 2019, **2**, 3274–3282.
219 N. Najibi Ilkhechi, M. R. Akbarpour, R. Yavari and Z. Azar, *J. Mater. Sci.: Mater. Electron.*, 2017, **28**, 16658–16664.
220 H. Liu and L. Gao, *Chem. Lett.*, 2004, **33**, 730–731.
221 K. Gupta, J. Kumar, R. P. Sing, A. Pandey, P. Rai and A. Pandey, *Mater. Technol.*, 2019, **34**, 765–775.
222 S. Gao, W. Yang, J. Xiao, B. Li and Q. Li, *J. Mater. Sci. Technol.*, 2019, **35**, 610–614.
223 X. Niu, W. Yan, C. Shao, H. Zhao and J. Yang, *Appl. Surf. Sci.*, 2019, **466**, 882–892.
224 S. Na Phattalung, S. Limpijumnong and J. Yu, *Appl. Catal., B*, 2017, **200**, 1–9.

225 N. Serpone, E. Borgarello and M. Gratzel, *J. Chem. Soc., Chem. Commun.*, 1984, 342–344, DOI: 10.1039/c39840000342.
226 R. Shen, K. He, A. Zhang, N. Li, Y. H. Ng, P. Zhang, J. Hu and X. Li, *Appl. Catal., B*, 2021, **291**, 120104.
227 R. Shen, Y. Ding, S. Li, P. Zhang, Q. Xiang, Y. H. Ng and X. Li, *Chin. J. Catal.*, 2021, **42**, 25–36.
228 P. Zhang and X. W. Lou, *Adv. Mater.*, 2019, **31**, 1900281.
229 L. Liu, T. Hu, K. Dai, J. Zhang and C. Liang, *Chin. J. Catal.*, 2021, **42**, 46–55.
230 J. X. Low, J. G. Yu, M. Jaroniec, S. Wageh and A. A. Al-Ghamdi, *Adv. Mater.*, 2017, **29**, 20.
231 Y. N. Jia, S. H. Zhan, S. L. Ma and Q. X. Zhou, *ACS Appl. Mater. Interfaces*, 2016, **8**, 6841–6851.
232 T. W. Ng, L. S. Zhang, J. S. Liu, G. C. Huang, W. Wang and P. K. Wong, *Water Res.*, 2016, **90**, 111–118.
233 Y. Jia, S. Zhan, S. Ma and Q. Zhou, *ACS Appl. Mater. Interfaces*, 2016, **8**, 6841–6851.
234 T. W. Ng, L. Zhang, J. Liu, G. Huang, W. Wang and P. K. Wong, *Water Res.*, 2016, **90**, 111–118.
235 M. Cho, H. Chung, W. Choi and J. Yoon, *Appl. Environ. Microbiol.*, 2005, **71**, 270.
236 L. Armelao, D. Barreca, G. Bottaro, A. Gasparotto, C. Maccato, C. Maragno, E. Tondello, U. L. Stangar, M. Bergant and D. Mahne, *Nanotechnology*, 2007, **18**, 7.
237 K. Hayashi, K. Nozaki, Z. Tan, K. Fujita, R. Nemoto, K. Yamashita, H. Miura, K. Itaka and S. Ohara, *Materials*, 2020, **13**(1), 78.
238 K. R. Raghupathi, R. T. Koodali and A. C. Manna, *Langmuir*, 2011, **27**, 4020–4028.
239 S. K. Ray, D. Dhakal, J. Hur and S. W. Lee, *Nanotechnology*, 2020, **31**, 16.
240 Y. Li and Y. F. Cheng, *J. Mater. Chem. B*, 2018, **6**, 1458–1469.
241 X. Tian, Y. R. Sun, S. H. Fan, M. D. Boudreau, C. Y. Chen, C. C. Ge and J. J. Yin, *ACS Appl. Mater. Interfaces*, 2019, **11**, 4858–4866.
242 L. Xiong, H. Yu, C. Nie, Y. Xiao, Q. Zeng, G. Wang, B. Wang, H. Lv, Q. Li and S. Chen, *RSC Adv.*, 2017, **7**, 51822–51830.
243 L. Xiong, T. W. Ng, Y. Yu, D. Xia, H. Y. Yip, G. Li, T. An, H. Zhao and P. K. Wong, *Electrochim. Acta*, 2015, **153**, 583–593.
244 J. Huang, W. Ho and X. Wang, *Chem. Commun.*, 2014, **50**, 4338–4340.
245 J. H. Thurston, N. M. Hunter and K. A. Cornell, *RSC Adv.*, 2016, **6**, 42240–42248.
246 D. Xia, Z. Shen, G. Huang, W. Wang, J. C. Yu and P. K. Wong, *Environ. Sci. Technol.*, 2015, **49**, 6264–6273.
247 Y. Zhong, C. Peng, Z. He, D. Chen, H. Jia, J. Zhang, H. Ding and X. Wu, *Catal. Sci. Technol.*, 2021, **11**(1), DOI: 10.1039/d0cy01847c.
248 S. Adhikari, A. Banerjee, N. K. Eswar, D. Sarkar and G. Madras, *RSC Adv.*, 2015, **5**, 51067–51077.
249 M. M. Li, D. G. Li, Z. R. Zhou, P. F. Wang, X. Y. Mi, Y. G. Xia, H. T. Wang, S. H. Zhan, Y. Li and L. M. Li, *Chem. Eng. J.*, 2020, **382**, 122762.
250 Y. Li, J. Zhao, G. S. Zhang, L. L. Zhang, S. Y. Ding, E. X. Shang and X. H. Xia, *Water Res.*, 2019, **161**, 251–261.
251 A. Senthilraja, B. Krishnakumar, R. Hariharan, A. Sobral, C. Surya, N. A. A. John and M. Shanthi, *Sep. Purif. Technol.*, 2018, **202**, 373–384.
252 M. C. Wu, T. H. Lin, K. H. Hsu and J. F. Hsu, *Appl. Surf. Sci.*, 2019, **484**, 326–334.
253 C. Liang, H. Guo, L. Zhang, M. Ruan, C.-G. Niu, H.-P. Feng, X.-J. Wen, N. Tang, H.-Y. Liu and G.-M. Zeng, *Chem. Eng. J.*, 2019, **372**, 12–25.
254 L. Jing, Y. Xu, S. Huang, M. Xie, M. He, H. Xu, H. Li and Q. Zhang, *Appl. Catal., B*, 2016, **199**, 11–22.
255 L. Jing, Y. Xu, C. Qin, J. Liu, S. Huang, M. He, H. Xu and H. Li, *Mater. Res. Bull.*, 2017, **95**, 607–615.
256 D. Han, Y. Han, J. Li, X. Liu, K. W. K. Yeung, Y. Zheng, Z. Cui, X. Yang, Y. Liang, Z. Li, S. Zhu, X. Yuan, X. Feng, C. Yang and S. Wu, *Appl. Catal., B*, 2020, **261**, 118248.
257 N. F. A. Neto, K. N. Matsui, C. A. Paskocimas, M. R. D. Bomio and F. V. Motta, *Mater. Sci. Semicond. Process.*, 2019, **93**, 123–133.
258 D. Neena, M. Humayun, D. Z. Lu, V. B. Mohan, D. J. Fu and W. Gao, *Ceram. Int.*, 2020, **46**, 5278–5288.
259 Q. F. Zhao, M. Wang, H. Yang, D. Shi and Y. Z. Wang, *Ceram. Int.*, 2018, **44**, 5145–5154.
260 Y. Wang, X. Xue and H. Yang, *Ceram. Int.*, 2014, **40**, 12533–12537.
261 V. Etacheri, G. Michlits, M. K. Seery, S. J. Hinder and S. C. Pillai, *ACS Appl. Mater. Interfaces*, 2013, **5**, 1663–1672.
262 R. S. Pessoa, V. P. dos Santos, S. B. Cardoso, A. C. O. C. Doria, F. R. Figueira, B. V. M. Rodrigues, G. E. Testoni, M. A. Fraga, F. R. Marciano, A. O. Lobo and H. S. Maciel, *Appl. Surf. Sci.*, 2017, **422**, 73–84.
263 N. Tahmasebizad, M. T. Hamedani, M. Shaban Ghazani and Y. Pazhuhanfar, *J. Sol-Gel Sci. Technol.*, 2020, **93**, 570–578.
264 K. V. Divya Lakshmi, T. Siva Rao, J. Swathi Padmaja, I. Manga Raju and M. Ravi Kumar, *Chin. J. Chem. Eng.*, 2019, **27**, 1630–1641.
265 Y. Z. Wang, Y. S. Wu, H. Yang, M. Wang, X. G. Shi, C. Wang and S. W. Zhang, *Mater. Technol.*, 2018, **33**, 48–56.
266 N. S. Leyland, J. Podporska-Carroll, J. Browne, S. J. Hinder, B. Quilty and S. C. Pillai, *Sci. Rep.*, 2016, **6**, 24770.
267 K. Ravichandran, R. Uma, B. Sakthivel, S. Gobalakrishnan and P. K. Praseetha, *J. Mater. Sci.: Mater. Electron.*, 2016, **27**, 1609–1615.
268 R. Michal, E. Dworniczek, M. Caplovicova, M. Gregor, L. U. Caplovic, A. Seniuk, P. Kus and G. Plesch, *Ceram. Int.*, 2014, **40**, 5745–5756.
269 P. Zhou, J. Yu and M. Jaroniec, *Adv. Mater.*, 2014, **26**, 4920–4935.
270 D. Xia, W. Wang, R. Yin, Z. Jiang, T. An, G. Li, H. Zhao and P. K. Wong, *Appl. Catal., B*, 2017, **214**, 23–33.
271 X. Zeng, Z. Wang, G. Wang, T. R. Gengenbach, D. T. McCarthy, A. Deletic, J. Yu and X. Zhang, *Appl. Catal., B*, 2017, **218**, 163–173.
272 Y. Xiang, Q. Zhou, Z. Li, Z. Cui, X. Liu, Y. Liang, S. Zhu, Y. Zheng, K. W. K. Yeung and S. Wu, *J. Mater. Sci. Technol.*, 2020, **57**, 1–11.

273 H. Yan, R. Wang, R. Liu, T. Xu, J. Sun, L. Liu and J. Wang, *Appl. Catal., B*, 2021, **291**, 120096.
274 T. W. Ng, L. Zhang, J. Liu, G. Huang, W. Wang and P. K. Wong, *Water Res.*, 2016, **90**, 111–118.
275 S. Zhang, C. Liu, X. Liu, H. Zhang, P. Liu, S. Zhang, F. Peng and H. Zhao, *Appl. Microbiol. Biotechnol.*, 2012, **96**, 1201–1207.
276 P. Ju, Y. Wang, Y. Sun and D. Zhang, *Dalton Trans.*, 2016, **45**, 4588–4602.
277 V. Siyahi, A. Habibi-Yangjeh, S. Latifi-Navid and A. Asadi, *Mater. Express*, 2015, **5**, 201–210.
278 G. Tong, F. Du, W. Wu, R. Wu, F. Liu and Y. Liang, *J. Mater. Chem. B*, 2013, **1**, 2647.
279 O. Akhavan, R. Azimirad, S. Safa and M. M. Larijani, *J. Mater. Chem.*, 2010, **20**, 7386.
280 O. Akhavan, R. Azimirad and S. Safa, *Mater. Chem. Phys.*, 2011, **130**, 598–602.
281 M. J. Muñoz-Batista, M. Ferrer, M. Fernández-García and A. Kubacka, *Appl. Catal., B*, 2014, **154–155**, 350–359.
282 Y. Jin, Z. Dai, F. Liu, H. Kim, M. Tong and Y. Hou, *Water Res.*, 2013, **47**, 1837–1847.
283 W. Wang, J. C. Yu, D. Xia, P. K. Wong and Y. Li, *Environ. Sci. Technol.*, 2013, **47**, 8724–8732.
284 D. L. Guan, C. G. Niu, X. J. Wen, H. Guo, C. H. Deng and G. M. Zeng, *J. Colloid Interface Sci.*, 2018, **512**, 272–281.
285 S. J. Gu, D. Zhang, S. R. Luo and H. Yang, *Int. J. Photoenergy*, 2019, **2019**, 6307858.
286 M. Padervand, *Appl. Nanosci.*, 2016, **6**, 1119–1126.
287 J. Liu, L. Huang, Y. Li, L. Yang, C. Wang, J. Liu, Y. Song, M. Yang and H. Li, *J. Colloid Interface Sci.*, 2021, **600**, 344–357.
288 C. Chen, D. Wang, Y. Li, H. Huang and Y. Ke, *Appl. Surf. Sci.*, 2021, **565**, 150534.
289 Y. Sun, X. Qi, R. Li, Y. Xie, Q. Tang and B. Ren, *Opt. Mater.*, 2020, **108**, 110170.
290 A. Enesca and L. Andronic, *Nanomaterials*, 2021, **11**(4), 871.
291 J. Low, J. Yu, M. Jaroniec, S. Wageh and A. A. Al-Ghamdi, *Adv. Mater.*, 2017, **29**, 1601694.
292 J. Fu, Q. Xu, J. Low, C. Jiang and J. Yu, *Appl. Catal., B*, 2019, **243**, 556–565.
293 R. He, H. Liu, H. Liu, D. Xu and L. Zhang, *J. Mater. Sci. Technol.*, 2020, **52**, 145–151.
294 Q. Xu, D. Ma, S. Yang, Z. Tian, B. Cheng and J. Fan, *Appl. Surf. Sci.*, 2019, **495**, 143555.
295 S. Wageh, A. A. Al-Ghamdi, R. Jafer, X. Li and P. Zhang, *Chin. J. Catal.*, 2021, **42**, 667–669.
296 R. C. Shen, X. Y. Lu, Q. Q. Zheng, Q. Chen, Y. H. Ng, P. Zhang and X. Li, *Sol. RRL*, 2021, **5**(7), 2100177.
297 S. Li, C. Wang, M. Cai, F. Yang, Y. Liu, J. Chen, P. Zhang, X. Li and X. Chen, *Chem. Eng. J.*, 2022, **428**, 131158.
298 P. Xia, S. Cao, B. Zhu, M. Liu, M. Shi, J. Yu and Y. Zhang, *Angew. Chem., Int. Ed.*, 2020, **59**, 5218–5225.
299 J. Wang, G. Wang, B. Cheng, J. Yu and J. Fan, *Chin. J. Catal.*, 2021, **42**, 56–68.
300 S. P. Adhikari, H. R. Pant, J. H. Kim, H. J. Kim, C. H. Park and C. S. Kim, *Colloids Surf., A*, 2015, **482**, 477–484.
301 V. Shanmugam, A. L. Muppudathi, S. Jayavel and K. S. Jeyaperumal, *Arabian J. Chem.*, 2020, **13**, 2439–2455.
302 S. Vignesh, S. Suganthi, J. K. Sundar and V. Raj, *J. Ind. Eng. Chem.*, 2019, **76**, 318–332.
303 J. Xu, Q. Z. Gao, X. J. Bai, Z. P. Wang and Y. F. Zhu, *Catal. Today*, 2019, **332**, 227–235.
304 M. J. Munoz-Batista, O. Fontelles-Carceller, M. Ferrer, M. Fernandez-Garcia and A. Kubacka, *Appl. Catal., B*, 2016, **183**, 86–95.
305 W. Zhang, C. Yu, Z. Sun and S. Zheng, *J. Microbiol. Biotechnol.*, 2018, **28**, 957–967.
306 Y. Wu, Y. Zhou, H. Xu, Q. Liu, Y. Li, L. Zhang, H. Liu, Z. Tu, X. Cheng and J. Yang, *ACS Sustainable Chem. Eng.*, 2018, **6**, 14082–14094.
307 Q. Zhang, X. Quan, H. Wang, S. Chen, Y. Su and Z. L. Li, *Sci. Rep.*, 2017, **7**, 3128.
308 Y. Y. Qin, Y. C. Guo, Z. Q. Liang, Y. J. Xue, X. L. Zhang, L. Yang and J. Tian, *Chin. Chem. Lett.*, 2021, **32**, 1523–1526.
309 P. Dhandapani, M. S. AlSalhi, R. Karthick, F. M. Chen, S. Devanesan, W. Kim, A. Rajasekar, M. Ahmed, M. J. Aljaafreh and A. Muhammad, *J. Hazard. Mater.*, 2021, **409**, 124661.
310 J. W. Xu, Y. Li, X. M. Zhou, Y. Z. Li, Z. D. Gao, Y. Y. Song and P. Schmuki, *Chem. – Eur. J.*, 2016, **22**, 3947–3951.
311 H. Y. Sun, Z. Q. Yang, Y. N. Pu, W. W. Dou, C. Y. Wang, W. H. Wang, X. P. Hao, S. G. Chen, Q. Shao, M. Y. Dong, S. D. Wu, T. Ding and Z. H. Guo, *J. Colloid Interface Sci.*, 2019, **547**, 40–49.
312 W. J. Wang, G. Y. Li, T. C. An, D. K. L. Chan, J. C. Yu and P. K. Wong, *Appl. Catal., B*, 2018, **238**, 126–135.
313 H. Li, H. Yu, X. Quan, S. Chen and Y. Zhang, *ACS Appl. Mater. Interfaces*, 2016, **8**, 2111–2119.
314 J. Li, Y. C. Yin, E. Z. Liu, Y. N. Ma, J. Wan, J. Fan and X. Y. Hu, *J. Hazard. Mater.*, 2017, **321**, 183–192.
315 X. Y. Zhao, M. M. Chen, H. L. Wang, L. Xia, M. Guo, S. W. Jiang, Q. Wang, X. J. Li and X. F. Yang, *Mater. Sci. Eng., C*, 2020, **116**, 111221.
316 B. K. Liu, X. L. Han, Y. Wang, X. Fan, Z. Y. Wang, J. T. Zhang and H. Z. Shi, *J. Mater. Sci.: Mater. Electron.*, 2018, **29**, 14300–14310.
317 Y. Jia, S. Zhan, S. Ma and Q. Zhou, *ACS Appl. Mater. Interfaces*, 2016, **8**, 6841–6851.
318 T. S. Natarajan, K. R. Thampi and R. J. Tayade, *Appl. Catal., B*, 2018, **227**, 296–311.
319 J. Li, S. Zhang, W. Guo, H. Qi, H. Liang and L. Mao, *Chin. J. Semicond.*, 2005, **26**, 2416–2421.
320 D. Zhang, Z. Yang, J. Hao, T. Zhang, Q. Sun and Y. Wang, *Chemosphere*, 2021, **276**, 130226.
321 J. J. Zhao, J.-S. Zhang, F. Zhang, W. Wang, H. R. He, W. Y. Cai and J. Wang, *Chin. Phys. B*, 2019, **28**(12), 126801.
322 C. F. Yu, K. Wang, P. Y. Yang, S. N. Yang, C. Lu, Y. Z. Song, S. Y. Dong, J. Y. Sun and J. H. Sun, *Appl. Surf. Sci.*, 2017, **420**, 233–242.
323 A. Kumar, G. Sharma, A. Kumari, C. Guo, M. Naushad, D. V. N. Vo, J. Iqbal and F. J. Stadler, *Appl. Catal., B*, 2021, **284**, 119808.

324 Y. Zhou, M. Yu, H. Liang, J. Chen, L. Xu and J. Niu, *Appl. Catal., B*, 2021, **291**, 120105.
325 M. Guo, Z. Xing, T. Zhao, Z. Li, S. Yang and W. Zhou, *Appl. Catal., B*, 2019, **257**, 117913.
326 J. Yu, J. Low, W. Xiao, P. Zhou and M. Jaroniec, *J. Am. Chem. Soc.*, 2014, **136**, 8839–8842.
327 J. Zhang, L. Zhang, W. Yu, F. Jiang, E. Zhang, H. Wang, Z. Kong, J. Xi and Z. Ji, *J. Am. Ceram. Soc.*, 2017, **100**, 5274–5285.
328 J. Zhang, L. Zhang, Y. Shi, G. Xu, E. Zhang, H. Wang, Z. Kong, J. Xi and Z. Ji, *Appl. Surf. Sci.*, 2017, **420**, 839–848.
329 A. K. Geim and K. S. Novoselov, *Nat. Mater.*, 2007, **6**, 183–191.
330 J. Li, E. Z. Liu, Y. N. Ma, X. Y. Hu, J. Wan, L. Sun and J. Fan, *Appl. Surf. Sci.*, 2016, **364**, 694–702.
331 Q. Zhang, X. Liu, L. Tan, Z. Cui, Z. Li, Y. Liang, S. Zhu, K. W. K. Yeung, Y. Zheng and S. Wu, *Chem. Eng. J.*, 2020, **383**, 123088.
332 B. Han, S. Liu, Y.-J. Xu and Z.-R. Tang, *RSC Adv.*, 2015, **5**, 16476–16483.
333 G. P. Neupane, K. Zhou, S. Chen, T. Yildirim, P. Zhang and Y. Lu, *Small*, 2019, **15**, 1804733.
334 Y. Li, P. Zhang, D. Wan, C. Xue, J. Zhao and G. Shao, *Appl. Surf. Sci.*, 2020, **504**, 144361.
335 Z. Jiang, Q. Chen, Q. Zheng, R. Shen, P. Zhang and X. Li, *Acta Phys.-Chim. Sin.*, 2020, **0**, 2010059.
336 Z. Xu, J. Jiang, Q. Zhang, G. Chen, L. Zhou and L. Li, *J. Colloid Interface Sci.*, 2020, **563**, 131–138.
337 W. Zhao, J. Liu, Z. Ding, J. Zhang and X. Wang, *J. Alloys Compd.*, 2020, **813**, 152234.
338 Z. Lou and C. Xue, *CrystEngComm*, 2016, **18**, 8406–8410.
339 R. Zhang, L. Huang, Z. Yu, R. Jiang, Y. Hou, L. Sun, B. Zhang, Y. Huang, B. Ye and Y. Zhang, *Electrochim. Acta*, 2019, **323**, 134845.
340 D. Ren, Z. Liang, Y. H. Ng, P. Zhang, Q. Xiang and X. Li, *Chem. Eng. J.*, 2020, **390**, 124496.
341 H. J. Cheng, J. G. Hou, O. Takeda, X. M. Guo and H. M. Zhu, *J. Mater. Chem. A*, 2015, **3**, 11006–11013.
342 D. He, Z. Zhang, Y. Xing, Y. Zhou, H. Yang, H. Liu, J. Qu, X. Yuan, J. Guan and Y.-N. Zhang, *Chem. Eng. J.*, 2020, **384**, 123258.
343 B. O'Regan and M. Grätzel, *Nature*, 1991, **353**, 737–740.
344 Y. X. Xing, H. Zhu, G. F. Chang, M. Yu, M. Zhao, F. L. Yue and Iop, *2018 4th International Conference on Environmental Science and Material Application*, 2019, vol. 252.
345 G. A. da Collina, F. Freire, V. D. Barbosa, C. B. Correa, H. R. Nascimento, A. C. R. T. Horliana, D. D. T. da Silva, R. A. Prates and C. Pavani, *Photodiagn. Photodyn. Ther.*, 2020, **29**, 101612.
346 N. Maldonado-Carmona, T. S. Ouk, M. J. F. Calvete, M. M. Pereira, N. Villandier and S. Leroy-Lhez, *Photochem. Photobiol. Sci.*, 2020, **19**, 445–461.
347 R. Santus, *Pathol. Biol.*, 1991, **39**, 54–58.
348 G. K. Couto, B. S. Pacheco, V. M. Borba, J. C. Rodrigues, T. L. Oliveira, N. V. Segatto, F. K. Seixas, T. V. Acunha, B. A. Iglesias and T. Collares, *J. Photochem. Photobiol., B*, 2020, **202**, 111725.
349 M. Q. Yang, J. R. Deng, D. Guo, J. Zhang, L. X. Yang and F. S. Wu, *Org. Biomol. Chem.*, 2020, **18**, 569.
350 W. Zhu, Y. H. Gao, P. Y. Liao, D. Y. Chen, N. N. Sun, P. A. N. Thi, Y. J. Yan, X. F. Wu and Z. L. Chen, *Eur. J. Med. Chem.*, 2018, **160**, 146–156.
351 C. Xu, W. Hu, N. Zhang, Y. Qi, J.-J. Nie, N. Zhao, B. Yu and F.-J. Xu, *Biomaterials*, 2020, **248**, 120031.
352 A. Sadiki, E. M. Kercher, H. B. Lu, R. T. Lang, B. Q. Spring and Z. S. Zhou, *Photochem. Photobiol.*, 2020, **96**, 596–603.
353 Y. L. He, S. J. Wang, L. W. Zhang, J. Xin, J. Wang, C. P. Yao, Z. X. Zhang and C. C. Yang, *J. Biomed. Opt.*, 2016, **21**, 9.
354 N. Zhang, L. Wen, J. Yan and Y. Liu, *Chem. Pap.*, 2020, **74**, 389–406.
355 O. Bettucci, T. Skaltsas, M. Calamante, A. Dessì, M. Bartolini, A. Sinicropi, J. Filippi, G. Reginato, A. Mordini, P. Fornasiero and L. Zani, *ACS Appl. Energy Mater.*, 2019, **2**, 5600–5612.
356 X. H. Zhang, T. Y. Peng and S. S. Song, *J. Mater. Chem. A*, 2016, **4**, 2365–2402.
357 Y. Li, C. Xie, S. Peng, G. Lu and S. Li, *J. Mol. Catal. A: Chem.*, 2008, **282**, 117–123.
358 Q. Li and G. Lu, *J. Mol. Catal. A: Chem.*, 2007, **266**, 75–79.
359 Y. Li, M. Guo, S. Peng, G. Lu and S. Li, *Int. J. Hydrogen Energy*, 2009, **34**, 5629–5636.
360 T. Shimidzu, T. Iyoda and Y. Koide, *J. Am. Chem. Soc.*, 1985, **107**, 35–41.
361 Z. Jin, X. Zhang, G. Lu and S. Li, *J. Mol. Catal. A: Chem.*, 2006, **259**, 275–280.
362 B. C. M. Martindale, G. A. M. Hutton, C. A. Caputo and E. Reisner, *J. Am. Chem. Soc.*, 2015, **137**, 6018–6025.
363 J. Xu, Y. Li and S. Peng, *Int. J. Hydrogen Energy*, 2015, **40**, 353–362.
364 C. Kong, S. Min and G. Lu, *Int. J. Hydrogen Energy*, 2014, **39**, 4836–4844.
365 C. Kong, S. Min and G. Lu, *ACS Catal.*, 2014, **4**, 2763–2769.
366 X. Zhang, L. Yu, C. Zhuang, T. Peng, R. Li and X. Li, *ACS Catal.*, 2014, **4**, 162–170.
367 X. Zhang, T. Peng, L. Yu, R. Li, Q. Li and Z. Li, *ACS Catal.*, 2015, **5**, 504–510.
368 K. Hirano, E. Suzuki, A. Ishikawa, T. Moroi, H. Shiroishi and M. Kaneko, *J. Photochem. Photobiol., A*, 2000, **136**, 157–161.
369 K. Hirano, E. Suzuki, A. Ishikawa, T. Moroi, H. Shiroishi and M. Kaneko, *J. Photochem. Photobiol., A*, 2000, **136**, 157–161.
370 D. N. Furlong, D. Wells and W. H. F. Sasse, *J. Phys. Chem.*, 1986, **90**, 1107–1115.
371 P. Chanhom, N. Charoenlap, C. Manipuntee and N. Insin, *J. Magn. Magn. Mater.*, 2019, **475**, 602–610.
372 M. Giridhar, H. S. BhojyaNaik, R. Vishwanath, C. N. Sudhamani, M. C. Prabakar and R. Kenchappa, *Mater. Today: Proc.*, 2017, **4**, 11671–11678.
373 L. Zan, S. Wang, W. Fa, Y. Hu, L. Tian and K. Deng, *Polymer*, 2006, **47**, 8155–8162.
374 Y. Xing, H. Zhu, G. Chang, M. Yu, M. Zhao, F. Yue and Iop, in *2018 4th International Conference on Environmental Science and Material Application*, 2019, vol. 252.

375 A. Zyoud, M. Dwikat, S. Al-Shakhshir, S. Ateeq, J. Shteiwi, A. Zu'bi, M. H. S. Helal, G. Campet, D. Park, H. Kwon, T. W. Kim, M. Kharoof, R. Shawahna and H. S. Hilal, *J. Photochem. Photobiol., A*, 2016, **328**, 207–216.
376 M. A. Khan, S. Mutahir, F. Wang, J. W. Zhou, W. Lei and M. Xia, *Sol. Energy*, 2019, **186**, 204–214.
377 X. Yang, D. Wang, Y. Shi, J. Zou, Q. Zhao, Q. Zhang, W. Huang, J. Shao, X. Xie and X. Dong, *ACS Appl. Mater. Interfaces*, 2018, **10**, 12431–12440.
378 M. Giridhar, H. S. BhojyaNaik, R. Vishwanath, C. N. Sudhamani, M. C. Prabakar and R. Kenchappa, *Mater. Today: Proc.*, 2017, **4**, 11671–11678.
379 A. Galstyan, *Chem. – Eur. J.*, 2020, **27**, 1903–1920.
380 C. Yan, X. Shao, Q. Shu, Y. Teng, Y. Qiao, P. Guan, X. Hu and C. Wang, *Int. J. Biol. Macromol.*, 2021, **186**, 839–848.
381 A. C. Bevilacqua, M. H. Kohler, B. A. Iglesia and P. C. Piquini, *Comput. Mater. Sci.*, 2019, **158**, 228–234.
382 Y. Sun, Y. L. Sun, C. Dall'Agnese, X. F. Wang, G. Chen, O. Kitao, H. Tamiaki, K. Sakai, T. Ikeuchi and S. Sasaki, *ACS Appl. Energy Mater.*, 2018, **1**, 2813–2820.
383 Y. Jiao, J.-F. Xu, Z. Wang and X. Zhang, *ACS Appl. Mater. Interfaces*, 2017, **9**, 22635–22640.
384 J. H. van Wonderen, D. Li, S. E. H. Piper, C. Y. Lau, L. P. Jenner, C. R. Hall, T. A. Clarke, N. J. Watmough and J. N. Butt, *ChemBioChem*, 2018, **19**, 2206–2215.
385 A. H. Zyoud, F. Saleh, M. H. Helal, R. Shawahna and H. S. Hilal, *J. Nanomater.*, 2018, **2018**, 2789616.
386 Y. X. Xing, H. Zhu, G. F. Chang, M. Yu, M. Zhao and F. L. Yue, 2018 *4th International Conference on Environmental Science and Material Application*, 2019, vol. 252.
387 M. Hosseini-Sarvari, M. Koohgard, S. Firoozi, A. Mohajeri and H. Tavakolian, *New J. Chem.*, 2018, **42**, 6880–6888.
388 K. S. Yao, D. Y. Wang, C. Y. Chang, W. Y. Ho and L. Y. Yang, *J. Nanosci. Nanotechnol.*, 2008, **8**, 2699–2702.
389 Y. W. Zhao, Q. W. Shang, J. C. Yu, Y. J. Zhang and S. Q. Liu, *ACS Appl. Mater. Interfaces*, 2015, **7**, 11783–11791.
390 H. H. Mohamed, I. Hammami, S. Akhtar and T. E. Youssef, *Composites, Part B*, 2019, **176**, 107314.
391 J. T. P. Matshwele, F. Nareetsile, D. Mapolelo, P. Matshameko, M. Leteane, D. O. Nkwe and S. Odisitse, *J. Chem.*, 2020, **2020**, 2150419.
392 N. Nambagari, S. Perka, R. K. Vuradi and S. Satyanarayana, *Nucleosides, Nucleotides Nucleic Acids*, 2019, **38**, 400–417.
393 Q. Y. Yi, W. Y. Zhang, M. He, F. Du, X. Z. Wang, Y. J. Wang, Y. Y. Gu, L. Bai and Y. J. Liu, *J. Biol. Inorg. Chem.*, 2019, **24**, 151–169.
394 J. Lu, Z. Li, W. An, L. Liu and W. Cui, *Nanomaterials*, 2019, **9**(9), 1321.
395 Y. Tian, K. E. Martin, J. Y. T. Shelnutt, L. Evans, T. Busani, J. E. Miller, C. J. Medforth and J. A. Shelnutt, *Chem. Commun.*, 2011, **47**, 6069–6071.
396 N. N. Zhang, L. Wen, J. Y. Yan and Y. Liu, *Chem. Pap.*, 2020, **74**, 389–406.
397 Y. Zhu, Y. Huang, Q. Li, D. Zang, J. Gu, Y. Tang and Y. Wei, *Inorg. Chem.*, 2020, **59**, 2575–2583.
398 T. Kim, S. Ham, S. H. Lee, Y. Hong and D. Kim, *Nanoscale*, 2018, **10**, 16438–16446.
399 S. Saraswat, A. Desireddy, D. Zheng, L. Guo, H. P. Lu, T. P. Bigioni and D. Isailovic, *J. Phys. Chem. C*, 2011, **115**, 17587–17593.
400 H. V. R. Maraka, R. M. Al-Shammari, N. Al-Attar, S. G. Lopez, T. E. Keyes and J. H. Rice, *Mater. Res. Express*, 2014, **1**, 045038.
401 S. P. Wang, W. Lin, X. Wang, T. Y. Cen, H. Xie, J. Huang, B. Y. Zhu, Z. Zhang, A. Song, J. Hao, J. Wu and S. Li, *Nat. Commun.*, 2019, **10**, 1399.
402 Z. Wang, C. J. Medforth and J. A. Shelnutt, *J. Am. Chem. Soc.*, 2004, **126**, 15954–15955.
403 S. Verma, A. Ghosh, A. Ghosh and H. N. Ghosh, *Chem. – Eur. J.*, 2011, **17**, 3458–3464.
404 C. Costa-Coquelard, S. Sorgues and L. Ruhlmann, *J. Phys. Chem. A*, 2010, **114**, 6394–6400.
405 Y. L. He, S. Wang, L. Zhang, J. Xin, J. Wang, C. Yao, Z. Zhang and C. C. Yang, *J. Biomed. Opt.*, 2016, **21**, 128001.
406 Y. He, J. Xiong, C. Yao, W. Jing and Z. Zhang, *Proc. SPIE*, 2015, **9449**, 944910.
407 Y. Zhao, Q. Shang, J. Yu, Y. Zhang and S. Liu, *ACS Appl. Mater. Interfaces*, 2015, **7**, 11783–11791.
408 C. Q. Zhao, F. U. Rehman, Y. L. Yang, X. Q. Li, D. Zhang, H. Jiang, M. Selke, X. M. Wang and C. Y. Liu, *Sci. Rep.*, 2015, **5**, 11518.
409 C. Q. Zhao, F. U. Rehman, H. Jiang, M. Selke, X. M. Wang and C. Y. Liu, *Sci. China: Chem.*, 2016, **59**, 637–642.
410 F. U. Rehman, C. Q. Zhao, C. Y. Wu, H. Jiang, M. Selke and X. M. Wang, *RSC Adv.*, 2015, **5**, 107285.
411 F. U. Rehman, C. Q. Zhao, C. Y. Wu, X. Q. Li, H. Jiang, M. Selke and X. M. Wang, *Nano Res.*, 2016, **9**, 3305–3321.
412 F. U. Rehman, C. Q. Zhao, H. Jiang, M. Selke and X. M. Wang, *Photodiagn. Photodyn. Ther.*, 2016, **13**, 267–275.
413 F. U. Rehman, C. Q. Zhao, H. Jiang, M. Selke and X. M. Wang, *J. Nanosci. Nanotechnol.*, 2016, **16**, 12691–12694.
414 J. Schindler, Y. Zhang, P. Traber, J. F. Lefebvre, S. Kupfer, M. Demeunynck, S. Grafe, M. Chavarot-Kerlidou and B. Dietzek, *J. Phys. Chem. C*, 2018, **122**, 83–95.
415 B. Tambosco, K. Segura, C. Seyrig, D. Cabrera, M. Port, C. Ferroud and Z. Amara, *ACS Catal.*, 2018, **8**, 4383–4389.
416 D. van der Westhuizen, K. G. von Eschwege and J. Conradie, *Data Brief*, 2019, **27**, 104759.
417 T. P. Yoon, *Acc. Chem. Res.*, 2016, **49**, 2307–2315.
418 J. D. Knoll, S. M. Arachchige and K. J. Brewer, *ChemSusChem*, 2011, **4**, 252–261.
419 K. Murata, M. Araki, A. Inagaki and M. Akita, *Dalton Trans.*, 2013, **42**, 6989–7001.
420 Y. Sasaki, H. Kato and A. Kudo, *J. Am. Chem. Soc.*, 2013, **135**, 5441–5449.
421 J. E. Martin, E. J. Hart, A. W. Adamson, H. Gafney and J. Halpern, *J. Am. Chem. Soc.*, 1972, **94**, 9238–9240.
422 S. Campagna, F. Puntoriero, F. Nastasi, G. Bergamini and V. Balzani, in *Photochemistry and Photophysics of Coordination Compounds I*, ed. V. Balzani and S. Campagna,

Springer Berlin Heidelberg, Berlin, Heidelberg, 2007, pp. 117–214, DOI: 10.1007/128_2007_133.
423 J. K. McCusker, *Acc. Chem. Res.*, 2003, **36**, 876–887.
424 M. Kuss-Petermann and O. S. Wenger, *Chem. – Eur. J.*, 2017, **23**, 10808–10814.
425 R. Konduri, H. Ye, F. M. MacDonnell, S. Serroni, S. Campagna and K. Rajeshwar, *Angew. Chem., Int. Ed.*, 2002, **41**, 3185–3187.
426 J. I. Goldsmith, W. R. Hudson, M. S. Lowry, T. H. Anderson and S. Bernhard, *J. Am. Chem. Soc.*, 2005, **127**, 7502–7510.
427 H. P. Liang, A. Acharjya, D. A. Anito, S. Vogl, T. X. Wang, A. Thomas and B. H. Han, *ACS Catal.*, 2019, **9**, 3959–3968.
428 W. F. Tian, Y. Q. He, X. R. Song, H. X. Ding, J. Ye, W. J. Guo and Q. Xiao, *Adv. Synth. Catal.*, 2020, **362**, 1032–1038.
429 D. M. Schultz and T. P. Yoon, *Science*, 2014, **343**, 1239176.
430 B. G. Tweedy, *Phytopathology*, 1964, **54**, 910–914.
431 B. Norden, P. Lincoln, B. Akerman and E. Tuite, in *Metal Ions in Biological Systems, Vol 33: Probing of Nucleic Acids by Metal Ion Complexes of Small Molecules*, ed. A. Sigel and H. Sigel, 1996, vol. 33, pp. 177–252.
432 A. D. Richards and A. Rodger, *Chem. Soc. Rev.*, 2007, **36**, 471–483.
433 H. Zhang, *Med. Chem.*, 2016, **6**, DOI: 10.4172/2161-0444.1000338.
434 N. E. A. El-Gamel and A. M. Fekry, *Bioelectrochemistry*, 2015, **104**, 35–43.
435 F. F. Li, J. G. Collins and F. R. Keene, *Chem. Soc. Rev.*, 2015, **44**, 2529–2542.
436 S. Li, C. Wu, X. Tang, S. Gao, X. Zhao, H. Yan and X. Wang, *Sci. China: Chem.*, 2013, **56**, 595–603.
437 A. R. Battersby, C. J. R. Fookes, G. W. J. Matcham and E. McDonald, *Nature*, 1980, **285**, 17–21.
438 L. Cheng, R. S. Assary, X. H. Qu, A. Jain, S. P. Ong, N. N. Rajput, K. Persson and L. A. Curtiss, *J. Phys. Chem. Lett.*, 2015, **6**, 283–291.
439 L. Castro and M. Buhl, *J. Chem. Theory Comput.*, 2014, **10**, 243–251.
440 G. Hautier, A. Jain and S. P. Ong, *J. Mater. Sci.*, 2012, **47**, 7317–7340.
441 N. S. Soukos, L. A. Ximenez-Fyvie, M. R. Hamblin, S. S. Socransky and T. Hasan, *Antimicrob. Agents Chemother.*, 1998, **42**, 2595.
442 S. Ferro, F. Ricchelli, G. Mancini, G. Tognon and G. Jori, *J. Photochem. Photobiol., B*, 2006, **83**, 98–104.
443 A. V. Kustov, D. V. Belykh, N. L. Smirnova, E. A. Venediktov, T. V. Kudayarova, S. O. Kruchin, I. S. Khudyaeva and D. B. Berezin, *Dyes Pigm.*, 2018, **149**, 553–559.
444 E. A. Groisman, *Trends Microbiol.*, 1994, **2**, 444–449.
445 M. Vaara and T. Vaara, *Antimicrob. Agents Chemother.*, 1983, **24**, 107–113.
446 P. Giege, J. M. Grienenberger and G. Bonnard, *Mitochondrion*, 2008, **8**, 61–73.
447 N. C. Robinson, *J. Bioenerg. Biomembr.*, 1993, **25**, 153–163.
448 G. Y. Jiang, W. H. Lei, Y. J. Hou and X. S. Wang, *New J. Chem.*, 2012, **36**, 2180–2183.
449 M. F. B. Vázquez, L. R. Comini, J. M. Milanesio, S. C. N. Montoya, J. L. Cabrera, S. Bottini and R. E. Martini, *J. Supercrit. Fluids*, 2015, **101**, 170–175.
450 Y. Wang, W. H. Chen, G. Y. Chen, X. P. Song, D. S. Zhang, B. Fu and Y. Chen, *Chin. J. Org. Chem.*, 2014, **34**, 522–525.
451 S. C. N. Montoya, A. M. Agnese, C. Perez, I. N. Tiraboschi and J. L. Cabrera, *Phytomedicine*, 2003, **10**, 569–574.
452 L. R. Comini, S. C. Núñez Montoya, P. L. Páez, G. A. Argüello, I. Albesa and J. L. Cabrera, *J. Photochem. Photobiol., B*, 2011, **102**, 108–114.
453 J. Y. Shin, Y. S. Kim, H. S. Cho and S. H. Lee, *US Pat.*, KR2017114738-A, 2017.
454 B. A. S. Reyes, E. C. Dufourt, J. Ross, M. J. Warner, N. C. Tanquilut and A. B. Leung, *Stud. Nat. Prod. Chem.*, 2018, **55**, 111–143.
455 E. Lima, M. J. Martínez-Ortiz, E. Fregoso and J. Méndez-Vivar, in *Studies in Surface Science and Catalysis*, ed. R. Xu, Z. Gao, J. Chen and W. Yan, Elsevier, 2007, vol. 170, pp. 2110–2115.
456 W. A. Dhafina, M. Z. Daud and H. Salleh, *Optik*, 2020, **207**, 163808.
457 C. Diaz-Uribe, W. Vallejo, G. Camargo, A. Munoz-Acevedo, C. Quinones, E. Schott and X. Zarate, *J. Photochem. Photobiol., A*, 2019, **384**, 112050.
458 L. Cui, J. J. Hu, W. Wang, C. Yan, Y. Guo and C. Tu, *Cellulose*, 2020, **27**, 6367–6381.
459 Q. Q. Yang, A. K. Farha, G. Kim, K. Gul, R. Y. Gan and H. Corke, *Trends Food Sci. Technol.*, 2020, **97**, 341–354.
460 L. Sobotta, P. Skupin-Mrugalska, J. Piskorz and J. Mielcarek, *Eur. J. Med. Chem.*, 2019, **175**, 72–106.
461 J. Oyim, C. A. Omolo and E. K. Amuhaya, *Front. Chem.*, 2021, **384**, 112050.
462 X. Lu, R. Chen, J. Lv, W. Xu, H. Chen, Z. Ma, S. Huang, S. Li, H. Liu, J. Hu and L. Nie, *Acta Biomater.*, 2019, **99**, 363–372.
463 R. Lood, K. W. Waldetoft and P. Nordenfelt, *Future Microbiol.*, 2015, **10**, 1659–1668.
464 C. Zhang, Y. Li, D. Shuai, Y. Shen and D. Wang, *Chem. Eng. J.*, 2019, **355**, 399–415.
465 S. Archana, K. Y. Kumar, B. K. Jayanna, S. Olivera, A. Anand, M. K. Prashanth and H. B. Muralidhara, *J. Sci.: Adv. Mater. Devices*, 2018, **3**, 167–174.
466 J.-D. Xiao and H.-L. Jiang, *Acc. Chem. Res.*, 2019, **52**, 356–366.
467 S. Kumar, T. Surendar, B. Kumar, A. Baruah and V. Shanker, *J. Phys. Chem. C*, 2013, **117**, 26135–26143.
468 Y. F. Cheng, Y. H. Mei, G. Sathishkumar, Z. S. Lu, C. M. Li, F. Wang, Q. Y. Xia and L. Q. Xu, *Colloids Interface Sci. Commun.*, 2020, **35**, 100241.
469 F. Aldeek, C. Mustin, L. Balan, T. Roques-Carmes, M.-P. Fontaine-Aupart and R. Schneider, *Biomaterials*, 2011, **32**, 5459–5470.
470 G. Yang, P. Li, L. Hu, X. Meng, Y. Wang and H. Xu, *Microbiology*, 2019, **46**, 1136–1145.

